Flux vortices in type II superconducting films

Stoddart, S. T.

Award date:
1994

Awarding institution:
University of Bath

Flux Vortices in Type II Superconducting Films

Submitted by S.T. Stoddart

for the degree of PhD

of the University of Bath

1994

ProQuest LLC
789 East Eisenhower Parkway
P.O. Box 1346
Ann Arbor, MI 48106-1346

Abstract

Vortex-resolved investigations have been carried out on type II superconducting films in a perpendicular magnetic field using micron-sized Hall probes. Sensitive Hall probes were fabricated from a GaAs/$Al_xGa_{1-x}As$ heterostructure containing a high mobility two-dimensional electron gas.

Pb and Pb(1% In) films 200nm thick were directly deposited onto Hall probes with characteristic dimensions from 10 to 2μm. Magnetic field sweeps below T_c yielded hysteresis loops which showed delayed flux entry and exit from the film due to flux pinning. Discontinuities in the hysteresis loops were caused by the sudden entry or exit of flux bundles. A coincidence measurement employing pairs of 2μm Hall bars established that the flux bundles had a temperature-independent correlation radius of 2.6μm. It was possible to track single vortices and correlated bundles as they moved small distances of 20-40nm in response to a change in temperature or under the action of an applied dc supercurrent. The signatures of flux creep and flux flow were identified, and the pinning force determined at individual pinning sites.

Similar measurements were carried out on a 200nm-thick Nb film and a 350nm-thick $YBa_2Cu_3O_{7-\delta}$ (YBCO) film. The flux bundle radius in the Nb film was found to decrease from 3.4μm to 1.6μm as the temperature increased from 4.5K to 6.5K. A sensitive differential measurement showed that single vortices entered the YBCO film in an uncorrelated fashion. The YBCO hysteresis loops could be described by a critical state model, yielding the critical current in the film over a wide temperature range. Pinning force measurements showed that vortices in the YBCO film were depinned by thermal activation at a temperature below the critical temperature of the film.

Acknowledgements

I would like to thank my supervisor Simon Bending for giving me the opportunity of undertaking the work described in this thesis, and for being an unfailing source of advice and enthusiasm.

Without contributions from many people and institutions, my task would have been impossible. I am most grateful to all of the following : M. Henini of Nottingham University for providing many of the heterostructures used to make the Hall probes; the Rutherford Appleton Laboratory for preparing two mask sets for the different Hall probe designs; the Max Planck Institute in Stuttgart for fabricating the Pb-gated 10μm Hall bars described at the beginning of Chapter 5; R.E. Somekh of the Department of Materials, University of Cambridge for supplying the Nb film investigated in Chapter 6; R.G. Humphreys of the DRA Malvern for supplying the patterned YBCO film investigated in Chapter 7. I would also like to thank Bob Draper for helping to build the cryostat and his advice concerning all practical matters; the university glass blower Mike Lock for building not one but two helium dewars; Andrey Geim for useful suggestions and discussions and for supplying the micrograph in Figure 5.2; Wendy Lambson for keeping the clean room clean and stocked up with necessities; Andy Peck for taking the electron micrograph in Figure 5.1; the librarians of Reading University for not losing their copy of Tinkham's *Introduction to Superconductivity*; the other members of the group - Zul, Virginia, Geoff, Mark, Dan and Ahmet for sharing the ups and downs of research and for the high spirits in the lab, particularly on Fridays.

My special gratitude is reserved for my wife Francesca for her patience and support.

Contents

Figure Captions

Chapter 4

Chapter 5

Chapter 6

Chapter 7

Tables

Chapter 3

Chapter 6

Chapter 1

Introduction

1.1. Motivation

High-temperature superconductivity was discovered in 1986 but despite an intense research effort, it remains poorly understood and practical applications are still in their infancy. Most applications require current transport with zero resistance in strong magnetic fields, but the resistance of the high-temperature (high-T_c) materials is slow to disappear in even moderate magnetic fields. Attempts to understand this behaviour have been the subject of a number of recent reviews[1, 2, 3]. In comparison with conventional materials, the mixed state of the high-T_c superconductors displays complex behaviour because of the greater importance of thermal fluctuations and the anisotropy of the copper oxide planes. The desire to understand the new physical phenomena and the prospect of applying this knowledge to practical applications have resulted in high-T_c superconductors attracting a great deal of attention.

Resistance in the mixed state is believed to originate from flux vortex motion driven by the Lorentz force. The mixed state is usually investigated through transport and magnetization measurements carried out on bulk samples which cannot directly give information about the microscopic behaviour of flux vortices. The flux vortex is fundamental to most theoretical approaches to the mixed state and consequently there is interest in techniques for detecting individual vortices. Examples are flux decoration[4], imaging in planar Josephson junctions[5, 6], SQUIDs[7, 8, 9], scanning tunnelling microscopy[10], and Lorentz microscopy[11]. Each technique has its limitations and some

are often laborious to apply. In this thesis, microscopic Hall probes are used to observe flux vortices in type II superconducting films, with the aim of investigating their static and dynamic properties.

Hall probes have been used by many workers as a local probe of the magnetic field distribution in superconductors[12, 13, 14] but seldom with the high spatial resolution achieved in this thesis. The two-dimensional electron gas (2DEG) found in a GaAs/ $Al_xGa_{1-x}As$ heterostructure provides a suitable detector with an excellent combination of high sensitivity and low noise. It can be patterned using conventional photolithographic techniques or electron-beam lithography to sub-micron dimensions. Hall bar structures with characteristic dimensions greater than about 10μm measure the local flux density averaged over a large number of flux quanta. By reducing the dimensions of the Hall bar, the spatial resolution of the detector can be increased to the 'quantum limit' of a single flux vortex. Spatial resolution is largely determined by the area of the Hall probe, but the separation between the Hall probe and the superconductor must also be taken into account. The inhomogeneous flux distribution of the mixed state decays rapidly outside the superconductor and the Hall probe separation must be equivalent to the flux line lattice constant if vortex resolution is to be achieved.

In order to emphasise their advantages, the micron-sized Hall probes are compared with other methods for detecting flux vortices below. Flux decoration[4] employs small ferromagnetic particles which collect where the local magnetic field is strongest. Vortices can only be resolved in low magnetic fields and at low temperatures. In addition, the vortices must be stationary and it is not practical to decorate the same piece of superconductor more than once. In contrast, Hall probes can be used over a wide temperature range (0-150K) and provide time-resolved information, giving a dynamic picture of flux behaviour. Planar Josephson junctions can be used to detect the position of a single vortex by measuring the Fraunhofer diffraction pattern for the critical current vs. applied magnetic field which is distorted

according to the vortex location[5, 6]. The superconductor under investigation is a thin film making up one side of the junction. This method has been used to find pinning forces for single vortices over a limited range of temperatures and materials. In this thesis, Hall probes have been used to make similar measurements but without the same restrictions as to temperature and material.

SQUIDs are capable of extremely sensitive magnetic field measurements and have been used to detect the movement of a fluxon in the superconducting strip making up the SQUID loop[7]. SQUIDs have also been scanned over a superconducting surface[8, 9] to investigate the spatial distribution of magnetic field, but resolution is limited by the relatively large area of the superconducting loop. A SQUID is also restricted to temperatures and magnetic fields below the critical values of its superconducting components. The spatial resolution of a Hall probe is limited to ~0.1μm because the Hall voltage is quenched in a quasi-1D channel[15]. In Figure 1.1 the spatial resolution and sensitivity of SQUIDs and the flux decoration technique are compared with Hall probes.

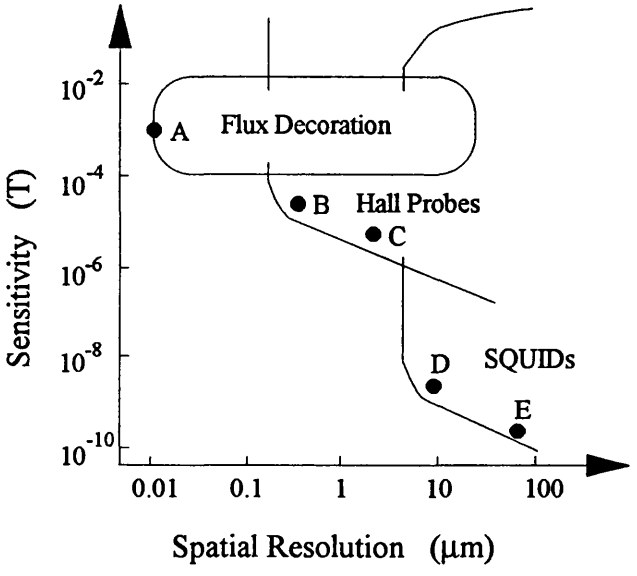

Figure 1.1. A comparison of the spatial resolution and magnetic sensitivity obtainable with flux decoration, Hall probes and SQUIDs. The points A - E were found in the following references : A - Ref. 19, B - Ref. 18, C - this thesis, D - Ref. 9, E - Ref. 8.

Scanning probe microscopies have recently provided some spectacular images of the flux line lattice. The flux lattice in $NbSe_2$ has been imaged by a scanning tunnelling microscope[10], however problems with surface quality have hindered investigations on high-T_c materials[16]. A magnetic force microscope can also image flux structures, but the strong magnetic field of the magnetic tip strongly perturbs the flux lattice and can actually be used to nucleate large vortex bundles[17]. In contrast a scanning Hall probe[18] is non-invasive because the self-field of the probe is negligible. Finally, Lorentz microscopy provides real time images of vortex motion[11] but must be carried out in a specially designed electron microscope and is restricted to very thin samples as the electron beam must pass through the material.

1.2. Overview of Thesis

Three different type II superconductors were studied : films of Pb, Nb and $YBa_2Cu_3O_{7-\delta}$ (YBCO). The properties of type II superconductors are reviewed in Chapter 2, with emphasis placed on the properties of flux vortices and the mixed state. The aim of the chapter is not to provide a comprehensive review of an extensive body of work, but to introduce concepts relevant to later chapters. Chapter 3 describes the semiconductor heterostructures used for the Hall probes and explains how the 2DEG behaves in the weak inhomogeneous magnetic fields found near a superconducting surface. The experimental work was carried out using hybrid semiconductor/ superconductor structures which are described in Chapter 4, together with the experimental apparatus. Detailed notes concerning the fabrication of the Hall probes are relegated to Appendix A.

The experimental results for the Pb, Nb and YBCO films are presented in Chapters 5, 6 and 7 respectively. In the case of the Pb films, the separation between the superconductor and Hall probe was made as small as possible by evaporating the material directly onto the surface of the Hall probes. Pb and Pb(1% In) films were

investigated using Hall probes with characteristic dimensions from 10μm down to 2μm. At the 10μm scale, it was just possible to observe the movement of small bundles of flux into and out of the superconductor. The 2μm probes were most useful because they were small enough to resolve single fluxons, permitting the observation of single and collective vortex phenomena. By sweeping the applied magnetic field around a hysteresis loop and taking measurements at pairs of Hall probes separated by a small distance, it was possible to study the entry and exit of flux bundles. When the mean vortex spacing and temperature were altered, the interplay between pinning forces and vortex interactions could be investigated. A transport current was driven through the superconductor in order to apply a Lorentz force to the vortices, opening up the possibility of measuring pinning forces and observing the crossover from flux creep to flux flow. A similar series of experiments was carried out on the Nb and YBCO films, also using 2μm Hall probes. The results are summarized in Chapter 8 and some suggestions made for future investigations.

Chapter 2

Type II Superconductors and the Mixed State

2.1. Introduction

When a superconductor is cooled through its critical temperature, it enters the superconducting state which is characterized by the disappearance of electrical resistance and the complete or partial expulsion of magnetic field from the superconductor. The microscopic origin of superconductivity is described by the Bardeen-Cooper-Schrieffer (BCS) theory which forms the basis of the modern picture of conventional superconductivity. Superconductivity is a broad field and the BCS theory will not be dealt with here. There are many different superconducting elements and compounds but their behaviour in a magnetic field separates them into just two classes, referred to as type I and type II. The following discussion begins with the phenomenological theories that describe type II superconductors and their behaviour in magnetic fields. After introducing the mixed state found in type II superconductors, the chapter continues with a description of flux vortices and their various interactions. The final sections on superconducting films and high-temperature superconductors are included for their relevance to the measurements discussed in later chapters.

2.2. Type I and II Superconductors

A superconductor cooled through its critical temperature T_c in a weak magnetic field expels the field from its bulk as illustrated in Figure 2.1. This expulsion, called the Meissner effect, is effected by supercurrents that flow in a thin surface layer and screen

the magnetic field from the interior. As the applied magnetic field is increased, the superconductor will behave in one of two different ways, giving rise to the two *H-T* phase diagrams in Figure 2.2 for type I and type II materials. For a type I material, the Meissner effect persists up to a critical field $H_c(T)$ beyond which superconductivity is destroyed and the material becomes normal with uniform magnetic field penetration. The resulting magnetization of a type I superconductor is illustrated in Figure 2.3, with perfect diamagnetism holding up to $H_c(T)$. In contrast, the phase diagram of a type II material shows an additional phase. The Meissner effect persists up to a lower critical field $H_{c1}(T)$, whereupon the material enters the mixed state where normal and superconducting regions coexist. Magnetic flux enters the material in the normal regions, causing a reduction of the magnetization. Only at the upper critical field $H_{c2}(T)$ does the material become fully normal. Note that the phase diagrams and magnetization curves in Figures 2.2 and 2.3 apply to the ideal case of a long thin cylinder in a parallel applied magnetic field. Other geometries give more complicated behaviours which will be discussed later.

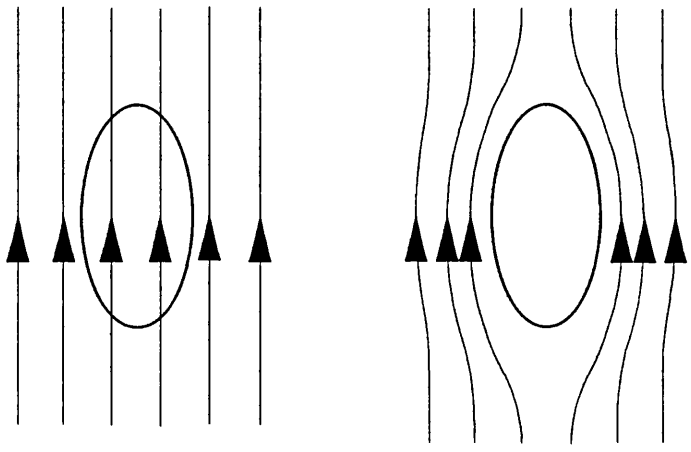

Figure 2.1. Behaviour of a superconductor as it is cooled through T_c in a weak magnetic field.

In order to understand why there are two classes of superconductors, it is necessary to consider the surface energy of the interface between normal and superconducting regions. This surface energy is determined by two fundamental lengths in the superconductor : the penetration depth λ which is the characteristic depth of magnetic field penetration, and the coherence length ξ which is the distance over which the superconducting order parameter changes. λ and ξ are introduced in the following sections.

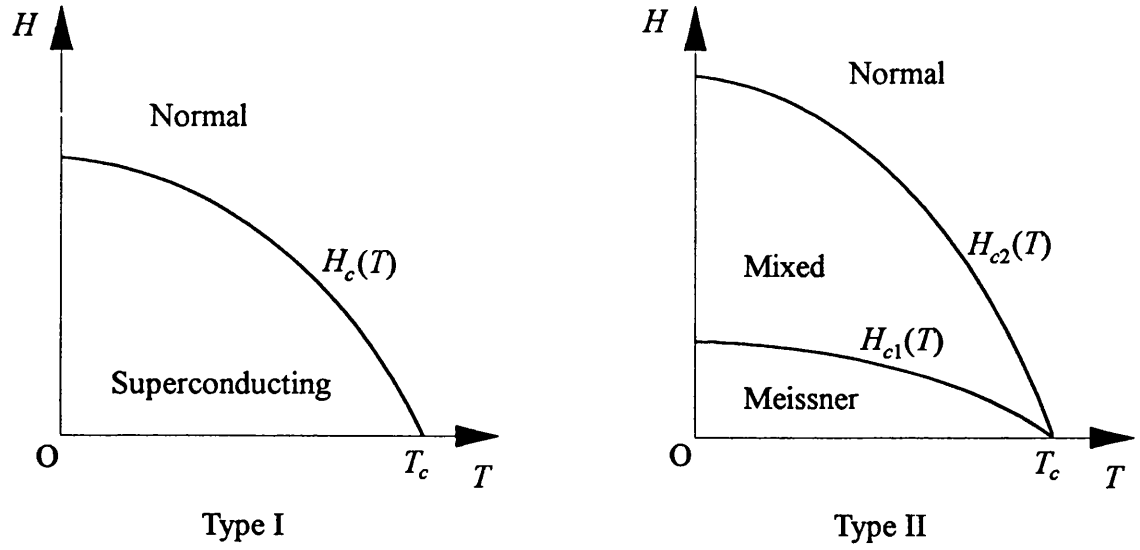

Figure 2.2. Phase diagrams of type I and type II superconductors.

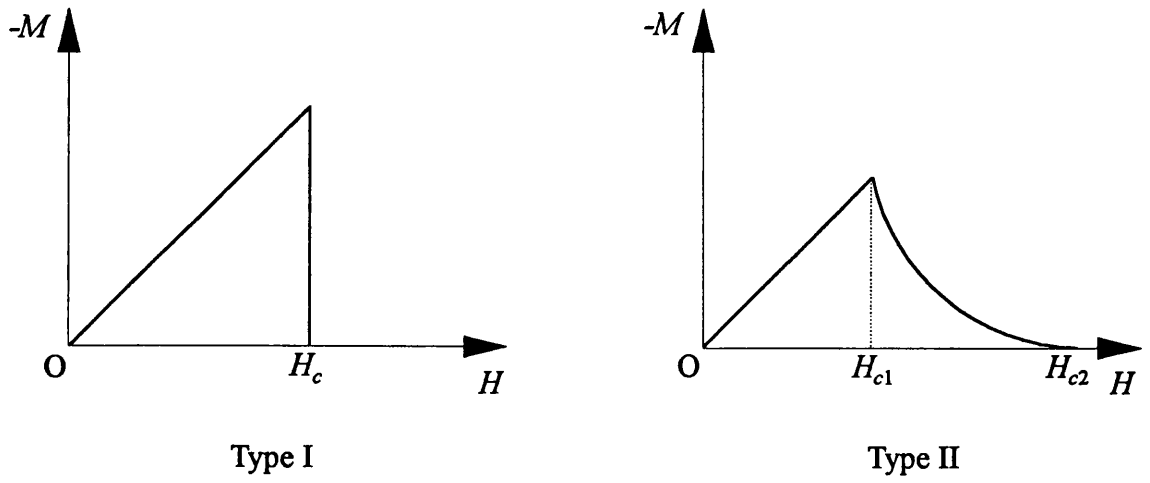

Figure 2.3. Magnetization curves of type I and type II superconductors.

2.3. The London Equations

The screening currents that flow at the surface of a superconductor in the Meissner state must occupy a finite layer. The applied magnetic field does not fall to zero abruptly, but dies away within this surface layer, over a characteristic length called the penetration depth λ. The penetration depth is treated in a quantitative way by the London equations, which give a phenomenological description of the electrodynamics of a type I superconductor :

$$\frac{d\mathbf{j}}{dt} = \frac{n_s q_s^2}{m_s}\mathbf{E} \tag{2.1}$$

and

$$\mathbf{B} = -\frac{m_s}{n_s q_s^2}\nabla \times \mathbf{j} \tag{2.2}$$

where $\mathbf{j}$ is the supercurrent density and n_s the density of the supercurrent carriers or Cooper pairs. m_s and q_s are the mass and charge of the Cooper pairs, equal to $2m$ and $2e$ respectively. The first London equation (2.1) describes a perfect conductor - an electric field produces a current that continuously increases with time. The second equation (2.2) is introduced to describe the Meissner effect. The London equations may be applied to describe the spatial variation of magnetic field within a superconductor. Combining one of Maxwell's equations $\nabla \times \mathbf{B} = \mu_0 \mathbf{j}$ and the second London equation (2.2) yields the equation

$$\begin{aligned}\mathbf{B} &= -\frac{m_s}{\mu_0 n_s q_s^2}\nabla \times \nabla \times \mathbf{B} \\ &= \lambda_L^2 \nabla^2 \mathbf{B}\end{aligned} \tag{2.3}$$

after applying a vector identity and with $\lambda_L = \sqrt{\frac{m_s}{\mu_0 n_s q_s^2}}$. Consider a semi-infinite superconductor filling all space $x \geq 0$ and with a uniform flux density $\mathbf{B}_a$ applied outside parallel to the boundary. A one-dimensional form of Equation (2.3) is sufficient to describe this situation : $B(x) = \lambda_L^2 \frac{\partial^2 B(x)}{\partial x^2}$ which has a solution

$$B(x) = B_a \exp(-x/\lambda_L). \tag{2.4}$$

Thus the flux density inside the superconductor decays exponentially over the distance λ_L which is called the London penetration depth. Because the density of superelectrons n_s is temperature dependent, so too is λ_L. The experimentally observed temperature dependence is well approximated by

$$\lambda_L(T) = \lambda_L(0)\left(1-t^4\right)^{-1/2} \tag{2.5}$$

where the reduced temperature $t = T/T_c$ and typically $\lambda_L(0) \sim 50\text{nm}$.

2.4. Ginzburg-Landau Theory

In the mixed state of a type II superconductor, the material is no longer perfectly diamagnetic, so we expect that the external magnetic field enters in some way. In fact, normal and superconducting phases coexist in the interior and there is a corresponding spatial modulation of the superelectron density. The London theory has a number of limitations, among them the assumption that the density of superelectrons is constant over the entire sample. The Ginzburg-Landau theory overcomes this restriction, leading to a new characteristic length ξ for the spatial variation in the density of Cooper pairs. An assumption is made that the behaviour of the superelectrons may be described by a function $\psi(\mathbf{r})$ which has the property that $|\psi(\mathbf{r})|^2$ is equal to the local concentration of superconducting electrons $n_s(\mathbf{r})$. In addition, it is also assumed that $\psi(\mathbf{r})$ can be used as an order parameter for the second order superconducting phase transition. Thus close to the critical temperature and in zero applied magnetic field, the free energy density of a superconductor f_s can be expanded as

$$f_s(\mathbf{r}) = f_n + \alpha(T)|\psi(\mathbf{r})|^2 + \tfrac{1}{2}\beta(T)|\psi(\mathbf{r})|^4 + \ldots \tag{2.6}$$

with f_n the free energy density of the normal phase. $\psi(\mathbf{r})$ vanishes as T approaches T_c so close to the transition terms of higher order may be ignored. The coefficients α and β are easily determined as follows. The superconductor is thermodynamically stable

when its free energy is at a minimum which requires

$$|\psi|^2 = -\frac{\alpha}{\beta} \quad \text{and} \quad \alpha < 0. \tag{2.7}$$

In addition, the thermodynamic critical field H_c which is the magnetic field at which the magnetic energy equals the superconducting condensation energy is determined by

$$\tfrac{1}{2}\mu_0 H_c^2 = f_n - f_s = -\alpha|\psi|^2 - \tfrac{1}{2}\beta|\psi|^4. \tag{2.8}$$

From Equations 2.7 and 2.8, it follows that $\alpha = -\mu_0 \frac{H_c^2}{n_s}$ and $\beta = \mu_0 \frac{H_c^2}{n_s^2}$.

When magnetic fields are present, the free energy density becomes

$$f_s(\mathbf{r}) = f_n + \alpha|\psi|^2 + \tfrac{1}{2}\beta|\psi|^4 + \tfrac{1}{2m_s}\left|(-i\hbar\nabla - q_s\mathbf{A})\psi\right|^2 + \tfrac{1}{2}\mu_0|H_e - H_i|^2 \tag{2.9}$$

where H_e is the external applied magnetic field and H_i the internal field. Of the two new terms, the first accounts for increases in energy due to spatial variation of ψ and the kinetic energy of the supercurrents. The last term $\frac{1}{2}\mu_0|H_e - H_i|^2$ is the magnetic energy. The total free energy is the integral of $f_s(\mathbf{r})$ over the entire volume of the superconducting specimen : $F = \int_V f_s(\mathbf{r})dV$. By minimizing this with respect to $\psi(\mathbf{r})$ and $\mathbf{A}(\mathbf{r})$, the Ginzburg-Landau equations are obtained :

$$\alpha\psi + \beta|\psi|^2\psi + \frac{1}{2m_s}(-i\hbar\nabla - q_s\mathbf{A})^2\psi = 0 \tag{2.10}$$

$$\mathbf{j} = \frac{-iq_s\hbar}{2m_s}(\psi^*\nabla\psi - \psi\nabla\psi^*) - \frac{q_s^2}{m_s}\psi^*\psi\mathbf{A}. \tag{2.11}$$

We shall use these equations in two simplified situations to get expressions for the characteristic lengths $\lambda(T)$ and $\xi(T)$.

Consider an interface between a normal and a superconducting region. The normal region must be maintained by the presence of the critical magnetic field. To find the coherence length $\xi(T)$, we look at the limiting case of an extreme type I

superconductor which has $\lambda << \xi$. This allows us to neglect the penetration of the magnetic field into the superconductor. If there is no magnetic field in the superconducting region, then we can choose $\mathbf{A} = 0$ and Equation (2.10) becomes

$$\alpha\psi + \beta|\psi|^2\psi + \frac{\hbar^2}{2m_s}\nabla^2\psi = 0. \tag{2.12}$$

The solution subject to the boundary conditions $\psi(0) = 0$ and $\psi \to \psi_0$ as $x \to \infty$ is $\psi(x) = \sqrt{\frac{\alpha}{\beta}}\tanh\left(x/\sqrt{2}\xi\right)$ with the coherence length given by $\xi^2(T) = \frac{\hbar^2}{2m_s|\alpha|}$.

To find the penetration depth, we consider a weak magnetic field present in the superconductor. This allows $|\psi|^2$ to be replaced by its equilibrium value $|\psi_0|^2$ in the second Ginzburg-Landau equation (2.11). Taking its curl, we get the London-type equation $\nabla \times \mathbf{j} = -\frac{q_s^2}{m_s}\psi_0^2\mathbf{B}$ which yields the penetration depth $\lambda^2(T) = \frac{m_s}{\mu_0 q_s^2 \psi_0^2}$, agreeing with the London value. Both characteristic lengths are proportional to $(1-t)^{-1/2}$ near T_c.

2.5. The Ginzburg-Landau Parameter

It is useful to introduce the Ginzburg-Landau parameter κ which is the dimensionless ratio of the two characteristic lengths :

$$\kappa = \frac{\lambda(T)}{\xi(T)}. \tag{2.13}$$

κ does not change with temperature because λ and ξ have the same temperature dependence according to the Ginzburg-Landau theory discussed in the previous section. In reality this is not strictly true and κ does show a weak variation with temperature.

2.6. The Interfacial Energy

The two lengths ξ and λ enable us to determine the surface energy of the interface between normal and superconducting regions. Considering such an interface in a homogeneous material at constant temperature, in the normal region $H \geq H_c$ while in the superconducting region, the magnetic field decays within a thin layer of thickness ~λ. In a similar way the order parameter rises from zero in the normal region to the bulk equilibrium value over the length ξ in the superconducting region. Figure 2.4 illustrates the two cases, $\lambda < \xi$ and $\lambda > \xi$.

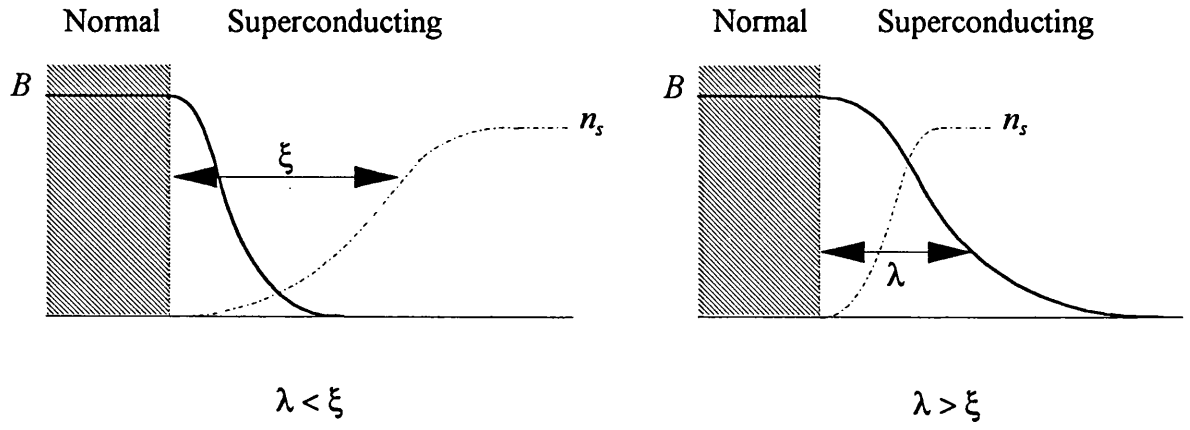

Figure 2.4. Interface between normal and superconducting phases for $\lambda < \xi$ and $\lambda > \xi$.

For the interface to be stable, the system must be at equilibrium, that is the free energy densities of the normal and superconducting phases must be equal. There are two energy contributions which change the free energy density of the superconductor relative to the normal material. Upon entering the ordered superconducting phase, the free energy density of the material decreases by an amount $f_n - f_s$, while the exclusion of the applied magnetic field increases the free energy density of the superconductor by an amount $\frac{1}{2}\mu_0 H_c^2$. Because the interface is at equilibrium, well inside the superconductor the two contributions must cancel, that is $\frac{1}{2}\mu_0 H_c^2 = f_n - f_s$. At the interface the order parameter ψ rises from zero over a distance ξ, so the decrease in the free energy density due to the electron ordering takes place over the same distance.

For an interface of area A, the volume of the superconducting region decreases by $\sim A\xi$, making a positive contribution of about $(f_n - f_s)A\xi$ to the free energy of the interface. Likewise the penetration of the magnetic field into the superconducting phase means that the increase in the magnetic energy takes place over the penetration depth λ, giving a negative energy contribution of approximately $\frac{1}{2}\mu_0 H_c^2 A\lambda$. In general λ does not equal ξ and the two contributions do not cancel, giving rise to a free energy per unit area

$$\sigma = \tfrac{1}{2}\mu_0 H_c^2(\xi - \lambda). \qquad (2.14)$$

The surface energy changes sign from negative to positive when ξ equals λ, that is when $\kappa = 1$. A more precise calculation using Ginzburg-Landau theory shows that the change of sign of the surface energy takes place at $\kappa = \frac{1}{\sqrt{2}}$. So for $\kappa < \frac{1}{\sqrt{2}}$ the surface energy is positive and for $\kappa > \frac{1}{\sqrt{2}}$ the surface energy is negative.

2.7. The Mixed State

When type II superconductors were introduced in Section 2.2, we saw that for applied fields between H_{c1} and H_{c2} the superconductor enters the mixed state with coexisting normal and superconducting regions, that is there will be normal-superconducting interfaces. Now that we have calculated the free energy associated with these interfaces, it is possible to understand in a qualitative way the distinction between type I and type II superconductors. If the surface energy is positive ($\kappa < \frac{1}{\sqrt{2}}$), the superconductor will have the lowest possible free energy if the interfacial area is minimized. This is a type I superconductor. On the other hand, if the surface energy is negative ($\kappa > \frac{1}{\sqrt{2}}$), the free energy of the superconductor will be minimized by the introduction of as many normal-superconducting interfaces as possible, a situation realized by the mixed state of a type II superconductor.

Most pure elements are type I superconductors while alloys or impure metals

usually exhibit type II superconductivity. The reason is that impurities in a metal cause additional scattering of electrons, reducing the electron mean free path l^*. Both λ and ξ depend on the electron mean free path, but while the penetration depth only increases slightly with a decrease in l^*, the coherence length falls rapidly as $\sqrt{l^*}$ and κ increases accordingly. Even a small number of impurities can increase κ sufficiently to produce type II behaviour.

2.8. The Abrikosov Flux Lattice

In the mixed state, because there is magnetic flux in the interior of the superconductor, there must also be supercurrents flowing in closed loops for a steady state. The problem of the spatial variation of B and j inside the superconductor was solved by Abrikosov, who found a periodic solution of the Ginzburg-Landau equations where the magnetic flux penetrating the superconductor is divided into cylinders called flux vortices arranged on a regular triangular lattice. The vortex consists of a normal core to which the magnetic flux is confined by a circulating supercurrent flowing around the core. The structure of a vortex is illustrated in Figure 2.5. The radius of the normal core of a vortex is approximated by ξ, while the extent of the magnetic field is given by λ.

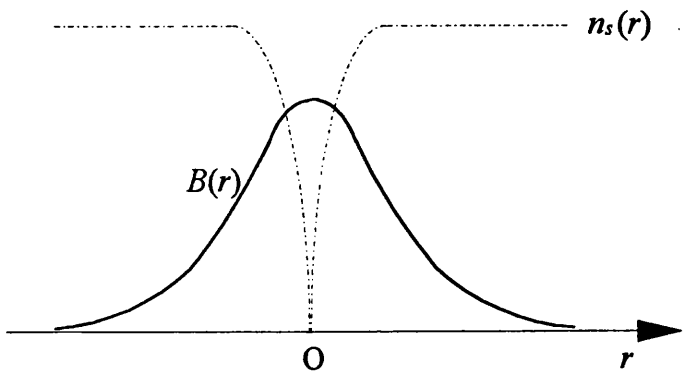

Figure 2.5. Variation of flux density and superelectron density across a flux vortex.

A certain amount of energy is required to create the normal core but this is offset by the gain in magnetic exclusion energy. At H_{c1} flux begins to penetrate because the gain in exclusion energy becomes sufficient to create flux tubes in the interior. As the external applied magnetic field is increased, the vortices become more numerous and closely packed, until just below the upper critical field H_{c2} the distance between vortices becomes ~2ξ and it is not possible to treat the vortices individually.

2.9. Flux Quantization

Each vortex contains flux amounting to a single flux quantum $\Phi_0 = \frac{h}{2e} = 2.068 \times 10^{-15}\,\mathrm{Wb}$. This quantization of flux is a consequence of the use of the single-valued order parameter ψ to describe the superconducting state. From the second Ginzburg-Landau equation, the supercurrent is given by

$$\mathbf{j} = -\left(\frac{q_s^2}{m_s}\mathbf{A} + \frac{q_s\hbar}{2m_s}\nabla\phi\right)|\psi|^2 \tag{2.15}$$

where ϕ is the phase of the complex order parameter $\psi \exp(i\phi)$. If $\mathbf{j}$ is integrated along a closed path around an isolated flux vortex at a distance large enough for there to be no current, then

$$0 = \oint \mathbf{j}\cdot\mathbf{dl} = \oint\left(\frac{q_s^2}{m_s}\mathbf{A} + \frac{q_s\hbar}{m_s}\nabla\phi\right)\cdot\mathbf{dl} \tag{2.16}$$

From Stoke's theorem we have $\oint \mathbf{A}\cdot\mathbf{dl} = \int \nabla\times\mathbf{A}\cdot\mathbf{dS} = \int \mathbf{B}\cdot\mathbf{dS} = \Phi$ where Φ is the total flux enclosed by the path. The second term $\oint \nabla\phi\cdot\mathbf{dl} = 2\pi n$ with n an integer because the phase must change by a multiple of 2π for the order parameter to remain single-valued. Recalling that $q_s = 2e$, we find that $\Phi = \frac{nh}{2e}$. The solution with $n = 1$ gives the flux quantum Φ_0, the smallest possible non-zero quantity of flux that a vortex can contain.

2.10. Vortex Interactions

The vortices arrange themselves in the Abrikosov flux lattice in an ideal superconductor or one with very weak pinning. There is a repulsive interaction between vortices and the lowest energy state is usually a regular hexagonal lattice with vortices on the vertices of equilateral triangles. The interaction between two vortices is due to the Lorentz force exerted by the supercurrent of one vortex on the magnetic flux of the other. The force per unit length exerted on flux line 2 by the supercurrents of flux line 1 is

$$\mathbf{f}_2 = \mathbf{j}_1(\mathbf{r}_2) \times \Phi_0 \tag{2.17}$$

where Φ_0 is a vector of magnitude the flux quantum directed along the length of the vortex and $\mathbf{j}_1(\mathbf{r}_2)$ is the supercurrent due to vortex 1 at position 2. Using the supercurrent density of the London vortex described in the next section, in the limit of large vortex separations $r_2 >> \lambda$ the magnitude of the force per unit length is[19]

$$f_2 = \frac{\Phi_0^2}{2\pi\mu_0\lambda^3}\sqrt{\frac{\pi\lambda}{2r_2}}\exp(-r_2/\lambda). \tag{2.18}$$

2.11. Vortex Models

The magnetic field distribution of a vortex must obey the Ginzburg-Landau equations which require lengthy numerical solution. A simple description of the magnetic field distribution is given by the London model[19] which assumes that a vortex consists of a normal core of radius ξ embedded in the superconducting phase. With the restriction that $\kappa >> 1$, that is the diameter of the vortex is small, the London model is a good approximation at fields in the range $H_{c1} < H << H_{c2}$ where the vortices are sufficiently widely spaced for the structure of the core to be unimportant and interactions between the vortices are weak.

However the London model fails in the core region where the magnetic flux

density diverges at the centre because the depression of the superconducting order parameter to zero on the vortex axis is not taken into account. This is unphysical and we must look elsewhere in order to get a useful idea of the flux distribution for the Pb films investigated later which have $\kappa \approx 1$ and in some instances strongly interacting vortices.

A useful improvement on the London model is given by Clem[20]. The Clem model gives a realistic description of the vortex core and has also been extended to arbitrary vortex density[21]. To begin with, we consider the flux distribution of an isolated vortex. Inside the vortex core, the order parameter is approximated by a simple variational trial function. Clem assumes that the normalized order parameter is of the form $\psi(r) = f(r)\exp(-i\phi)$ with the magnitude $f(r) = r/R$ where r is the radial coordinate and $R = (r^2 + \xi_v^2)^{1/2}$. ξ_v is a variational core radius parameter of order ξ, the Ginzburg-Landau coherence length. ξ_v is calculated variationally in the way outlined below.

Placing the isolated vortex on the z-axis and using the second Ginzburg-Landau equation, the magnetic flux density is calculated to be

$$B_z = \frac{\Phi_0}{2\pi\lambda\xi_v}\frac{K_0(R/\lambda)}{K_1(\xi_v/\lambda)} \tag{2.19}$$

where $K_0(x)$ and $K_1(x)$ are modified Bessel functions and λ is the penetration depth. To find ξ_v Clem calculates the Ginzburg-Landau free energy density associated with the vortex and from that, the energy per unit length of the vortex line $\varepsilon_\ell = \frac{\Phi_0}{4\pi}\sqrt{2}H_c\left[\frac{\kappa}{8}\left(\frac{\xi_v}{\lambda}\right)^2 + \frac{1}{8\kappa} + \frac{\lambda}{2\kappa\xi_v}\frac{K_0(\xi_v/\lambda)}{K_1(\xi_v/\lambda)}\right]$. The energy per unit length is at a minimum with respect to the variational parameter ξ_v when ξ_v satisfies

$$\kappa = \frac{\sqrt{2}}{\xi_v'}\left[1 - \frac{K_0^2(\xi_v')}{K_1^2(\xi_v')}\right]^{1/2} \tag{2.20}$$

where $\xi_v' = \xi_v/\lambda$. Clem finds that the energy minimum is at most only a few percent

higher than the value obtained from an exact numerical solution of the Ginzburg-Landau equations. In Figure 2.6, $\kappa\xi_v' = \xi_v / \xi$ is plotted against $1/\kappa$ and it can be seen that $\xi_v \sim \xi$ for a wide range of values of κ. To find ξ_v for a superconductor of known κ, the simplest procedure is to read the value off the figure.

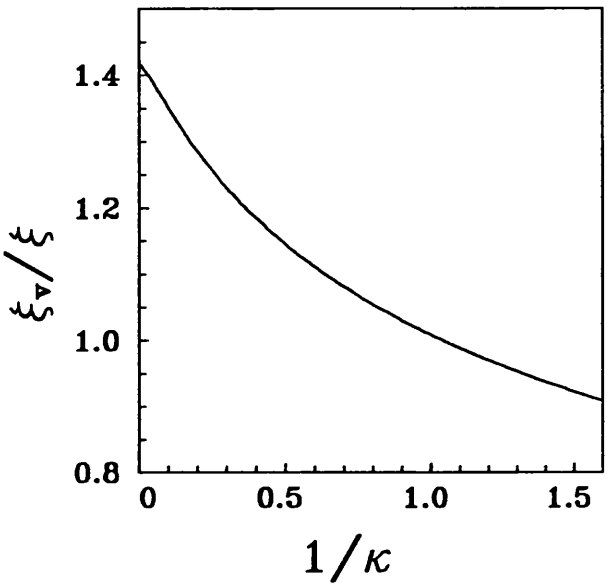

Figure 2.6. The ratio ξ_v/ξ plotted against $1/\kappa$.

It is possible to extend the model for an isolated vortex to a flux line lattice by making a linear superposition of the magnetic field contributions of the individual flux lines[21]. The local flux density can be obtained for arbitrary κ values and flux lattice spacings, provided that the overlap between vortices is accounted for by introducing a field-dependent penetration depth λ_{eff} which must be calculated using the correct spatially dependent magnitude of the order parameter appropriate for the given flux line spacing : $\lambda_{eff} = \frac{\lambda}{\sqrt{\overline{f^2(B)}}}$. Here $\overline{f^2(B)}$ is the spatial average of the order parameter for the applied magnetic flux density B. The effective penetration depth λ_{eff} reduces to the weak field penetration depth λ at low average flux density, increases as B increases and diverges as B approaches the upper critical field.

The field distribution of a single vortex in a lattice is found in the same way as

for the isolated vortex considered in the variational model above, just replacing λ with the effective field-dependent penetration depth λ_{eff}. A linear superposition of all the individual contributions leads to a periodic field distribution

$$B(\mathbf{r}) = B\sum_{\tau} F(\tau)\exp(i\tau\cdot\mathbf{r}) \tag{2.21}$$

where the sum is over all reciprocal lattice vectors τ, B is the applied magnetic flux density and the form factor $F(\tau) = \dfrac{K_1(Q\xi_v)}{Q\lambda_{eff}K_1(\xi_v/\lambda_{eff})}$ with $Q = \left(\tau^2 + \lambda_{eff}^{-2}\right)^{-1/2}$.

To compute $B(\mathbf{r})$, λ_{eff} and ξ_v must be known. Clem[21] provides a formula for the spatial average of the order parameter $\overline{f^2} = 1-(2+S_2)x+(1+S_2)x^2$ where $x = B/H_{c2}$ and $S_2 = -\left[\beta_A - (\beta_A - 1)/2\kappa^2\right]^{-1}$ with $\beta_A = 1.1596$. ξ_v can be found using Figure 2.6. The reciprocal lattice vectors of the real space hexagonal flux lattice must also be known. If the average flux density in the superconductor is B, then the lattice constant is $a = \sqrt{\dfrac{2\Phi_0}{\sqrt{3}B}}$ and the reciprocal lattice vectors are $\tau = n\tau_1 + m\tau_2$ with $\tau_1 = \left(\dfrac{2\pi}{a}, -\dfrac{1}{\sqrt{3}}\dfrac{2\pi}{a}\right)$ and $\tau_2 = \left(0, \dfrac{2}{\sqrt{3}}\dfrac{2\pi}{a}\right)$.

The Clem model is subject to the same theoretical limitations as the Ginzburg-Landau equations, in particular, temperatures are restricted to the immediate vicinity of the superconducting transition. It is not an exact solution of the Ginzburg-Landau equations, but it is an improvement over the London model, giving a realistic behaviour of the magnetic flux density in the vortex core. The Clem model agrees satisfactorily with experiment and with results from lengthy numerical solution of the Ginzburg-Landau equations. It is used in Chapter 4 to calculate the magnetic field distribution at and close to superconducting surfaces.

2.12. The Critical Current

Just as there is a critical magnetic field, so too there is a critical current density

j_c which, if exceeded, causes the superconducting state to break down and resistance to appear. For a superconductor in the Meissner state, there can be no magnetic field in the interior which means that a transport supercurrent is limited to the same thin surface layer in which the screening currents flow. The total surface current density is the sum of the transport and screening current densities and is related to the magnetic field at the surface of the superconductor by the second London equation.

When the surface magnetic field reaches H_{c1}, a type II superconductor enters the mixed state and an ideal material will display a finite resistance even if the transport current is very small. To see how this is possible, consider a plate of type II material in a perpendicular magnetic field $H > H_{c1}$. The applied transport current is not confined to a surface layer, but is distributed across the entire cross-section because there is now magnetic flux inside the superconductor. The flux distribution across a vortex core varies more slowly than the density of superelectrons, so the applied current flows through the core, exerting a Lorentz force on the vortex per unit length :

$$\mathbf{f}_L = \mathbf{j} \times \Phi_0 \tag{2.22}$$

where $\mathbf{j}$ is the current density which is assumed to be uniform and Φ_0 is a vector of magnitude the flux quantum directed along the magnetic field. The reversible magnetization curve of an ideal type II superconductor in Figure 2.3 suggests that free movement of a vortex is possible for the smallest of driving forces, so the vortices drift across the plate under the influence of the Lorentz force. The energy dissipated by the vortex motion is supplied by the applied current and as a result a voltage drop appears along the sample which exhibits an electrical resistance.

2.13. Flux Pinning

A type II superconductor in the mixed state can only sustain a supercurrent if the flux vortices are fixed in place to prevent motion caused by the Lorentz force. A

mechanism is provided by regions of "weaker" superconductivity where there is less superconducting condensation energy and which are energetically favourable for the normal vortex core. Suitable sites are provided by spatial inhomogeneities such as defects in the crystalline structure, grain boundaries, normal precipitates, impurities and voids.

The effect of a pinning centre can be understood by considering the free energy associated with the vortex core. At the centre of a vortex, the density of superelectrons decreases and energy is required to break the Cooper pairs. Approximating the core as a cylinder of normal material of radius ξ, the local increase in free energy per unit length is $\varepsilon \sim \frac{1}{2}\mu_0 H_c^2 \pi \xi^2$. If the flux vortex can pass through a normal region of diameter $l \geq \xi$, it will reduce its length in the superconducting phase and the total free energy decreases by an amount εl. This amount of energy must be provided to move the vortex off the pinning centre. An effective pinning centre has a diameter of the order of ξ, the size of the vortex core. With many pinning centres, the flux tubes try to take up positions that minimise the total energy, allowing for the repulsive interaction between vortices.

The force required to depin a vortex will equal the maximum value of $\frac{d\varepsilon}{dr}$ and in practice it is found from the Lorentz force necessary to move the vortex. The temperature dependence of the pinning force per unit length of a single vortex is often found to obey an empirical power law

$$f_p(t) = f_p(0)(1-t)^n \qquad (2.23)$$

where t is the reduced temperature. The temperature dependence can be crudely estimated[5] by assuming the gain in free energy per unit length of the pinned vortex to be εl_p where l_p is the fraction of the vortex line that is pinned. Near T_c we have the temperature dependences $H_c \propto (1-t)$ and $\xi \propto (1-t)^{-1/2}$. Estimating f_p as $\frac{\Delta\varepsilon}{\Delta\xi}$ gives an overall temperature dependence $f_p \propto (1-t)^{3/2}$. In fact a broad range of values has been

observed for both the exponent n and the zero-temperature pinning force $f_p(0)$, depending on the system investigated. n and $f_p(0)$ are believed to vary according to the type of pinning site involved.

2.14. The Critical State and Flux Creep

Because flux pinning impedes vortex motion, magnetization curves become irreversible when pinning is present. As the applied magnetic field increases past H_{c1}, vortices enter the superconductor but are pinned just within the surface. The pinned vortices cannot move freely in the material, so instead of the uniform vortex density set up in an ideal material, there is a gradient of vortex concentration from the surface inwards. When the applied magnetic field is removed, flux remains trapped within the superconductor.

The non-uniform distribution of flux lines produces a supercurrent j. If j exceeds the critical current density, the vortices rearrange themselves into the critical state with $j \leq j_c$ everywhere in the material and the flux lines stop moving altogether or creep slowly due to thermally activated depinning. Flux creep takes place at finite temperature, as thermal energy allows flux lines to jump from one pinning site to another in response to the driving force of the supercurrent set up by the flux density gradient. Flux creep can also occur in a current-carrying superconductor but the resulting resistive voltage is very small and difficult to observe because of the low velocity of flux creep.

Flux creep is described by the theory of Anderson and Kim[22] which assumes that a single flux line or a bundle of flux lines hops over the potential barrier between adjacent pinning points. For moderate flux densities, a single vortex is unlikely to move because the range of the repulsive vortex interaction is large compared to the typical distance between lines. Local perturbations of the flux line density are energetically unfavourable, and this encourages cooperative motion with a whole bundle of lines

jumping simultaneously. The jump rate is assumed to be of the form $\omega_0 \exp(-U_0 / kT)$ where ω_0 is an attempt frequency and U_0 is the energy barrier between the initial and final vortex configurations. As a rough estimate, Tinkham[23] takes $U_0 = p\frac{1}{2}\mu_0 H_c^2 L^3$ with L a microscopic length of the same order of magnitude as λ and ξ, and p the fraction of the condensation energy in the volume L^3 available as pinning energy. Typically U_0 is very large compared to kT, and so the rate of flux creep is very slow.

2.15. Collective Pinning

Pinning centres are randomly distributed throughout a real material and tend to distort the flux line lattice. Just above H_{c1} when the vortices are widely separated, the location of a flux line is determined by the pinning centres, not by the exponentially small interaction with neighbouring flux lines. There is strong deformation of the flux line lattice and its periodicity is destroyed. In this case, referred to as single particle pinning, each pinning centre acts with maximum force and the average pinning force can be determined from a simple summing procedure. Increasing the flux line density, the vortex interactions become stronger relative to the pinning centres, and short-range order appears over a small volume V_c but there is still no long-range order. When a supercurrent less than the critical value is applied, each volume V_c displaces independently under the Lorentz force by a distance less than ξ so that the resulting pinning force compensates the Lorentz force. Inside V_c the flux lattice is almost perfectly periodic and the pinning centres are randomly distributed, so the pinning forces almost cancel each other. The collective pinning force acting on the volume V_c is equal to $f_p\sqrt{n_p V_c}$ where f_p is the force of interaction at a single pinning centre and n_p is the density of pinning centres[24].

In a superconducting film, the radius of the region in which there is short-range order is given by[24]

$$R_c = \frac{C_{66}\, a}{f_p \sqrt{n_p}} \tag{2.24}$$

where C_{66} is the shear elastic modulus of the flux line lattice and a is the flux line lattice constant. For applied magnetic fields small in comparison to H_{c2}, C_{66} can be determined from the dependence of the magnetic field H on the flux density B obtained from the magnetization of the material[25] : $C_{66} = \frac{1}{2}\int_0^{B_0} B^2 \frac{\partial^2 H}{\partial B^2} dB$. As the magnetic field decreases to H_{c1}, C_{66} falls off rapidly and R_c decreases.

2.16. Superconducting Films

The experimental work presented later in this thesis was carried out on superconducting films in a perpendicular magnetic field. For this particular geometry there are some additional considerations which are addressed in this section. Previously we assumed the specimen to be a long, thin rod in a parallel applied magnetic field so that any distortion of the magnetic field was negligible.

A planar superconductor placed in a weak perpendicular magnetic field H_a will expel the magnetic field by the Meissner effect, causing an intensification of the magnetic field at the edges of the superconductor. The external magnetic field at the perimeter exceeds the applied field strength and is given by

$$H_{edge} = \frac{1}{1-n} H_a \tag{2.25}$$

where n is the demagnetization factor. The superconductor will enter the mixed state when $H_{edge} > H_{c1}$. For a long cylinder parallel to the applied magnetic field $n = 0$, while a sphere has $n = 1/3$. For a thin film in a perpendicular applied magnetic field $n \approx 1$, which means that flux vortices will enter the film almost as soon as the magnetic field increases from zero, ignoring the effect of flux pinning and the existence of any surface barrier to flux entry.

Another consideration is that sufficiently thin films of a type I superconductor enter the mixed state when a perpendicular magnetic field is applied. The theoretical prediction of Tinkham[26] that the mixed state is stable in thin films of type I material was confirmed by decoration experiments[27] which showed that below a critical thickness d_c, type I films assume the mixed state with flux vortices each containing a single flux quantum. Above the critical thickness, vortices containing more than one flux quantum form. For polycrystalline Pb films, $d_c \approx 250\text{nm}$ at 4.2K[27].

As the film thickness decreases below the critical thickness, the perpendicular critical field $H_{c\perp}$ increases, being given by

$$H_{c\perp}(d) = \sqrt{2}\kappa(d)H_c. \qquad (2.26)$$

The Ginzburg-Landau parameter κ depends on d through the electronic mean free path which is shorter in thinner films due to increased scattering at the film surface.

2.17. The Critical State in Thin Films

The critical state is often described by the Bean model which assumes that the flux density gradient and associated current density are either constant or zero, that is in the region where flux has penetrated $|\nabla \mathbf{B}| = \mu_0 j_c$ and $j = j_c$ while elsewhere both quantities are zero. The Bean model applies to long specimens in a parallel magnetic field where there are no demagnetizing effects. For a flat superconductor in a perpendicular magnetic field demagnetizing effects are crucial and complicate the situation, but the idea is retained that flux lines start to move when j reaches the critical value j_c and the critical state is still obtained.

A useful model which applies specifically to a type II superconducting strip in a perpendicular magnetic field has been given separately by Brandt *et al.*[28, 29] and Zeldov *et al.*[30] Analytical solutions are given for the current density and magnetic field distributions in a long flat superconducting strip of width $2W$ and thickness d such that

$2W >> d$. The strip lies in the x-y plane, centred at the origin and running parallel to the x-axis. A uniform magnetic field is applied along the z-direction, producing a supercurrent $j(x,y)$ flowing along the -x direction, limited to a field-independent value j_c. For simplicity j_c is assumed to be independent of magnetic field, but this is not always valid since j_c drops to zero as H_{c2} is approached. Although the material is type II, the model does not distinguish between Meissner surface currents and vortex currents but considers the current density $j(x,y)$ smeared over several flux line spacings and integrated over the film thickness to give $J(y)$. It does not matter whether the film thickness is greater than or less than the penetration depth.

The first step in the calculation is to use Ampere's law to find the perpendicular component of the magnetic field across the width of the strip :

$$H(y) = \frac{1}{2\pi}\int_{-W}^{W} \frac{J(u)du}{y-u} + H_a. \qquad (2.27)$$

$H(y)$ is approximately constant across the entire thickness of the strip. As H_a increases from zero, the flux lines penetrate to a position b so that $H(y) \neq 0$ for $|y| > b$ but $H(y) = 0$ for $-b < y < b < W$. The shielding currents saturate near the edges of the strip, that is $J(y > b) = J_c$ and $J(y < b) = -J_c$. After finding the current distribution in the inner region $|y| < b$ required to satisfy these conditions, it is possible to calculate the magnetic field distribution :

$$\begin{aligned} H(y) &= 0 && \text{for } |y| < b \\ &= H_a \operatorname{arctanh}\left[\frac{(y^2 - b^2)^{1/2}}{c|y|}\right] && \text{for } b < |y| < W \end{aligned} \qquad (2.28)$$

where the position b is given by $b = \dfrac{W}{\cosh(H_a/H_c)}$, $c = \tanh(H_a/H_c)$ and $H_c = J_c/\pi$. $H(y)/H_c$ is plotted in Figure 2.7 across the width of the strip. If H_a is swept up to a maximum value H_0 and then swept around a magnetization loop, the magnetic field is

given by the following linear superpositions for H_a decreasing from $+H_0$ to $-H_0$ and then increasing from $-H_0$ to $+H_0$ respectively :

$$H_{\downarrow}(y,H_a,J_c) = H(y,H_0,J_c) - H(y,H_0 - H_a,2J_c)$$
$$H_{\uparrow}(y,H_a,J_c) = -H_{\downarrow}(y,-H_a,J_c) \qquad (2.29)$$

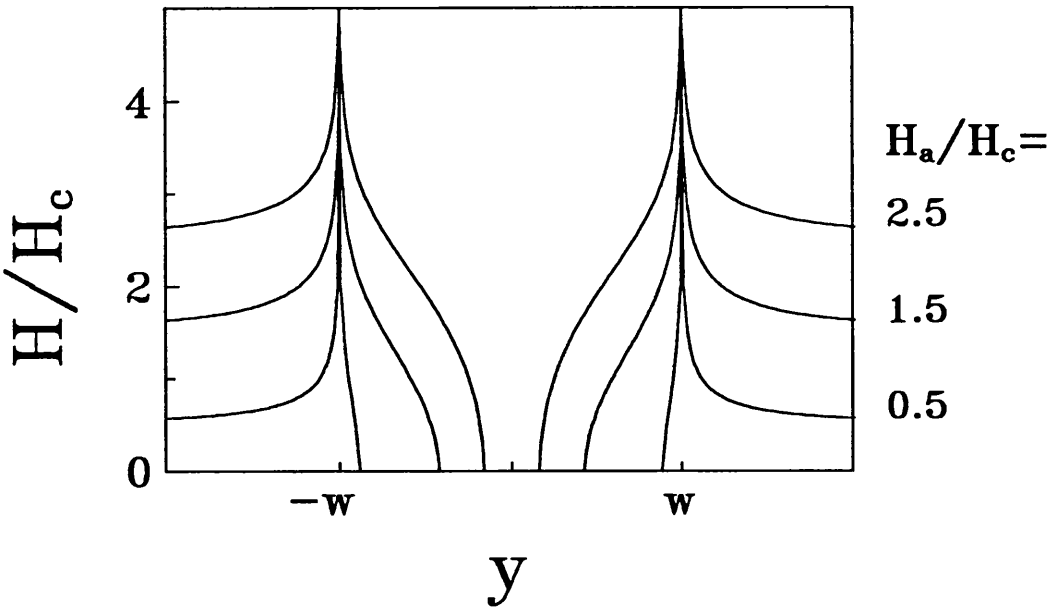

Figure 2.7. Perpendicular magnetic field across a superconducting strip for applied fields $H_a/H_c = 0.5,\ 1.5,\ 2.5$.

Solutions are also given[29, 30] for the magnetic field distribution in a strip carrying a transport current and for a combination of transport current and applied magnetic field. With a transport current and no applied magnetic field, the current flows mostly at the strip edges with $J = J_c$ again up to a position b, dropping away to the centre. The magnetic field component perpendicular to the strip is

$$H(y) = 0 \qquad \text{for } |y| < b$$
$$= H_c \frac{y}{|y|} \operatorname{arctanh}\left(\frac{y^2 - b^2}{W^2 - b^2}\right)^{1/2} \qquad \text{for } b < |y| < W \qquad (2.30)$$

where $b = W\left(1 - I^2/I_{\max}^2\right)^{1/2}$, $H_c = J_c/\pi$ as before and I is the transport current.

2.18. High-temperature Superconductors

High-temperature (high-T_c) superconductors are a recently discovered family of copper-oxide based materials that exhibit type II superconductivity up to temperatures as high as 130K. The materials have a layered structure based on copper oxide planes, resulting in anisotropy which varies from strong in $YBa_2Cu_3O_{7-\delta}$ (YBCO) to extremely strong in $Bi_2Sr_2CaCu_2O_{8+\delta}$ (BSCCO). The microscopic mechanism responsible for the formation of Cooper pairs in these materials has still not received a satisfactory theoretical explanation and is believed to differ from the electron-phonon interaction found in the conventional low-temperature materials. However, many of the phenomenological concepts used to describe the mixed state of low-temperature materials can still be applied.

The present discussion is limited to the unusual properties of the mixed state formed when the high-T_c materials are exposed to a magnetic field. While the superconducting transition is quite sharp in zero magnetic field, it becomes much broader in moderate magnetic fields, in contrast to the behaviour of the low-T_c materials[1, 3]. Resistance in the mixed state is conventionally associated with motion of vortices and it is believed that thermal fluctuations in the high-T_c materials are responsible for additional vortex motion that leads to broadening of the resistive transition. Another mechanism proposed to account for this broadening is Lorentz-force-independent dissipation caused by fluctuations of the superconducting order parameter[3].

Magnetization measurements have led to the observation of an irreversibility line $H_{Irr}(T)$ separating the mixed state into two regions. At magnetic fields and temperatures above the irreversibility line, the changes in the magnetization are reversible, while below they are not and magnetization loops become hysteretic. The irreversibility line is believed to arise from thermal depinning of vortices from pinning sites by thermal fluctuations. A more controversial interpretation of the fluctuation

phenomena is a phase transition[1] where a vortex glass phase melts to form a vortex liquid phase at a melting temperature T_m. These new phases are sketched in Figure 2.8. The effect of pinning is to distort the ideal flux line lattice, producing the vortex glass phase where fluxons reduce their energy by settling into the randomly positioned pinning sites. The pinning force adds to the restoring force from intervortex repulsion, increasing T_m and also broadening the transition.

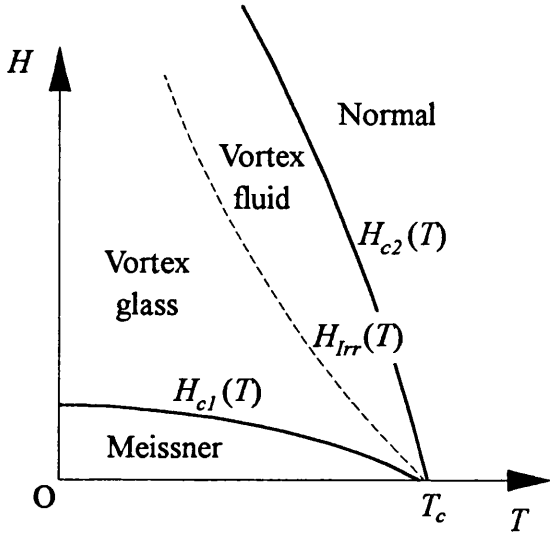

Figure 2.8. Phase diagram of a high-T_c superconductor.

While thermal fluctuations are unimportant in conventional type II materials, there are a number of reasons for their greater importance in high-T_c superconductors. The energy required to create a piece of flux line of length ξ is $U = \frac{1}{2}\mu_0 H_c^2 \xi^3$, where $\frac{1}{2}\mu_0 H_c^2$ is the superconducting condensation energy and ξ^3 is the volume of the normal core. From Ginzburg-Landau theory $H_c = \frac{\Phi_0}{2\sqrt{2}\pi\lambda\xi}$, so U varies as ξ/λ^2. The coherence length in the high-T_c materials is of the order of 10Å, much smaller than coherence lengths found in other materials (typically between 100-1000Å). The penetration depth λ of about 1500Å is somewhat larger than usual because there is a relatively low electron density in the high-T_c materials. Thus U is considerably smaller in the high-T_c materials and close to the larger critical temperatures, the flux vortices

are highly susceptible to thermal fluctuations. Considering a thermal activation factor of the form $\exp(-U/kT)$, it is clear that thermally activated flux creep will occur much more readily.

The strong anisotropy of the layered materials is also important. The weak interactions between the copper oxide planes mean that the vortex line tension is smaller, giving a loosely connected vortex line that is more easily disturbed by thermal fluctuations than is the case in low-T_c materials. In an extremely anisotropic material such as BSCCO, the interactions between the planes are so weak that in a perpendicular applied magnetic field, the vortex lines consist of strings of 2D 'pancake' vortices. As the vortex density increases, the interactions between the pancake vortices in a CuO plane become stronger than the interaction between the pancake vortices making up a flux line and there is believed to be an additional 2D-3D phase transition in the BSCCO phase diagram.

There is still uncertainty surrounding many aspects of the behaviour of high-T_c superconductors and much remains to be done to determine the exact nature of the phase diagram(s) for the different materials and the origins of the broadening of the superconducting transition in a magnetic field.

Chapter 3

The Two-dimensional Electron Gas

3.1. Introduction

Using a high-mobility two-dimensional electron gas (2DEG), it is possible to fabricate Hall probes which can measure magnetic field with high spatial resolution and great sensitivity. Such probes are ideal for measuring the small magnetic fields associated with flux vortices which may be detected close to the surface of a superconductor. In this chapter, we see how a 2DEG forms at the interface in a GaAs/$Al_xGa_{1-x}As$ heterostructure and what its properties are in both a uniform magnetic field and the highly inhomogeneous magnetic field found close to a superconducting surface. The reasons for the superiority of the 2DEG as a Hall probe are discussed at the end of the chapter.

3.2. The GaAs/$Al_xGa_{1-x}As$ Heterojunction

GaAs and $Al_xGa_{1-x}As$ with $x \leq 0.3$ have almost identical lattice constants and coefficients of thermal expansion, making it possible to join together the two different crystals to form a semiconductor heterojunction. The structure is grown by molecular beam epitaxy which builds up the crystal layer by layer, allowing precise control of composition at the atomic level. The two materials have different band gaps; the band gap of GaAs is 1.4eV while that of $Al_{0.3}Ga_{0.7}As$ is 1.7eV. The difference is largely made up by an increase in the $Al_{0.3}Ga_{0.7}As$ conduction band energy. This band mismatch is exploited by carefully tailoring the structure of the heterojunction, giving

rise to a quantum well in which conduction electrons are confined. When the two different materials are brought together, the alignment of the two sets of conduction and valence bands is determined by the exact nature of the charge distribution and associated electric fields across the heterostructure, subject to the requirement that the chemical potential be equal across the heterojunction when it is in equilibrium.

Electrical conduction is made possible in semiconductors by the presence of electrons in the conduction band (or holes in the valence band). In intrinsic semiconductors, carriers are generated by thermal excitation across the band gap with the result that at low temperatures carrier concentration is low and conductivity very poor. Conduction may be improved by the addition of shallow donors which provide electrons which are more readily excited to the conduction band. To provide conduction electrons in the GaAs/$Al_{0.3}Ga_{0.7}As$ heterostructure, silicon donors are added during growth to a region of $Al_{0.3}Ga_{0.7}As$ slightly removed from the actual interface, as may be seen in the sketch in Figure 3.1. There is an undoped spacer layer separating the dopant atoms in a thick doped alloy layer from the interface. Once in the conduction band, the mobile electrons drop into the lowest available energy states which are in the GaAs region, separated from the fixed donor impurities. The positively charged donor ions and free electrons establish a space charge region, the electrostatic potential of which is superimposed on the band diagram causing band bending. The barrier height is determined not only by the conduction band offset but also by the space charge potential which reflects the donor concentration. The band offset is ~0.3eV, and moderate doping can contribute a barrier height of the same order. Another contribution to the band structure is made by surface states that act as deep acceptors and trap electrons. The electric field of the charges at the surface repels conduction electrons, adding a downhill slope to the conduction band. The resulting band structure is sketched in Figure 3.1 below the physical structure.

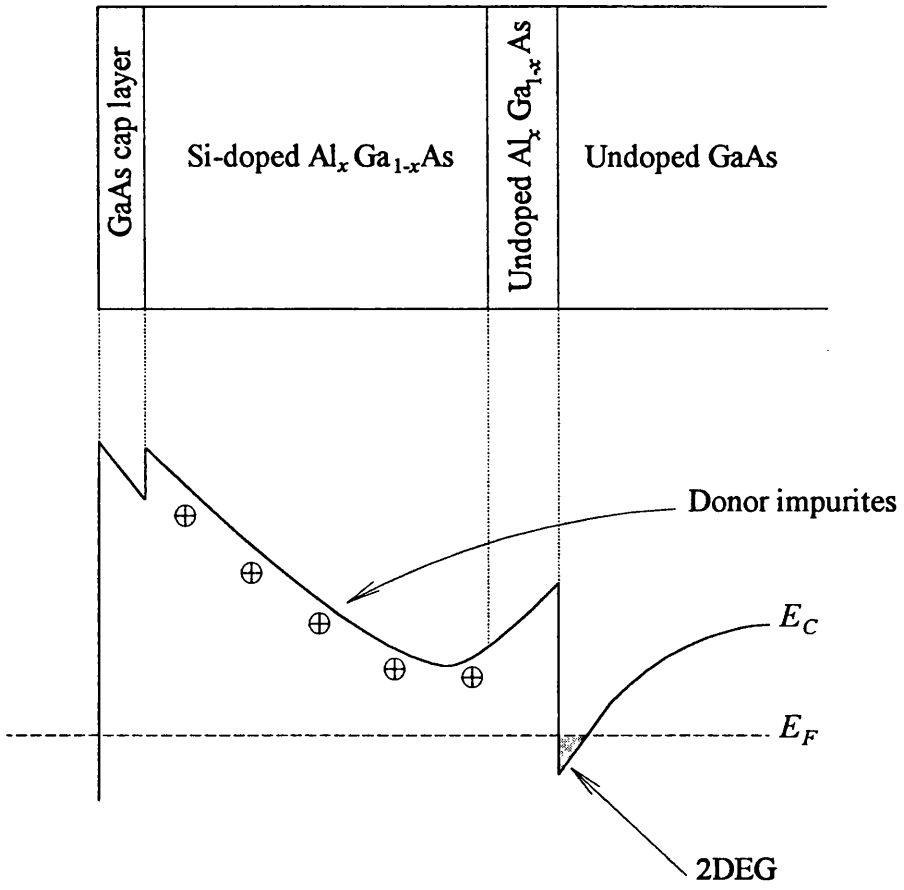

Figure 3.1. The layered structure of a GaAs/$Al_xGa_{1-x}As$ heterostructure (above). The corresponding conduction band structure showing the location of the positive donors and 2DEG (below).

3.3. The Two-dimensional Electron Gas

The conduction electrons in the GaAs conduction band are pulled up to the interface by the positively charged donor ions remaining in the $Al_xGa_{1-x}As$. The electrons are confined to a very narrow potential well, nearly triangular in shape. The width of the well is much less than the electron mean free path and consequently the electron transport is two dimensional in nature.

Consider an electron in the quantum well. In the direction perpendicular to the interface it is bound, in the plane parallel to the interface it can move freely. The

confinement of the electron changes the energy spectrum for motion in the perpendicular direction into a series of discrete levels. The electron states are found by solving Schrödinger's equation for electrons in the confining potential $V(z)$:

$$\left\{-\frac{\hbar^2}{2m^*}\frac{d^2}{dz^2}+V(z)\right\}\psi(z)=E\psi(z) \qquad (3.1)$$

where the effective mass m^* is as for the bulk material and the z-direction is perpendicular to the interface. The solution for a triangular well is given in Reference 31, but for our purposes it is sufficient to know that qualitatively there is a discrete set of energy levels E_0, E_1, ... referred to as subbands. The number and separation of subbands depends on the depth and width of $V(z)$. In our structures the electron concentration is low enough for only the first subband to be occupied which makes treatment of the system much simpler. If another subband is occupied, there is another set of electrons with a different mobility. The wavefunction in the first subband peaks about 50Å away from the interface.

In the x-y plane parallel to the interface, we expect the electronic structure of the semiconductor to be unchanged, the same as it is in the bulk material. The parallel momentum component is not quantized and, considering the free electron model in two dimensions, the Fermi surface is a disc in k-space of radius $k_F=\sqrt{2\pi n_{2d}}$ where n_{2d} is the two-dimensional electron concentration. The density of states is constant within each subband, not depending on k as is the case in three dimensions. The total density of states is step-like, increasing only as the next subband is entered. So the electron momentum is quantized in the z-direction, but continuous in the x- and y-directions, with the total electronic energy given by $E_T=E_{\parallel}+E_{\perp}+E_C$ where $E_{\parallel}=\frac{\hbar^2k_{\parallel}^2}{2m^*}$, $E_{\perp}$ is the subband energy and E_C is the energy of the conduction band.

The electron distribution near the interface is a very thin or quasi-two dimensional sheet of electron gas. It is not two dimensional in a strict geometrical sense since the wavefunctions have a finite spatial extent in the third dimension.

However it is effectively two-dimensional at low temperature as the thickness is very much less than the mean free path of the electrons. Looking at it from a quantum mechanical point of view, the carriers are confined to a well of width $\leq \lambda_F$ the Fermi wavelength, which is ~7nm in our structures.

3.4. Electron Mobility

The exceptionally high mobility of electrons in the heterostructure is a result of the great reduction in scattering at low temperatures. At room temperature, phonon scattering dominates and the electron mobilities in undoped bulk GaAs and the heterostructure are similar. As temperature falls to 77K, scattering from phonons decreases and both mobilities increase to a maximum of $\sim 2\times10^5 cm^2V^{-1}s^{-1}$. Below 77K the mobility in bulk GaAs falls as electrons become bound to impurities while in some heterostructures it can continue to increase to as much as $5\times10^6 cm^2V^{-1}s^{-1}$ at 1K.

At low temperatures, scattering by charged impurities and other defects generally determines mobility. Since lattice vibrations are suppressed, impurities are a major source of electron collisions. Donor impurities must be present to supply the carriers, but modulation doping is used to spatially separate the donors from the 2D electrons. By placing an undoped spacer layer of $Al_xGa_{1-x}As$ between the donors and the GaAs, the donor impurities are some distance away from the carriers and the resulting reduction in Coulomb scattering by the charged impurities improves mobility.

Two other sources of electron scattering, interface roughness and alloy scattering, are also reduced in the heterostructure. Scattering due to irregularities and imperfections at the heterostructure interface is small because epitaxial growth provides a very smooth surface and in addition the amplitude of the electron wavefunction at the actual interface is small so the electron motion is less sensitive to properties of the interface. The random placing of different atoms on lattice sites in an

alloy causes alloy scattering. This is weak in the heterostructure because the electrons penetrate very little into the alloyed $Al_xGa_{1-x}As$ region.

3.5. Electron Concentration

The electron concentration does not change much with temperature but it can be influenced in certain ways. One method is illumination of the heterostructure with infra-red radiation, exciting electrons from deep donor-related traps in the $Al_xGa_{1-x}As$ into the conduction band. From the conduction band, the electrons drop into the quantum well. The resulting increase in electron concentration is extremely long-lived at low temperatures, thus the effect is referred to as persistent photoconductivity (PPC). The deep traps are DX centres which undergo a large lattice relaxation on changing their charge state and so the probability of the electrons being recaptured is very small at low temperatures. The PPC effect is very useful for reversing any depletion of carriers in the 2DEG.

A metal gate deposited on top of the heterostructure can also be used to alter the electron concentration. The gate makes a Schottky contact to the semiconductor and current will not flow to the 2DEG if a modest bias voltage is applied. If the gate is reverse biased (i.e. gate becomes negative), electrons are pushed out of the 2DEG, causing n_{2d} to decrease. Conversely, a positive bias increases electron concentration. To achieve a stable electron concentration, the gate must be contacted and held at a fixed potential relative to the 2DEG to prevent for example a build up of static charge from changing n_{2d} in an unpredictable way.

3.6. The 2DEG in a Uniform Magnetic Field

In a conducting system, the charge carriers interact with an applied magnetic flux density **B** through the Lorentz force $\mathbf{F}_L = -q\mathbf{v} \times \mathbf{B}$ where q is their charge and **v** their velocity. If the magnetic field is perpendicular to the velocity, a charge carrier will

move in a circle at the cyclotron frequency $\omega_c = qB/m^*$ provided there is no scattering. In a real system, the charge carriers are scattered with a characteristic scattering time τ. There are two magnetic field regimes to consider : a low field regime where $\omega_c\tau << 1$ and the electron travels along a small fraction of an orbit before being scattered, and a high field regime where $\omega_c\tau >> 1$ and the electron undergoes many orbits before being scattered.

Typically magnetic fields up to 10mT were employed in the experiments described in this thesis. The 2D electron systems have scattering times of the order of 10^{-12}s, placing them firmly in the low field limit and simplifying considerably the magnetotransport. The free electron model is adequate to describe the classical Hall effect. The observed magnetoresistance only requires consideration of weak localization. The strong magnetic fields which place the system in the high field regime give rise to the quantum Hall effect and Shubnikov-de Haas oscillations in the magnetoresistance. These are beyond the scope of this thesis and we shall only consider what happens in the small fields encountered in this work.

3.6.1. The Hall Effect

In a degenerately doped semiconductor, the semiclassical free electron model of charge transport gives an adequate description of the Hall effect. The main simplifying assumptions are that the charge carriers move due to the applied electric and magnetic fields only, and that they all move with a uniform drift velocity. The thermal motion of the carriers and the details of scattering are neglected. The energy dissipation due to scattering is taken into account by the smooth friction that gives the drift velocity. The Hall effect is derived below for the conventional three-dimensional geometry, from which the two-dimensional case follows in a straightforward way. Detailed treatments of the Hall effect may be found in References 32 and 33.

Consider the flat conducting plate in Figure 3.2. The plate is long, that is its

length l is much greater than the width w, so that the influence of the current-supplying contacts may be ignored. To begin with, suppose that an external electric field $\mathbf{E}_e = (E_x, 0, 0)$ has been applied, but no magnetic field. From Ohm's law, the current density $\mathbf{j}$ is

$$\mathbf{j} = \sigma \mathbf{E}_e \tag{3.2}$$

where the conductivity $\sigma = nq\mu$ and n is the carrier density. If the carriers are electrons, they will move in the negative x-direction with a drift velocity $\mathbf{v}_d = -\mu \mathbf{E}_e$.

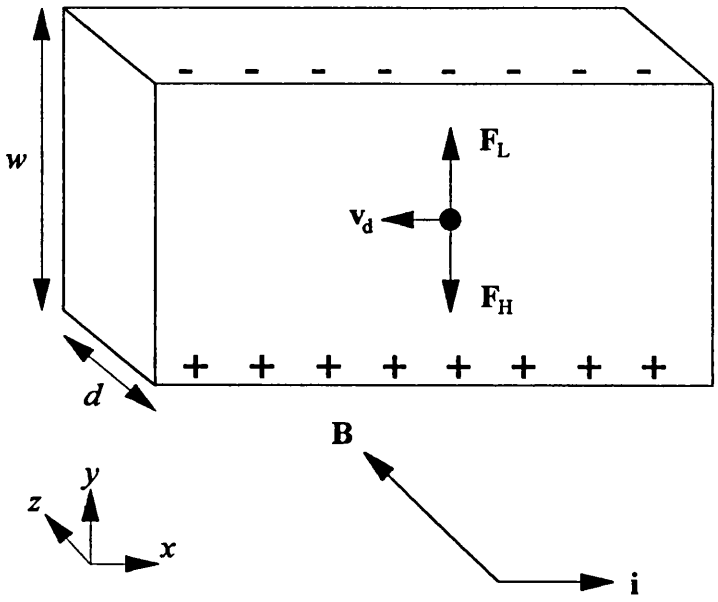

Figure 3.2. The Hall effect in a material containing negative charge carriers.

On applying a perpendicular magnetic field $\mathbf{B} = (0, 0, B_z)$, the Lorentz force acting on the charge carriers is given by

$$\mathbf{F}_L = q\mathbf{v}_d \times \mathbf{B}. \tag{3.3}$$

The Lorentz force pushes the carriers in the y-direction, causing an accumulation of charge at the upper edge of the strip and a decrease at the lower edge. The charge imbalance generates a transverse electric field $\mathbf{E}_H$ across the strip called the Hall field. An equilibrium is rapidly reached when the force caused by the Hall field balances the

Lorentz force :

$$q\mathbf{v}_d \times \mathbf{B} + q\mathbf{E}_H = 0 \tag{3.4}$$

which yields the Hall field :

$$\begin{aligned} \mathbf{E}_H &= -\mathbf{v}_d \times \mathbf{B} \\ &= \mu \mathbf{E}_e \times \mathbf{B} . \end{aligned} \tag{3.5}$$

At equilibrium the charge carriers again move parallel to the x-axis.

The Hall electric field causes a transverse voltage across the strip which can be measured between two points on opposite edges of the strip that lie on an equipotential when $\mathbf{B} = 0$. The Hall voltage is $V_H = wE_H$ and combining this with Equations (3.2) and (3.5) gives

$$V_H = R_H \frac{iB}{t} \tag{3.6}$$

where t is the thickness of the strip and the total current $i = jwt$. $R_H = 1/qn$ is called the Hall coefficient and has units $\Omega \mathrm{m T}^{-1}$.

In two dimensions, the derivation of the Hall voltage is carried out in the same way as above. However current density j is now a two-dimensional quantity and the total current is given by $i = jw$. Thus the Hall voltage is

$$V_H = R_H iB \tag{3.7}$$

where $R_H = 1/qn_{2d}$ and has units $\Omega \mathrm{T}^{-1}$. The reduction in dimensions is accounted for by the natural replacement of nt by n_{2d}.

3.6.2. Magnetoresistance

Magnetoresistance is defined as

$$\frac{\Delta R}{R} = \frac{R(B) - R(0)}{R(0)}. \tag{3.8}$$

The free electron model predicts zero magnetoresistance because the electron trajectories in the conductor are unchanged by the presence or absence of a transverse magnetic field, ignoring the effects of contacts. In real systems, there is usually a positive magnetoresistance and in semiconductors $\frac{\Delta R}{R} \propto B^2$ at small fields, as was observed in the 2DEG system at 77K.

However in high resistance systems at low temperatures, it is found that $\frac{\Delta R}{R} < 0$. This negative magnetoresistance is a quantum interference correction to the classical conductance. To see how it arises, consider a semiclassical picture of an electron propagating from point A to point B. The probability W of getting from A to B is the square of the sum of the quantum mechanical amplitudes over all possible paths :

$$\begin{aligned} W &= \left| A_I + A_{II} + \ldots \right|^2 \\ &= \left| A_I \right|^2 + \left| A_{II} \right|^2 + A_I A_{II}^* + A_I^* A_{II} + \ldots \end{aligned} \tag{3.9}$$

Contributions from paths of different lengths will in general have random phases so the cross-terms cancel giving the same result as classical diffusion.

Consider now a self-intersecting trajectory where an electron returns to its starting point. If the electron scatters elastically from an impurity, its phase changes by a fixed amount. Elastic scattering just changes the direction of the electron momentum, allowing the electron to diffuse back to its starting point with coherent phase. Each closed path can be traversed in two different directions, giving two paths of the same length. An electron travelling in the opposite direction will have the same phase shift by time-reversal symmetry and so the two quantum mechanical amplitudes remain coherent and interfere constructively. There is thus an increased probability of returning to the same point, in fact $W_{QM} = 2W_{Classical}$ which decreases the diffusion

constant and diminishes the conductivity.

In contrast to elastic scattering, inelastic scattering randomizes the electron phase and if inelastic scattering dominates the system, the classical result is regained : $W_{QM} = W_{Classical}$. Thus the first condition required to observe weak localization is that the inelastic scattering time $\tau_i >> \tau_e$ the elastic scattering time, so that elastic scattering dominates. A second condition, that the electron mean free path $l^* >> \lambda_F$ the Fermi wavelength, is necessary so that the electron trajectories are well defined and distinct. These conditions are satisfied in a system with weak disorder at low temperatures.

In two dimensions, the weak localization contribution to the total conductivity $\sigma_{Total} = \sigma_{Classical} + \delta\sigma$ is $\delta\sigma \approx -\frac{e^2}{\hbar}\ln(\tau_i/\tau_e)$. A magnetic field influences the weak localization correction through the Aharonov-Bohm effect. An electron traversing a closed path of area A in a perpendicular magnetic flux density B_a, gains an extra phase shift $\exp(\pm B_a A/\Phi_0)$ with the sign depending on the direction of travel. As B_a increases, the phase difference becomes larger and the cross terms in Equation (3.9) cancel with the result that $\sigma_{Total} \to \sigma_{Classical}$. A full calculation of the magnetoresistance for a weakly disordered 2D system[34] gives the result

$$\sigma(B,T) - \sigma(0,T) = \alpha\frac{e^2}{2\pi^2\hbar}\left\{\psi(a_i + \tfrac{1}{2}) - \psi(a_e + \tfrac{1}{2}) + \ln\left(\frac{\tau_i}{\tau_e}\right)\right\} \qquad (3.10)$$

where α is a constant of order 1 and ψ is the digamma function. The terms $a_{i,e} = \frac{\hbar}{4eBD\tau_{i,e}}$ with the electron diffusion constant $D = \frac{1}{2}l^{*2}/\tau_e$ at low temperatures. For small applied magnetic fields $B << B_i = \frac{\hbar}{4eD\tau_i}$, that is $a_i >> 1$, Equation (3.10) simplifies to

$$\sigma(B,T) - \sigma(0,T) = \tfrac{1}{24}\alpha\frac{e^2}{2\pi^2\hbar}\left(\frac{B}{B_i}\right)^2. \qquad (3.11)$$

3.7. The 2DEG in a Non-uniform Magnetic Field

When the 2DEG is placed in a magnetic field which varies on a length scale similar to the electronic mean free path, it is reasonable to expect that the magnetotransport will be different to the uniform field case. Such an inhomogeneous magnetic field can be provided by the flux vortices in a type II superconductor.

A flux vortex has a characteristic magnetic radius approximately equal to the penetration depth, which is ~0.1μm. The separation between vortices depends on the applied flux density B and is $a \approx \sqrt{\Phi_0/B}$. For moderate applied fields from 0.5mT to 10mT, $a \approx 2\mu m$ to $0.5\mu m$. The inhomogeneous field decays rapidly outside the superconductor, but if the 2DEG is sufficiently close, the field inhomogeneity is largely preserved. In the next chapter, the distributions of magnetic flux at the superconducting surface and at the 2DEG are calculated for some relevant situations.

3.7.1. The Hall Effect in a Non-uniform Magnetic Field

The Hall effect due to the magnetic field of an array of flux vortices has been studied in References 35 and 36. The Hall voltage at a constant magnetic field has been measured above the critical temperature of the superconductor, that is when the flux distribution is uniform. By cooling a type II superconducting film through its critical temperature, a perpendicular magnetic field is broken up into an array of vortices which has the same average flux density as the uniform magnetic field above T_c. This field-cooling technique gives an equilibrium distribution of roughly uniformly spaced flux vortices, but not a flux line lattice because the films have many pinning centres. There is no expulsion of flux by the Meissner effect or vortex density gradient caused by pinning. It was found[35] that there is no difference between the Hall voltage of a uniform field or of the inhomogenous field of an array of vortices, unless the 2DEG has a very low electron concentration less than $\sim 2 \times 10^{15} m^{-2}$.

To understand this qualitatively, consider the flux vortices as uniform cylinders

of flux with radius λ and assume that both the vortex spacing and electron mean free path are large compared to λ. Thus the electron is affected by the magnetic field along only a small part of its path. As an electron passes through a vortex, it is deflected by the Lorentz force for a short period. The deflection after passage through several vortices is cumulative and it was found[35] that the average force exerted on the electron is $F \approx ev_F B$, the same as the Lorentz force in a uniform magnetic field, giving the usual result for the Hall voltage. This simple picture assumes that the Fermi length of the electrons λ_F is less than or comparable to the vortex diameter, an assumption that is no longer valid at low electron concentrations because $\lambda_F = \sqrt{2\pi/n_{2d}}$. As the wavelength of the electron wavefunction becomes greater than λ, the asymmetrical scattering of the electron by the Lorentz force becomes less efficient because the electron is 'spread out' over an area greater than that containing the magnetic field. Scattering by the vector potential outside the vortex, the Aharonov-Bohm effect, becomes dominant. There is interference between electrons travelling on paths to the left and right of the vortex, but the paths enclose a total amount of flux Φ_0 so the incident electron wave is not deflected. The result is a quenching of the Hall voltage below the value expected for a uniform field. As the applied flux density increases, the vortex separation decreases and the magnetic field becomes more uniform. For all electron concentrations, the full Hall voltage is obtained for applied flux densities above ~15mT.

3.7.2. Magnetoresistance in a Non-uniform Magnetic Field

The characteristic length scale for weak localization is the distance over which the electron maintains phase coherence, the inelastic scattering length l_i which can be many microns at low temperatures. The weak localization correction at a given point is sensitive to the magnetic field within an area of order l_i^2, so if the magnetic field is non-uniform or modulated on this length scale, then we expect Equation (3.10) to be invalid. The conductivity $\sigma(\mathbf{r})$ is now non-local in the sense that it does not depend on

the magnetic field at **r** but on the magnetic field within the area $\sim l_i^2$.

At low applied magnetic fields $B << B_i = \frac{\hbar}{4eD\tau_i}$ the characteristic inelastic field, the vortex separation is much greater than l_i and the vortices act independently. Each vortex makes an identical contribution to the magnetoresistance which increases linearly with concentration of vortices. As the magnetic field increases further, the vortices start to overlap and an intermediate situation is realized where the magnetoresistance approaches the uniform field results.

Rammer and Shelankov[37] investigated weak localization in a distribution of flux cylinders of radius λ containing a uniform magnetic flux density B_0. In the 'non-local' limit where $l_i >> \lambda$ and for isolated vortices, they found that

$$\sigma(B,T)-\sigma(0,T) \approx \frac{e^2}{2\pi^2\hbar}\frac{1}{\ln(B_0/B_i)}\frac{|B|}{B_i}. \qquad (3.12)$$

Experiments have found that the magnetoconductivity is approximately linear in B at low fields[38, 39] but the slope of the experimental data is not predicted correctly by Equation (3.12). However the experiments do not access the 'non-local' limit and a numerical solution of the quantum diffusion equation using more realistic magnetic field distributions gives good results[40].

3.8. The 2DEG Hall Probe as a Magnetic Sensor

The magnetic field emerging from the surface of a superconductor is modulated on a microscopic scale, and once in free space, the inhomogeneities decay very rapidly. To measure this magnetic field is not easy, but Hall probes fabricated from a 2DEG are ideally suited to the task. Not only are 2DEG Hall probes particularly sensitive, but the 2DEG can also be photolithographically patterned to sub-micron dimensions, giving excellent lateral resolution. The 2DEG is also effectively planar and forms at a heterojunction very close to the semiconductor's surface, overcoming the problem of

the rapid decay of the magnetic field outside the superconductor. The following sections show in greater detail why the 2DEG makes such excellent devices.

Semiconductors are often used as Hall sensors for magnetic field measurements[33]. When deciding which material to use, it is not the maximum Hall voltage obtainable for a given magnetic field that is important, but the smallest magnetic field that can be measured. The minimum detectable field is set by the signal-to-noise ratio of the probe, and this is the quantity of interest in the following sections. To simplify the qualitative treatment of Hall probe sensitivity[41], the following assumptions are made :

1. Electrical properties are independent of size.
2. The thermal noise of the probe resistance is the only noise source.
3. Power dissipation per unit area of the probe in contact with the substrate is constant.

The first assumption avoids any complications that arise when the probe dimensions shrink to the same length scale as the electron mean free path. The second assumption allows noise from the measurement system or other sources to be ignored. The thermal noise should just be taken as a lower limit on the noise of the entire measurement system. The thermal voltage noise is $V_N = 2\sqrt{k_B T R \Delta f}$ where R is the probe resistance and Δf is the measurement bandwidth. In what follows, we take $V_N \propto \sqrt{R}$ or $V_N \propto \sqrt{\rho}$ as appropriate. The last assumption is necessary because for a given material in a given applied magnetic field, the signal V_H is maximized when the probe current is made as large as possible. There must be a limit to the current passing through the Hall probe, and that limit is given by the power that the probe can dissipate without significant self-heating. The power dissipation condition states that

$$\frac{P}{A} = \frac{i^2 R}{wl} = \text{constant} \tag{3.13}$$

where P is the power dissipated in a Hall probe of area A.

3.8.1. Probe Material

To see how the signal-to-noise ratio depends on the choice of probe material, we consider a probe of fixed geometry and fixed power dissipation. The noise voltage depends only on the resistivity of the material : $V_N \propto \sqrt{\rho}$. The signal is $V_H = R_H iB$ where the Hall coefficient R_H is a property of the material and the current i through the probe is determined by the power dissipation condition. Taking into account the fixed geometry, it follows from Equation (3.13) that $i \propto \rho^{-1/2}$. Thus the signal-to-noise ratio is

$$\frac{V_H}{V_N} \propto \frac{R_H \rho^{-1/2}}{\rho^{1/2}} = \frac{R_H}{\rho}. \tag{3.14}$$

Material	R_H ($\Omega m T^{-1}$)	ρ (Ωm)	μ ($m^2 V^{-1} s^{-1}$)
2DEG at 4.3K	4 800	56	86
2DEG at 77K	4 800	370	13
Bulk GaAs[42]	8×10^{-3}	0.01	0.8
InSb[43]	3.5×10^{-4}	5×10^{-5}	7.0
InAs[41]	7.5×10^{-5}	3×10^{-5}	2.5
Bi[41]	1.0×10^{-6}	1.2×10^{-6}	0.83
Au[41]	7.0×10^{-11}	2.2×10^{-8}	3.2×10^{-3}

Table 3.1. Hall coefficient, resistivity and mobility of some materials used as Hall probes. Note that for the 2DEG, R_H and ρ are two-dimensional quantities with units ΩT^{-1} and Ω respectively.

The ratio R_H/ρ is a measure of the minimum detectable magnetic field for a particular material and may be regarded as a figure of merit. It is listed in Table 3.1 for the 2DEG and a range of commonly used materials. For a semiconductor the ratio R_H/ρ is equal to the mobility μ, so the desirability of a high mobility is clear. In practice other factors will also influence the choice of probe material, such as ease of fabrication and compatibility with the sample to be measured.

3.8.2. Spatial Resolution

To achieve high spatial resolution, the sensitive area of the Hall probe should be as small as possible. To see how the sensitivity of a two-dimensional Hall probe varies with its area, we introduce a scale factor k such that $l = kl_0$ and $w = kw_0$ where l and w are the length and width of the probe respectively. The thermal noise voltage V_N is unchanged as the linear dimensions are scaled because the resistance of the two-dimensional probe remains constant : $R = \rho\frac{l}{w} = R_0$. The signal $V_H = R_H iB$ scales in the same way as the current i under the assumption of constant power dissipation per unit area : $\frac{P}{A} = \frac{i^2R}{wl} = \frac{i_0^2R_0}{w_0l_0}$. Because $R = R_0$, it follows that $i = ki_0$. This is equivalent to the two-dimensional current density $j = \frac{i}{w} = \frac{ki_0}{kw_0} = j_0$ remaining constant as the dimensions are scaled. Thus the signal-to-noise ratio is

$$\frac{V_H}{V_N} \propto k \tag{3.15}$$

and as the Hall probe dimensions decrease $(k < 1)$, the minimum detectable field increases and the probe becomes less sensitive. (An identical result is found for a three-dimensional probe whether its thickness remains constant or scales with the area.)

There is an additional consideration when the probes are used to sense the quantized flux vortices found in the mixed state of a superconductor. A flux vortex is smaller than a practical Hall probe, and as we have seen above, a single flux quantum

threading a Hall probe produces the same signal as a uniform magnetic field $B = \Phi_0 / A$. If a single flux vortex remains in the Hall probe as its area is scaled, we find that $B = \frac{1}{k^2} B_0$ and the signal-to-noise ratio in Equation (3.15) becomes

$$\frac{V_H}{V_N} \propto \frac{1}{k}. \tag{3.16}$$

Now the sensitivity increases as the probe becomes smaller, until probe size approaches the dimensions of the vortex itself.

A Hall probe cannot be made arbitrarily small and care should be taken when probe dimensions are of the order of the electron mean free path in the material. For example, the Hall voltage of a bismuth probe is quenched when the probe thickness becomes less than 1μm[44]. Thickness is not a relevant parameter for a 2DEG, but when the probe width shrinks sufficiently for the conducting regions to become quasi-one-dimensional, quenching of the Hall voltage is observed[15].

3.8.3. Time resolution

The Hall effect has been found to be independent of frequency up to the microwave region[32]. Time resolution has not been stretched in the low frequency ac measurements carried out in this work, and it seems likely that the time response of a 2DEG probe will be limited by factors such as the device capacitance, instrumental bandwidths and time constants used to improve signal-to-noise.

Chapter 4

Superconductor/Semiconductor Hybrid Structures

4.1. Introduction

The flux vortices found in the mixed state of a type II superconductor produce an inhomogeneous magnetic field which decays rapidly outside the superconducting surface. If the 2DEG Hall probes are to achieve vortex resolution, the separation between superconductor and semiconductor must be as small as possible and this is the main consideration when designing the hybrid superconductor/semiconductor structure. The magnetic field distribution is calculated below for a hybrid structure of the type employed in the next chapter. The magnetic field is found at the superconducting surface and at a separation corresponding to that of the Hall probe. If the superconductor/Hall probe separation is not known, it can be estimated by measuring the magnetic field at the Hall probe for low applied fields while the superconductor remains in the Meissner state. Different superconducting films were investigated in this work, necessitating the design of two types of Hall bars which are described in a later section. The fabrication of the Hall bars and the assembly of the hybrid superconductor/semiconductor structure are also described. The chapter concludes with a description of the experimental apparatus and techniques used to examine the hybrid structures.

4.2. Magnetic Field Distribution

Using the Clem vortex model introduced in Chapter 2, the magnetic field

distribution can be calculated at the surface of a superconductor in the mixed state. To find the corresponding distribution at the Hall probe, we must first calculate how the inhomogeneous magnetic field decays outside the superconducting surface.

Consider a semi-infinite type II superconductor filling all space $z \leq 0$ with a magnetic field applied in the z-direction. At the superconducting surface in the x-y plane, the inhomogeneous magnetic flux density due to the flux line lattice is $\mathbf{B}(\mathbf{r}) = (0, 0, B_z(\mathbf{r}))$ where $\mathbf{r}$ is a position vector in the x-y plane. The flux line lattice is a periodic structure and the periodicity will be preserved in $\mathbf{B}(\mathbf{r}, z)$, the magnetic field above the superconducting surface, the z-component of which can be expanded in a Fourier series :

$$B_z(\mathbf{r}, z) = \sum_{\tau} B_z(\tau, z) \exp(i\tau \cdot \mathbf{r}). \tag{4.1}$$

$\mathbf{B}(\mathbf{r}, z)$ also has small x- and y-components which are of no interest because they are not detected by the Hall probes.

In free space outside the superconductor, the current density is zero and Maxwell's equations become $\nabla \cdot \mathbf{B} = 0$ and $\nabla \times \mathbf{B} = 0$. By a vector identity, $\nabla^2 \mathbf{B} = 0$ and substituting in $B_z(\mathbf{r}, z)$ gives

$$\sum_{\tau} \left\{ B_z(\tau, z).(i\tau_x)^2 + B_z(\tau, z).(i\tau_y)^2 + \frac{\partial^2 B_z(\tau, z)}{\partial z^2} \right\} \exp(i\tau \cdot \mathbf{r}) = 0. \tag{4.2}$$

Because $\exp(i\tau \cdot \mathbf{r})$ is not always equal to zero, it follows that

$$\frac{\partial^2 B_z(\tau, z)}{\partial z^2} = |\tau|^2 B_z(\tau, z). \tag{4.3}$$

Solving this differential equation subject to the boundary condition in the x-y plane yields $B_z(\tau, z) = B_z(\tau, 0) \exp(-|\tau| z)$ and the solution we require is

$$B_z(\mathbf{r}, z) = \sum_{\tau} B_z(\tau, 0) \exp(-|\tau| z) \exp(i\tau \cdot \mathbf{r}). \tag{4.4}$$

Thus the magnetic field inhomogeneity decays exponentially on the scale of the lowest spatial frequency with increasing height above the superconducting surface. As a rule of thumb, the magnetic field inhomogeneity extends over a distance of the same order as the period of the lowest spatial frequency, that is the spacing between flux vortices.

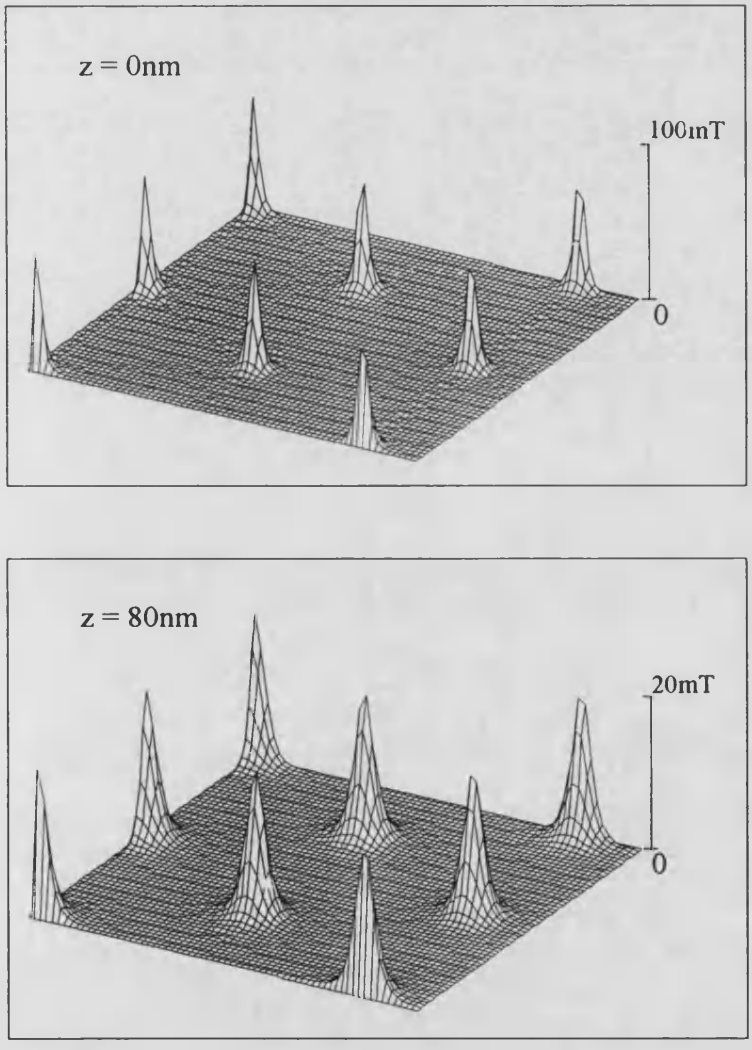

Figure 4.1. (a) The magnetic flux density at the surface of a Pb film (above) and 80nm away from the film (below). The applied flux density is 0.5mT and the vortex spacing is approximately 2μm.

The flux density of a flux line lattice is given by the Clem model in Equation (2.21) in the convenient form $B_z(\mathbf{r}) = B\sum_{\tau} F(\tau)\exp(i\tau\cdot\mathbf{r})$. To compute the flux density away from the surface just requires additional factors of the form $\exp(-|\tau|z)$. Using the superconducting parameters of the Pb films investigated in the next chapter, the Clem model was used to construct the surface plots in Figures 4.1 (a) and (b). These show the magnetic flux density at the surface of the Pb film and at the 2DEG 80nm away for two different applied magnetic fields. The flux vortices are well resolved at the 2DEG for moderate applied fields except very close to T_c.

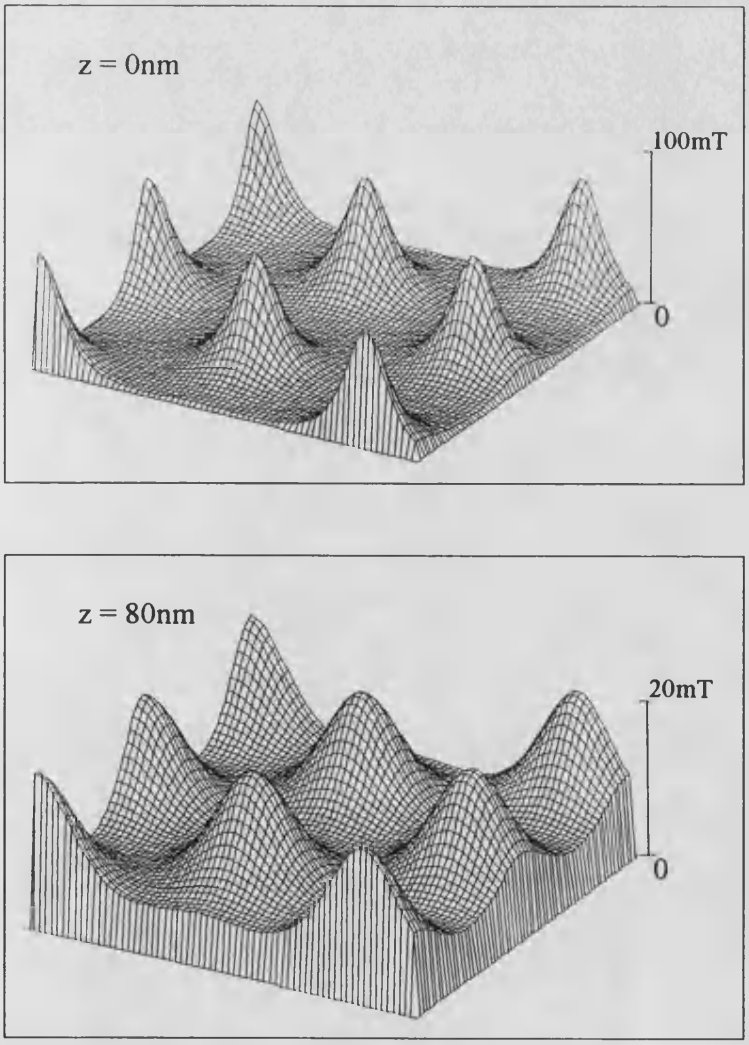

Figure 4.1. (b) The applied flux density is now 10mT and the vortex spacing has decreased to approximately 0.5μm.

4.3. Superconductor/Semiconductor Separation

When the superconducting film is in the Meissner state, it screens the Hall probe from the perpendicular magnetic field. The degree of screening will depend on the distance between the superconductor and the Hall probe. The greater the separation, the greater will be the fraction of the applied magnetic field measured by the Hall probe. Because the demagnetization factor for the strip in this geometry is very nearly 1, the Meissner state will only exist at very low applied magnetic fields. It will be more easily observed at the lowest temperatures because then the critical current will be higher and will screen the magnetic field more efficiently.

Consider a long superconducting strip in the x-y plane of width $2W$ and thickness d such that $2W >> d$. The strip is centred at the origin and runs along the y-axis. A uniform perpendicular magnetic field H_a applied along the z-axis induces supercurrents in the strip. If H_a is small enough, the strip will remain in the Meissner state with an ideal supercurrent density integrated over the thickness of the strip given by[28]

$$J(x) = \frac{2xH_a}{\sqrt{a^2 - x^2}}. \tag{4.5}$$

This ideal screening current flows either within two surface layers of thickness λ or is nearly constant across the film thickness if $d < \lambda$. The magnetic field intensity $H(z)$ at a distance z above the centre of the strip is a superposition of the applied field H_a and the field intensity produced by the screening current :

$$\begin{aligned} H(z) &= H_a - \int_{-W}^{W} \frac{x}{x^2 + z^2} J(x)dx \\ &= H_a \frac{z}{\sqrt{W^2 + z^2}} . \end{aligned} \tag{4.6}$$

The separation z_0 between the Hall probe and the centre of the strip was always small enough to satisfy the condition $z_0 << W$, so the magnetic field $H(z_0)$ at the

probe is well approximated by :

$$H(z_0) = H_a \frac{z_0}{W}. \qquad (4.7)$$

This relation is used to determine z_0 in later chapters.

4.4. Hall Probe Design

The superconducting film was either directly deposited onto the Hall probe or onto a separate substrate which was sandwiched together with the Hall probe. A different Hall probe structure was designed for each technique, the method used depending on the compatibility of the superconductor with the material of the detector. Three superconducting films have so far been investigated :

1. Pb films deposited by thermal evaporation.
2. Nb films deposited by sputtering.
3. $YBa_2Cu_3O_{7-\delta}$ films grown by molecular beam epitaxy.

The specific characteristics of these films are dealt with in later chapters, along with the measurement results. Here we are only interested in their compatibility with the $GaAs/Al_xGa_{1-x}As$ heterostructure. Pb is a soft metal and can be deposited by thermal evaporation directly onto the semiconductor without affecting the properties of either the 2DEG or the superconductor. The process of sputtering would deliver Nb atoms to the surface of the semiconductor with sufficient energy to damage the semiconductor, causing depletion of electrons from the 2DEG. Nb films were thus deposited onto a sapphire substrate. In the case of YBCO, a lattice-matched substrate is necessary for the growth of high quality films, and the films were grown on a MgO substrate.

The two different detector designs are shown in Figure 4.2. Both have similar central Hall bar structures, the main difference being the length of the current and voltage leads. Probe A was designed for the direct deposition of a superconducting film, with the short voltage leads intended to reduce the source resistance and the

associated thermal noise. There were a pair of Hall bars in each structure, one of which was covered by the superconductor while the other remained uncovered, providing an ungated control. Probe B was designed with very long current and voltage leads to extend out from under the superconductor substrate. The leads were defined by etching away the material in between to a depth of ~0.2μm and were made quite narrow to reduce the raised area of semiconductor in contact with the superconductor. There would then be less opportunity for superficial debris on either the semiconductor or the superconductor to interfere and spoil the desired close spacing.

The simple Hall bar structures were made with equal voltage and current lead widths providing a square intersection. With the benefit of hindsight, probe B was designed with a wider range of distances between the lead intersections, because the probe separation was found to be an interesting parameter to vary. Hall bars with line widths from 2μm to 10μm were fabricated.

4.5. Hall Probe Fabrication

The epitaxially grown GaAs/$Al_xGa_{1-x}As$ heterostructures were fabricated using standard semiconductor processing techniques. These are outlined briefly below; detailed procedures are listed in Appendix A. The first step is to make low-resistance ohmic contacts to the 2DEG. The contact pads are defined in ultraviolet-sensitive photoresist by optical lithography and then a gold-germanium eutectic is deposited by thermal evaporation. The photoresist is removed by a solvent, 'lifting-off' the unwanted Au-Ge film. The contact pads that remain are then annealed, the Au-Ge diffusing into the semiconductor to create a heavily doped n^+ region in contact with the 2DEG. The same lift-off technique is used to deposit a gold bonding layer on top of the alloy pads, providing a surface suitable for ultrasonic bonding of fine gold wires. Finally the Hall bar structure is lithographically patterned in photoresist which protects the Hall bar while unwanted material is etched away with an acidic/alkaline solution. It was

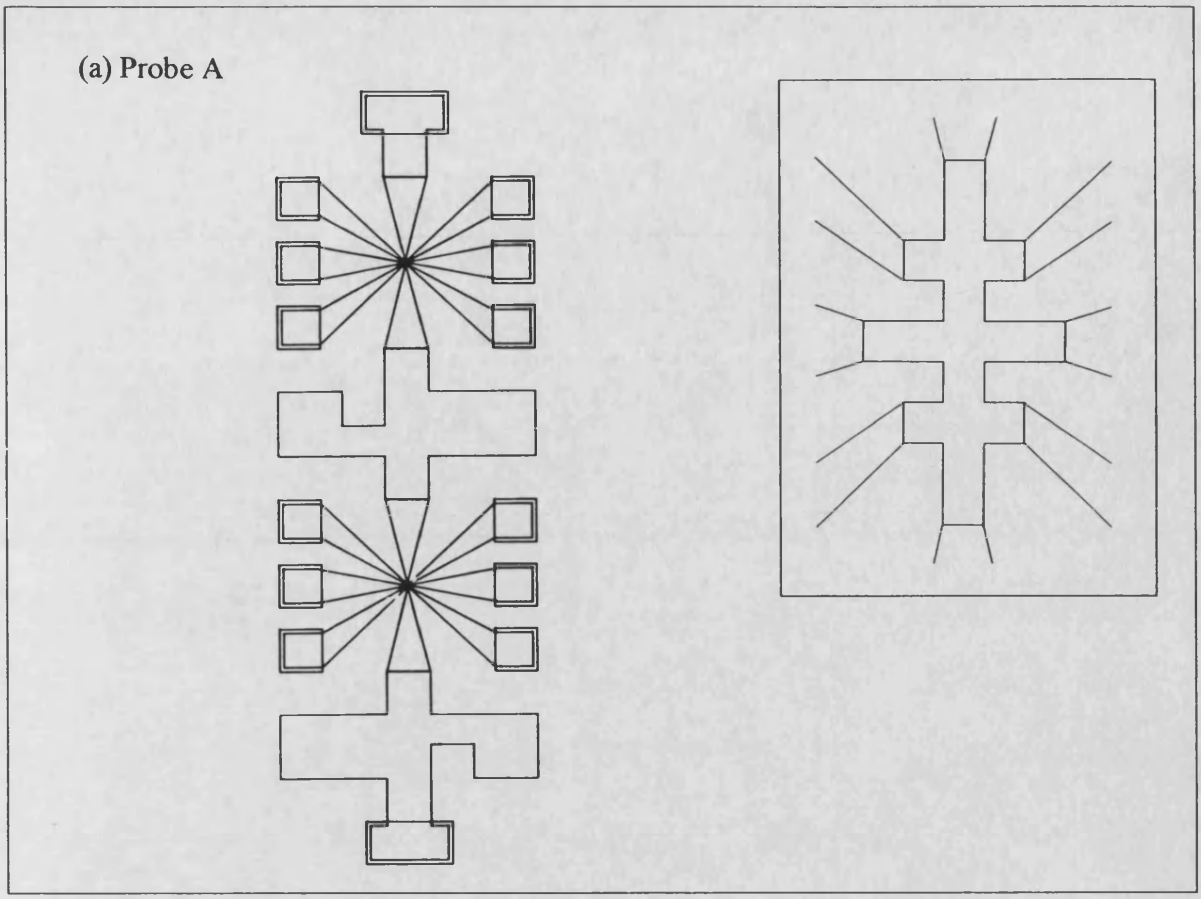

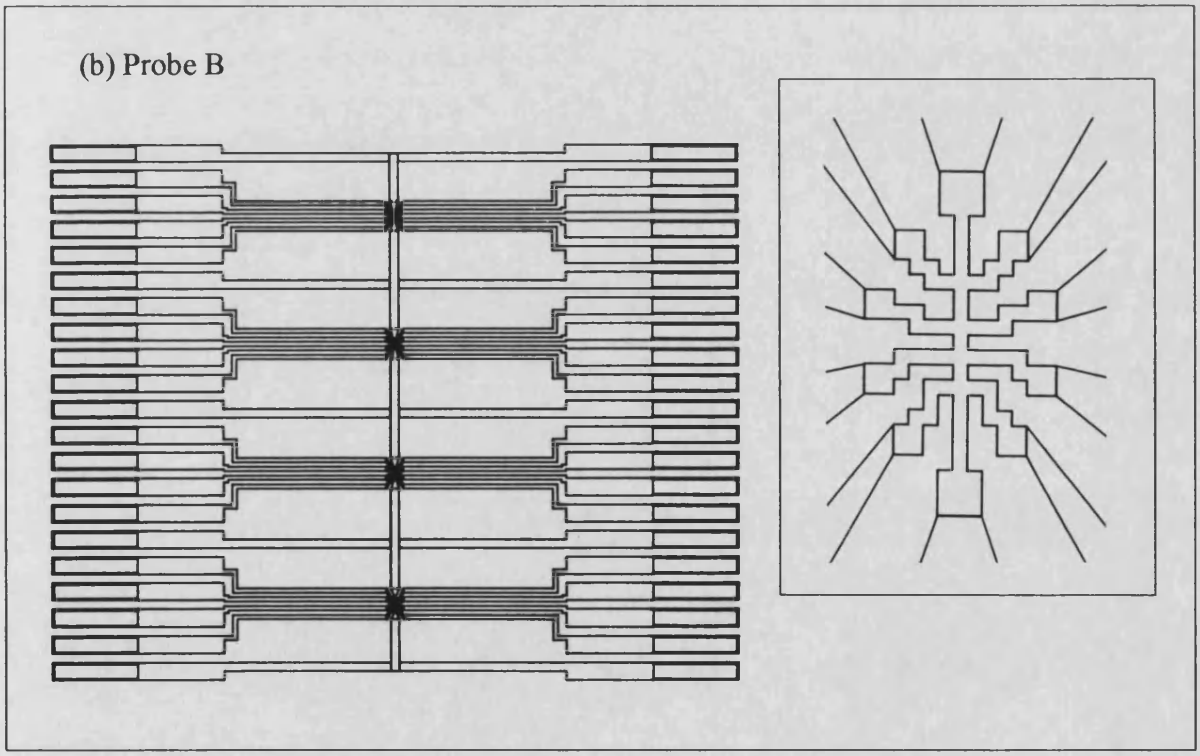

Figure 4.2. (a) Probe A : The Hall bar structure used with directly deposited films. (b) Probe B : The Hall bar structure used with films on separate substrates. The insets show the fine structure of the Hall probes. In both cases the narrowest lines are 2μm wide.

necessary to pay careful attention to clean room technique because the smallest Hall probe linewidth of 2μm is close to the limit for optical lithography and wet-chemical etching.

4.6. Assembly of the Hybrid Structure

The Pb films were deposited and patterned using another lift-off process. Because of the softness and poor adhesion of the Pb to the semiconductor, it was necessary to use a thicker layer of photoresist and to exercise care during the lift-off procedure.

Some trial and error was necessary before a satisfactory method was evolved to ensure close contact between the Hall bar and the superconducting films already on their own substrate. A suitable adhesive was found to be GE varnish diluted with a 1:1 toluene/ethanol mixture to a viscosity similar to that of water. The use of diluted Bostick has also been reported[45]. The diluted GE varnish formed a bond that was robust and durable, suffering no noticeable degradation after many thermal cycles.

The superconductor was attached to the Hall bar by the following procedure. A drop of diluted GE varnish was placed on top of the Hall bar structure. The substrate bearing the superconductor was mounted with the superconductor facing downwards on a micromanipulator and lowered into position. Sometimes it was necessary to apply a little acetone to thin the varnish which thickened as solvent evaporated. When the superconductor was satisfactorily aligned, sufficient pressure was applied to bring the substrate into close contact with the semiconductor, the separation being judged by the appearance of optical interference fringes between substrate and semiconductor. The superconducting films were deposited onto transparent or semi-transparent substrates and because they were patterned, it was possible to see through the substrate to the chip below. When the substrate was in close contact with the semiconductor, under a microscope it was possible to see red and green interference fringes, implying that the

separation between superconductor and semiconductor was of the order of a few quarter-wavelengths of visible light. In some cases it was possible to see the interference fringes in the deeper etched sections of semiconductor between the voltage leads while the voltage leads appeared black. Pressure was applied overnight while the glue dried. Finally, extra GE varnish was applied around the edges of the substrate to reinforce the bond.

4.7. Experimental Apparatus

The experiments were carried out in a conventional glass cryostat. A temperature range of 3-15K was accessible with liquid helium, suitable for working with low-temperature superconductors. The use of liquid nitrogen opened up a range from 65K upwards, appropriate for the high-T_c films. Intermediate temperatures were seldom required, but were accessible as the system warmed up after a helium fill.

The alumina chip carrier bearing the hybrid structure of Hall probe and superconducting film was glued onto a copper sample holder, illustrated in Figure 4.3. The stainless steel sample tube was filled with ~100mbar of helium exchange gas to provide a thermal link between the bath of cryogen and the sample. Temperature was measured by a calibrated carbon glass resistor that was inserted into a close-fitting hole in the copper holder near to the sample. The thermometer leads were varnished onto the interior of the sample holder to further improve thermal contact. The temperature was controlled using a Lakeshore DRC-91CA temperature controller and a 50Ω constantin wire heater, bifilar-wound to avoid adding an extra magnetic field when in operation. The sample temperature could be stabilised to better than ±2mK in the lower temperature range. Stability degraded to ±20mK in the upper temperature range due to reduced thermometer sensitivity and increased thermal mass of the system.

Small perpendicular magnetic fields were generated by a copper solenoid immersed in the bath. The 74mm-long solenoid consisted of 2917 turns with an inside

diameter of 31mm and an outside diameter of 40mm. The magnetic flux density is given by a standard short solenoid formula[46] : $B = k\mu_0 nI$ where the constant $k = 0.90 \pm 0.01$ takes into account the finite solenoid dimensions, n is the number of turns per metre and I is the solenoid current. The calibration was confirmed by agreement between n_{2d} measured using the solenoid and the value measured by the crystal growers. A copper solenoid has the advantage over a superconducting one that there can be no residual trapped flux when the solenoid current is reduced to zero. A disadvantage of copper was considerable joule heating in the solenoid when high currents were applied to provide larger magnetic fields. Fortunately such magnetic fields were seldom necessary because, as we have seen above, weak magnetic fields are sufficient to provide widely spaced vortices that can be individually resolved at the detector.

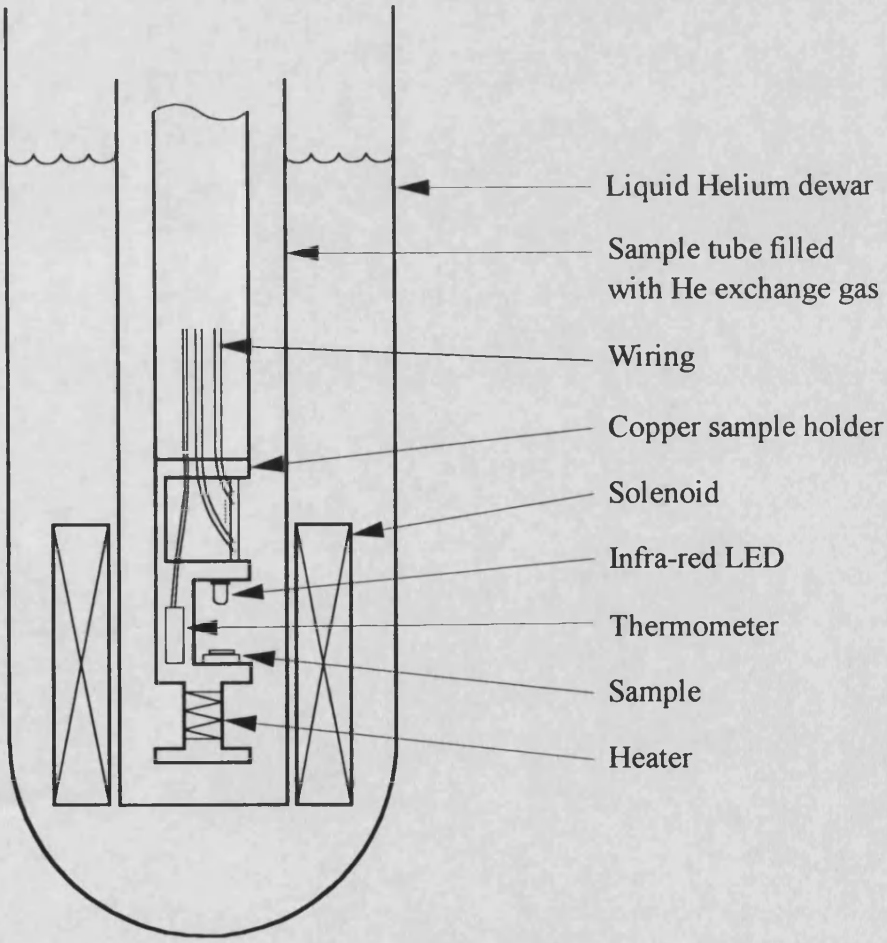

Figure 4.3. Sketch of the sample holder with a sample in place.

Electrical connections from the sample holder to the top of the cryostat were made with screened stainless steel wires to reduce the heat leak to the sample holder. The solder joints at the cold end of the sample tube were made with indium solder. Indium has a critical temperature below the range of interest (unlike lead-tin solder), and was used as a precaution against spurious results caused by a sudden change in contact resistance. An infra-red light-emitting diode provided illumination to improve the electrical properties of the 2DEG.

4.8. Measurement Circuits

The Hall bar served as a high resolution probe of the magnetic field close to the surface of the superconductor while the magnetic field, temperature or supercurrent were varied to change the state of the superconductor. The quantities measured at the 2DEG were the Hall voltage and on some occasions, the magnetoresistance. When a current was passed through the superconducting film, the resistance of the film was measured to confirm the value of T_c and to observe any flux flow voltages.

The transport properties of the Hall bar structure were measured using conventional ac lock-in techniques. The circuit used to measure the Hall voltage is shown in Figure 4.4(a). The signal generator passes a 31Hz ac current through the sample and provides a reference for the high-input-impedance lock-in amplifier. There was a small constant phase difference $< 10°$ between the reference and all the signal voltages from a particular sample. The signal generator is a voltage source so the 1MΩ resistor was placed in series with the Hall bar to maintain a constant current. The actual value of the current was monitored by measuring the voltage drop across the 1kΩ resistor. The sample was connected in the ac bridge circuit in Figure 4.4(b) to provide increased sensitivity for the magnetoresistance measurement. A second identical lock-in amplifier could be used to measure the Hall voltage and magnetoresistance simultaneously.

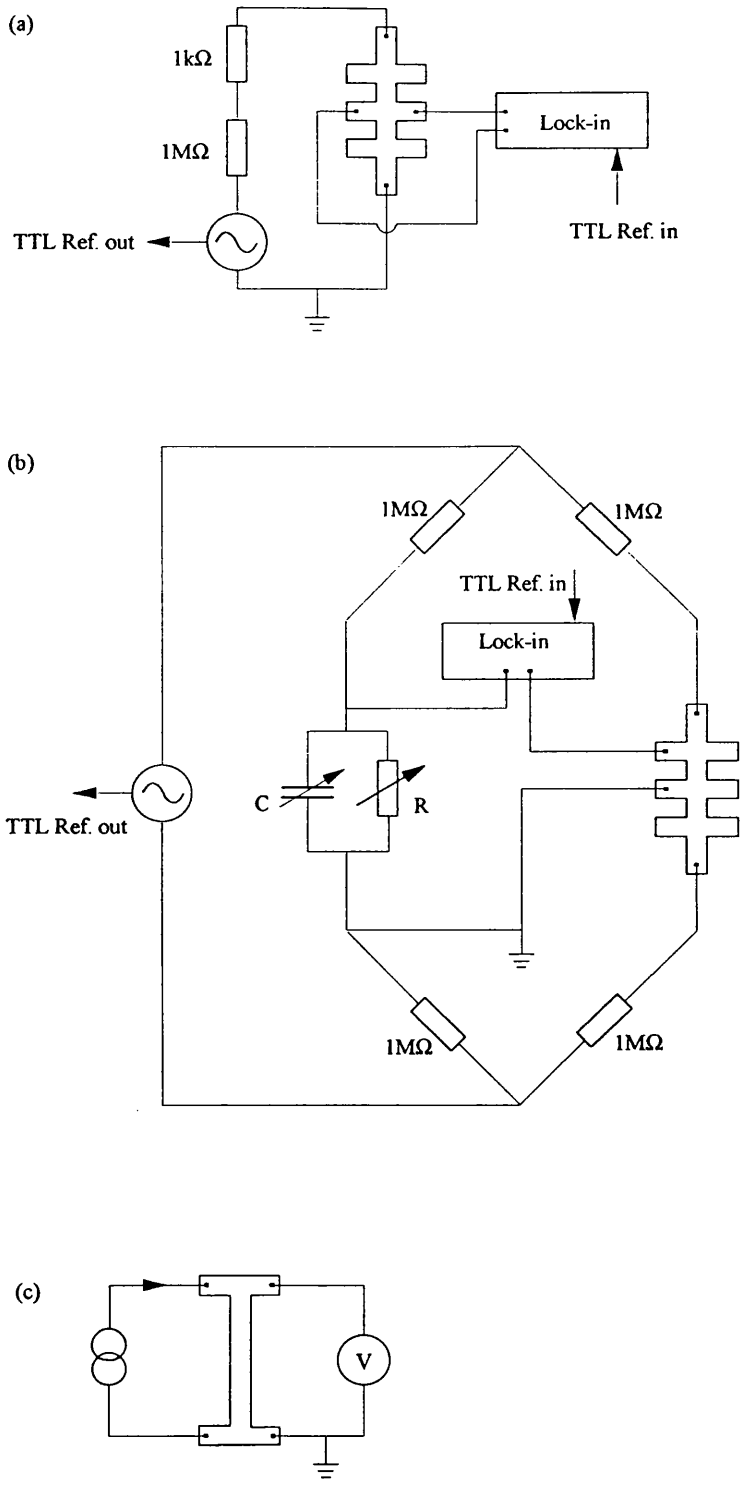

Figure 4.4. (a) The electrical circuit used for the measurement of Hall voltage. (b) The ac bridge circuit used to measure magnetoresistance. (c) The circuit used to measure the resistance of the superconducting film.

Throughout all the measurements, the superconductor was electrically grounded at the same point as the 2DEG. With the gate and 2DEG shorted together, there could be no potential difference between them and no gating effect to change the electron concentration in the 2DEG. At least one electrical contact was always made to the superconductor for this purpose. Four contacts were made for some experiments where a current was driven through the superconductor, permitting four-point resistance measurements. The simple circuit for this measurement is illustrated in Figure 4.4(c). One of the voltage contacts was shorted to the 2DEG because if a current lead was used, the voltage drop due to the lead and contact resistances was sufficient to cause a gating effect.

A common problem encountered with the Hall probes, particularly at low temperatures, was high resistance voltage or current leads caused by either bad ohmic contacts or by sections of the 2DEG being depleted of electrons. Whatever the cause, the problem could usually be cured by illuminating the sample with the infrared LED for a few seconds, exciting more electrons into the 2DEG by the persistent photoconductivity effect.

4.9. Semiconductor Characterization

The two quantities that characterize a 2DEG are its electron concentration and mobility. To use the 2DEG as a calibrated magnetic sensor, n_{2d} must be known, and together n_{2d} and μ set the signal-to-noise ratio of the Hall probe. Because n_{2d} can differ slightly each time the detector is cooled down from room temperature, the 2DEG was characterized at the beginning of every set of measurements. As long as the detector was kept cold, its properties remained stable.

The electron concentration and mobility of the 2DEG were found by measuring the Hall coefficient and resistance with the superconducting gate in its normal state. It was necessary to work above T_c so that the gate was 'transparent' to the applied

magnetic field and screening by the superconductor did not expose the 2DEG to an unknown magnetic field. $V_H(B)$ was usually measured from −10mT to +10mT and the gradient $\frac{\Delta V_H}{\Delta B}$ obtained from a least squares fit. It was then a simple matter to find n_{2d}, recalling from Chapter 3 that $V_H = R_H iB$ and $R_H = 1/en_{2d}$. The resistance R of a section of the Hall bar was measured and the resistivity determined from the Hall bar geometry : $\rho = \frac{1}{2}R$. The mobility was obtained from the relation $\sigma = n_{2d}e\mu$.

Both n_{2d} and μ are plotted in Figure 4.5 as functions of temperature below about 90K. Electron concentration is only weakly temperature dependent while the mobility changes considerably. Neither n_{2d} nor μ change significantly over the narrow temperature range used for the conventional low-temperature superconductors.

For an optimal signal-to-noise ratio, the current flowing through the Hall bar should be as large as possible. A longitudinal voltage was measured at the Hall bar and the applied current steadily increased until a deviation from Ohm's law was seen. This indicates excessive joule heating in the 2DEG, and a slightly smaller current was chosen for the operating current.

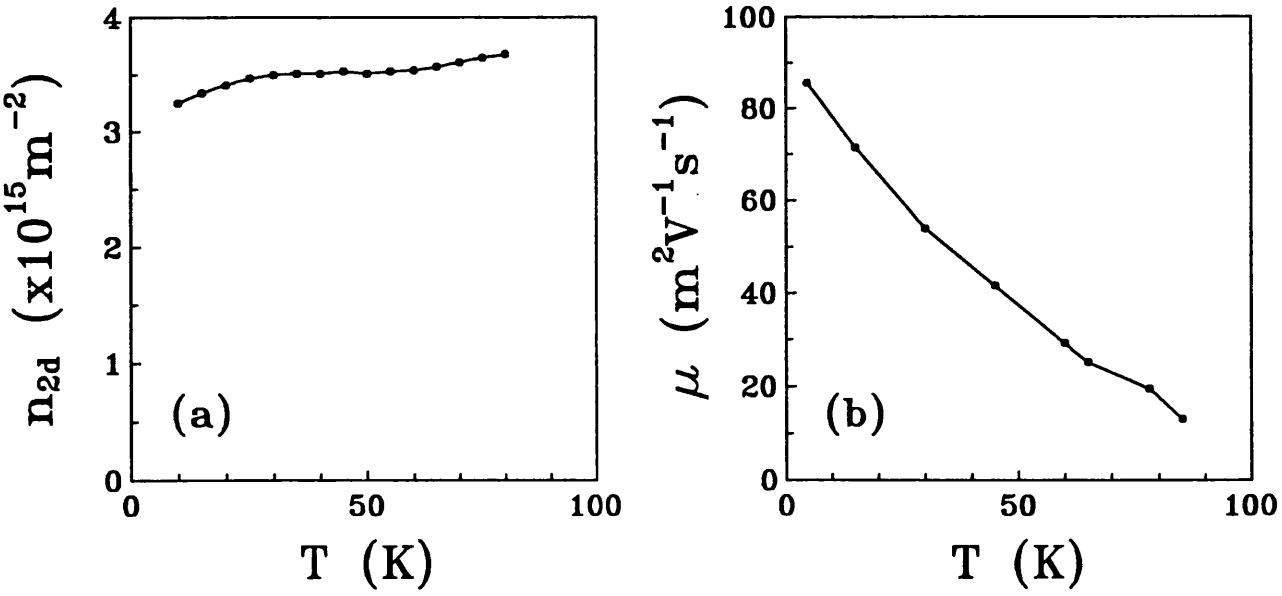

Figure 4.5. (a) The electron concentration n_{2d} of a 2DEG as a function of temperature. (b) The electron mobility μ of a 2DEG as a function of temperature.

Chapter 5

Lead Films

5.1. Introduction

Pb was chosen for the first experiments because it has one of the largest peak vortex fields of all known superconductors and it could also be deposited directly onto the Hall probe surface. These properties ensure that the magnetic field at the 2DEG will have the largest possible amplitude modulation.

Two series of experiments were carried out using two different families of Hall probes. The 10μm characteristic line width of the first family provided a $10 \times 10 \mu m^2$ active area which was just small enough for the entry of discrete flux bundles to be discernible. A 2DEG of moderate mobility was used, so the weak localization magnetoresistance did not saturate over the range of applied magnetic fields. Thus both Hall voltage and magnetoresistance could be measured, providing complementary information about the magnetic field penetrating the superconductor. For the second family, the characteristic line width was reduced to 8, 4 and 2μm, with the 2μm structures proving most useful. With the consequent increase in spatial resolution, it was possible to detect not only the entry of flux bundles, but also motion of individual flux vortices in response to changes in temperature and the supercurrent in the Pb film. A high mobility 2DEG was used, so the magnetoresistance saturated at very low fields and was swamped by variations in the Hall voltage at different contacts.

5.2. Pb Films

Pb films were deposited by thermal evaporation directly onto the GaAs/ $Al_xGa_{1-x}As$ Hall bars at room temperature. Some films of Pb alloyed with 1 atom. % In were also deposited. All of the films were 200nm thick and were patterned into strips 20μm wide over the Hall probes. To protect the films from oxidation, some were covered with a thin 10nm layer of Al.

A sample Pb film deposited onto a GaAs substrate was examined in a scanning electron microscope, revealing the granular microstructure shown in Figure 5.1. The average area covered by a single grain was estimated to be $\approx 0.036\mu m^2$ by counting the number of grains in the known area of the micrograph. The grains are approximately circular, so the average grain diameter is $\approx 210nm$, close to the film thickness of 200nm.

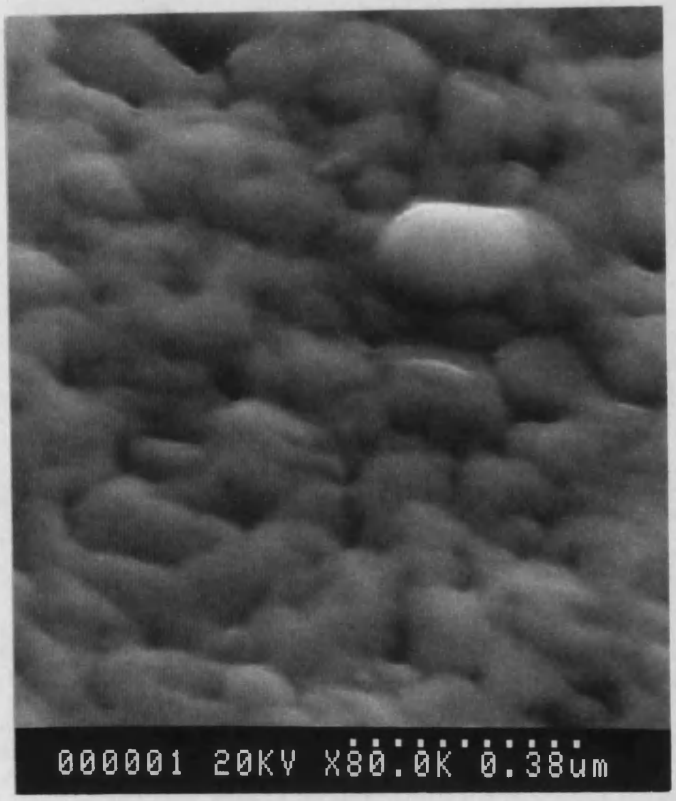

Figure 5.1. Scanning electron micrograph of a Pb film.

Bulk Pb is a type I superconductor, but the 200nm films are thin enough to display type II behaviour for the reasons discussed in Chapter 2. The existence of flux vortices each containing a single flux quantum has been confirmed by decoration experiments carried out on films deposited under similar conditions[47]. A flux line lattice is not visible in the micrograph reproduced in Figure 5.2, but a random vortex arrangement caused by flux pinning.

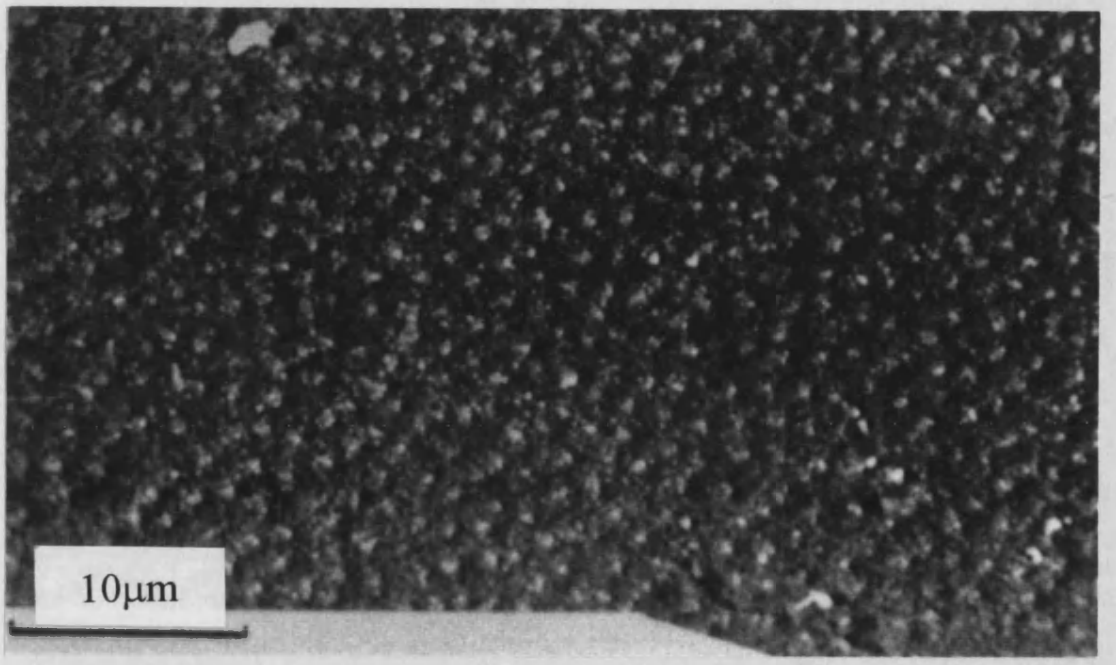

Figure 5.2. The arrangement of flux vortices in a Pb film revealed by decoration with small magnetic particles. The applied magnetic field is 0.8mT.

The characteristic superconducting parameters of the Pb films were determined from resistance measurements in different applied magnetic fields. First of all, the critical temperature T_c was found to be 7.2K from the mid-point of the zero-field resistive transition plotted in Figure 5.3. Next the upper critical field H_{c2} was measured at different temperatures, the results fitted to $H_{c2}(t) = H_{c2}(0)(1-t^2)$ and extrapolated to zero temperature, yielding $\mu_0 H_{c2}(0) = 110 \pm 10\text{mT}$. This value was used to estimate

$\lambda(0) = 53\text{nm}$ and $\xi(0) = 55\text{nm}$, using standard expressions from Ginzburg-Landau theory in the clean limit for bulk materials :

$$\mu_0 H_{c2} = \frac{\Phi_0}{2\pi\xi^2} \text{ and } H_{c2} = \sqrt{2} H_c \frac{\lambda}{\xi}. \tag{5.1}$$

The thermodynamic critical field $\mu_0 H_c$ was assumed to be 80mT, the same as for bulk Pb, because T_c was unchanged. The use of bulk expressions is justified because the films are thicker than the low temperature penetration depth $(d \approx 4\lambda(0))$. The resistivity of the films is approximately $0.6\mu\Omega\text{cm}$ at 8K. From this we estimate that the electron mean free path l^* is ~$0.1\mu\text{m}$ and so the films are in the clean limit $(l^* \approx 2\xi(0))$.

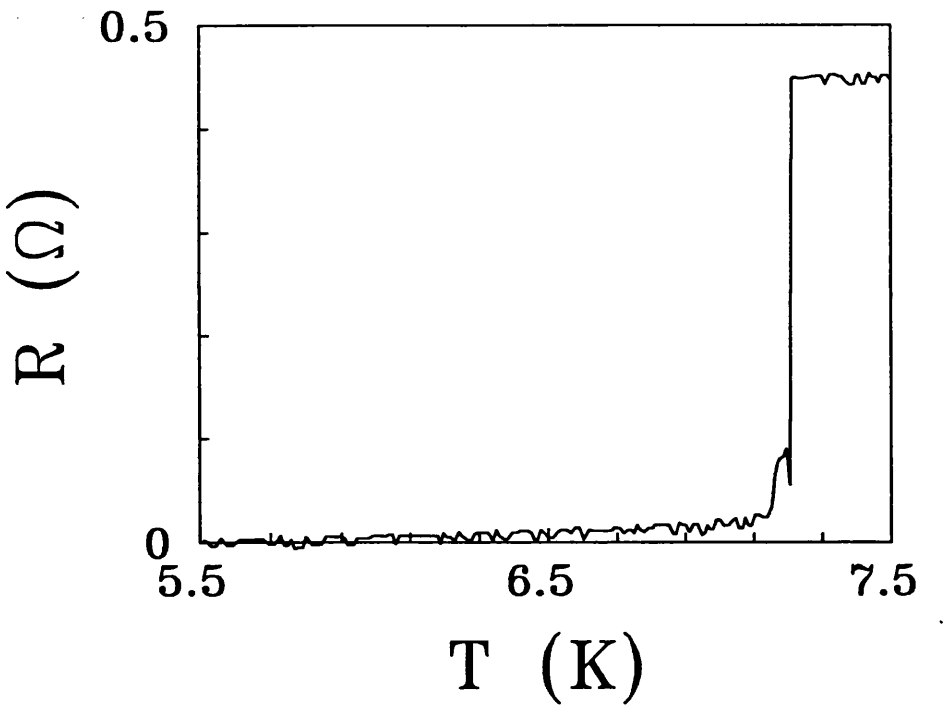

Figure 5.3. The resistance of the Pb film as a function of temperature.

Alloying the Pb with 1% In provides films with different superconducting characteristics. The films have smaller grains, which together with the increased random alloy scattering, contribute to a reduction in the electron mean free path. The shorter mean free path means that ξ is smaller and λ larger, so the Pb(1% In) films are well in the type II regime.

5.3. 10μm Hall Bars

The 10μm Hall bars were fabricated from a GaAs/$Al_xGa_{1-x}As$ heterostructure containing a 2DEG with $n_{2d} = 8.1 \times 10^{15} m^{-2}$ and $\mu = 1.9 m^2 V^{-1} s^{-1}$ at 4.5K. Neither the electron concentration nor the mobility changed significantly over the temperature range covered by the experiments. The mobility is relatively low compared to the high mobilities available and was chosen so that the weak localization magnetoresistance did not saturate at low applied magnetic fields. The 2DEG was at a depth of 44nm below the heterostructure surface.

The Hall bars were grouped in pairs on the GaAs chip. The Pb or Pb(1% In) films described in the previous section were deposited on top of one Hall bar, while a 200nm-thick Au film was deposited on its neighbour. Au does not undergo a superconducting transition so the films provided a normal control below the critical temperature of the superconducting films.

5.3.1. Measurements

There was a measurable magnetoresistance over the moderate range of magnetic fields applied, and thus magnetoresistance as well as the Hall voltage at the 2DEG were investigated as a function of magnetic field. The Hall voltage and magnetoresistance were measured simultaneously, with the Hall contacts bracketed by the magnetoresistance contacts as shown in Figure 5.4. The applied magnetic field was swept up from zero to a maximum value $+H_0$, swept down to $-H_0$ and then back up to $+H_0$, tracing out a hysteresis loop. To ensure that all magnetic field sweeps began from the same initial condition of an equilibrium thermodynamic state, the sample was always cooled from above T_c in zero applied field to the required temperature.

Most of the measurements were taken with a 1μA(rms) ac current flowing through the Hall bar, low enough for there to be linear voltage response, that is the 2DEG was in the ohmic region of its *I-V* characteristic. Decreasing the current further

produced no significant change in either the Hall resistivity or magnetoconductivity. In some measurements the current was deliberately increased, heating the electronic system and thus reducing the weak localization magnetoresistance.

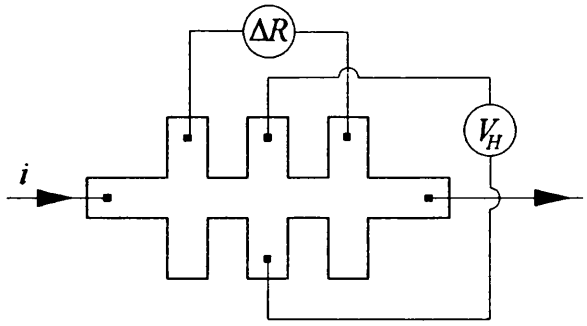

Figure 5.4. The contacts used for the simultaneous Hall voltage and magnetoresistance measurements carried out on the 10μm Hall bar.

5.3.2. Results and Discussion

The Hall resistivity ρ_{xy} of the 2DEG is proportional to the perpendicular component of the local magnetic field over a $10 \times 10 \mu m^2$ area at the centre of the Pb strip. ρ_{xy} is plotted in Figure 5.5 as a function of applied magnetic field H with the Pb film at different temperatures below and above T_c. While the Pb film is in the normal state, it has a negligible effect on the applied magnetic field and as expected $\rho_{xy} \propto H$. But as soon as the temperature drops below T_c the effect of the diamagnetic superconducting Pb film can be seen. At the beginning of the hysteresis loop, as the applied magnetic field is increased from zero, the entry of magnetic flux to the centre of the Pb film is delayed as a result of flux pinning and also any surface barrier against flux entry. When the applied magnetic field is reduced from its maximum value, there is again a delay before flux starts to leave the centre of the film and at zero applied field there is still flux held in the film as a result of flux pinning. Similar behaviour is observed as the external magnetic field is increased on the last leg of the hysteresis loop.

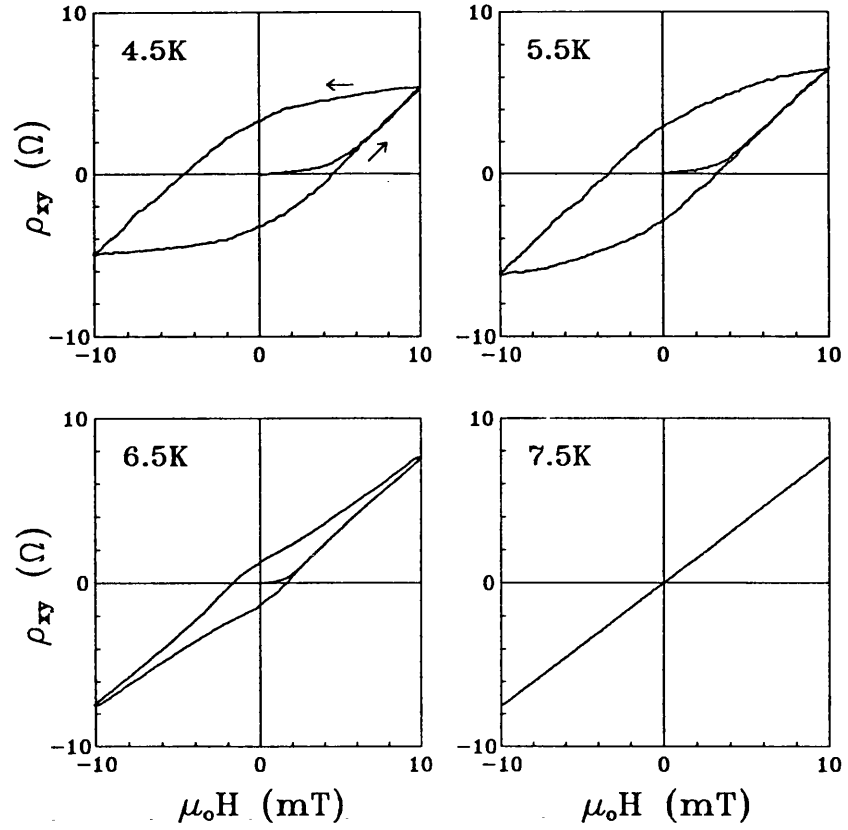

Figure 5.5. Hall resistivity (ρ_{xy}) of the 10μm Pb-gated Hall bar at different temperatures. The arrows indicate the direction of magnetic field sweep.

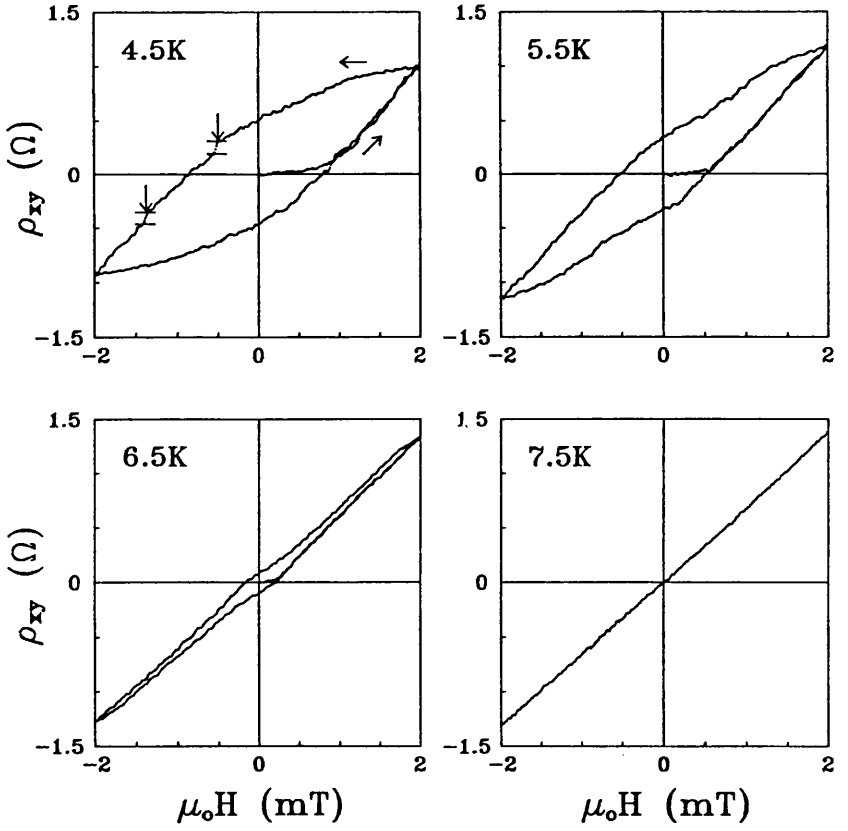

Figure 5.6. Hall resistivity (ρ_{xy}) of the 10μm Pb(1% In)-gated Hall bar at different temperatures. Some flux jumps are indicated on the 4.5K hysteresis loop.

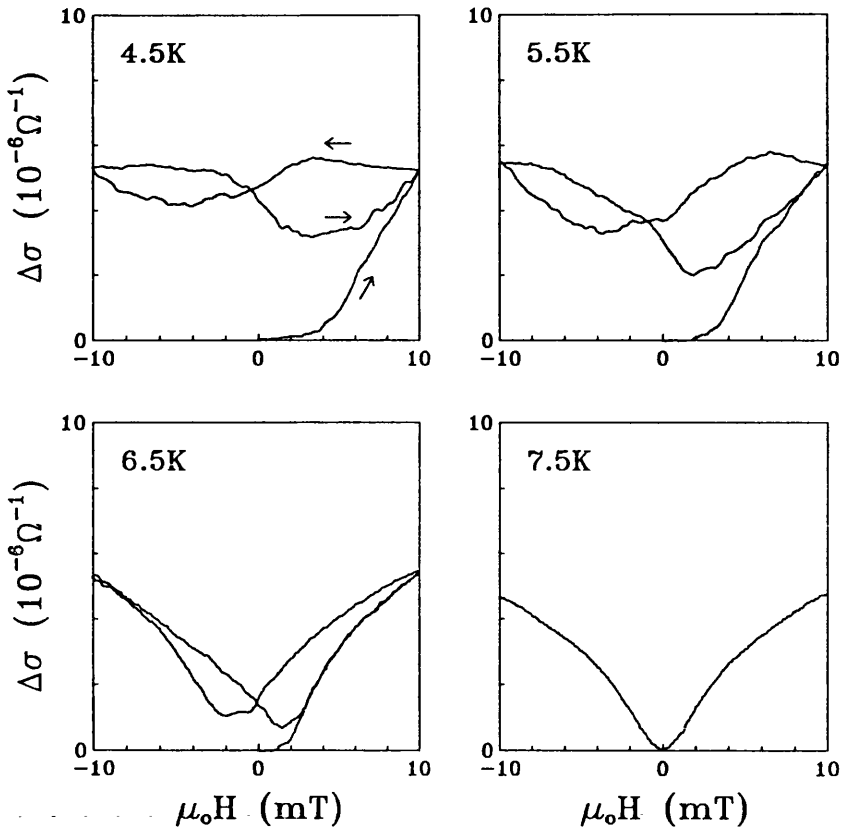

Figure 5.7. Magnetoconductivity ($\Delta\sigma$) measurements for the 10μm Pb-gated Hall bar at different temperatures. Each curve was recorded at the same time as the corresponding curve in Figure 5.5.

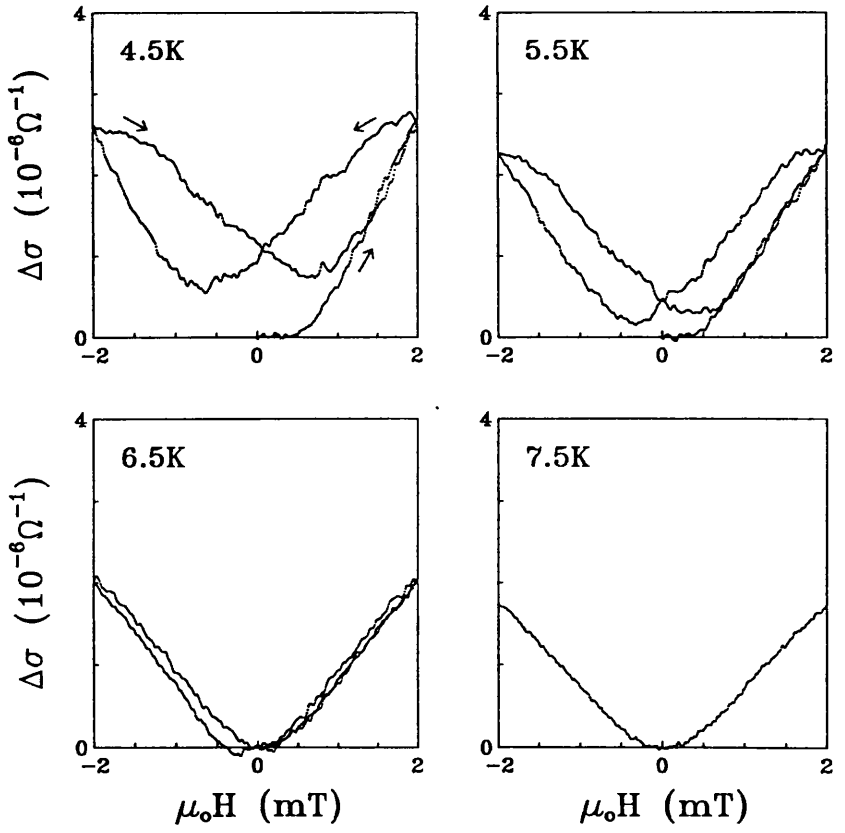

Figure 5.8. Magnetoconductivity ($\Delta\sigma$) measurements for the 10μm Pb(1% In)-gated Hall bar at different temperatures. Each curve was recorded at the same time as the corresponding curve in Figure 5.6.

loop. As the temperature decreases below T_c, flux pinning becomes stronger and the hysteresis loops become wider.

The corresponding measurements for the Hall bar with the Pb(1% In) film are plotted in Figure 5.6. Note the difference in scale of the applied magnetic field. The hysteresis loops displayed by the Pb(1% In) film are much narrower than those of the Pb film, suggesting that flux pinning is much weaker in the Pb(1% In).

The magnetoconductivity $\Delta\sigma$ is plotted at different temperatures for the Pb-gated structure in Figure 5.7 and the Pb(1% In)-gated structure in Figure 5.8. $\Delta\sigma$ also shows hysteretic behaviour below T_c. Whenever the film is normal, the magnetic field penetrates freely, producing symmetrical and non-hysteretic magnetoconductivity curves. The magnetoresistance does not depend on the polarity of the applied magnetic field, so we should expect all the curves to be symmetrical about the y-axis. A varying amount of asymmetry is observed in all of the plots of $\Delta\sigma$ below T_c and is discussed later.

Measurements on the Au-gated control structures showed the expected behaviour for a 2DEG in a uniform magnetic field at all temperatures.

Returning to the Hall resistivity data, it was observed that ρ_{xy} did not always change smoothly with applied magnetic field, but there were sometimes rapid changes over a narrow field range. Two instances are indicated in Figure 5.6 for the 4.5K Pb(1% In) loop. In contrast, measurements on larger area structures[48] display smooth curves as a result of the statistical averaging of flux movements. The 'steps' in Hall resistivity must be caused by a sudden change in the flux threading the 2DEG, due to the movement of a bundle of flux into or out of the superconducting film. The number N of flux quanta observed is easily calculated from the step height $\Delta\rho_{xy}$:

$$N = \frac{\Delta\rho_{xy}}{R_H}\frac{A}{\Phi_0} \qquad (5.2)$$

where A is the $10\times10\mu m^2$ active area of the Hall probe. For jumps such as those indicated in Figure 5.6, typically 4-10 flux quanta are involved. Jumps due to single flux quanta are not observed but the change in Hall resistivity caused by a single flux quantum ($\approx 0.01\Omega$) is at the limit of sensitivity. The measurements with smaller, more sensitive Hall probes discussed below confirm that motion in small bundles is the norm. Since the active Hall area is enclosed by the longitudinal voltage contacts, and ρ_{xy} and $\Delta\sigma$ were measured simultaneously, there should be features in $\Delta\sigma$ corresponding to the flux jumps observed in ρ_{xy}. Figure 5.9 shows just such an instance where the indicated jump in Hall resistivity corresponds to a change in magnetoconductivity. The active Hall area is about 1/5 of the area giving $\Delta\sigma$, so the same fraction of jumps in $\Delta\sigma$ should be correlated with those in ρ_{xy}. This estimate is in reasonable agreement with our observations.

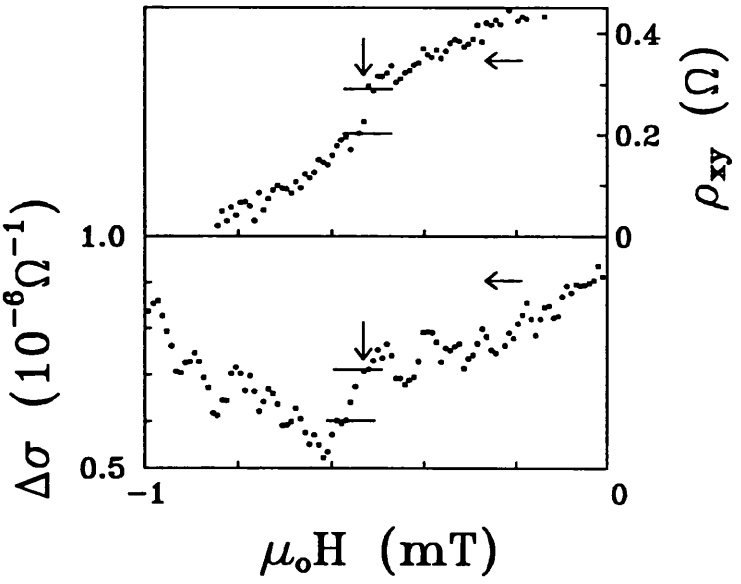

Figure 5.9. Detail of a simultaneous Hall resistivity and magnetoconductivity measurement for the 10μm Pb(1% In)-gated Hall bar at 4.5K. A flux jump detected at the same time in both traces is indicated.

In the low field limit where the flux vortices are widely separated, the Hall resistivity and magnetoconductivity give complementary information about the flux threading the superconductor. The Hall resistivity is antisymmetric in magnetic field

and depends on the net flux density, that is the difference between the densities of vortices n_+ and antivortices n_-. The magnetoconductivity is insensitive to the polarity of the magnetic field, depending on the sum of the vortex densities n_+ and n_-. Using ρ_{xy} and $\Delta\sigma$ in a simple qualitative model, it is possible to calculate the densities of vortices and antivortices present at the centre of the superconducting film. From Figure 5.4, it may be seen that different, although overlapping, areas of superconductor are covered by the measurements of ρ_{xy} and $\Delta\sigma$. It is therefore necessary to assume that n_+ and n_- are uniform throughout the central region of the film on the 10μm scale set by the Hall bar dimensions. This is reasonable because the deviations from uniformity evidenced by the jumps in ρ_{xy} and the asymmetry in $\Delta\sigma$ are relatively small compared to the smooth total background signals.

Because the vortices are well-separated at low applied magnetic fields, each one makes an individual contribution to the Hall resistivity and magnetoconductivity and so

$$\rho_{xy} = k_\rho(n_+ - n_-) \tag{5.3}$$

and

$$\Delta\sigma = k_\sigma(n_+ + n_-) \tag{5.4}$$

where n_+ and n_- are the numbers of vortices and antivortices per unit area respectively and k_ρ and k_σ are constants of proportionality. It follows that

$$n_+ = \tfrac{1}{2}\left(k_\sigma^{-1}\Delta\sigma + k_\rho^{-1}\rho_{xy}\right) \tag{5.5}$$

and

$$n_- = \tfrac{1}{2}\left(k_\sigma^{-1}\Delta\sigma - k_\rho^{-1}\rho_{xy}\right). \tag{5.6}$$

The constant k_ρ is found using the Hall resistivity and the known applied flux density when the film is in the normal state. Below T_c, assuming that only vortices are present on the initial upward sweep from zero field to H_o implies that $k_\sigma^{-1}\Delta\sigma - k_\rho^{-1}\rho_{xy} = 0$ and solving this yields k_σ. n_+ and n_- are plotted in Figure 5.10 for both the Pb and

Pb(1% In) films at 4.5K, calculated using the appropriate pairs of Hall resistivity and magnetoconductivity measurements in Figures 5.5 to 5.8.

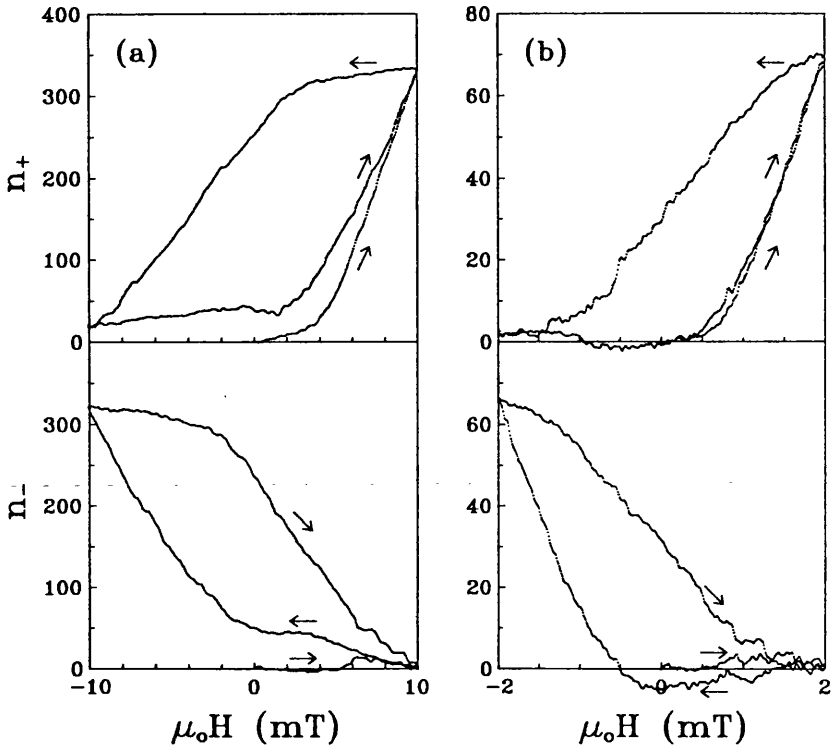

Figure 5.10. (a) Densities of vortices n_+ (top) and antivortices n_- (bottom) in the Pb film at 4.5K as a function of applied magnetic field. The y-axis is in units of number of vortices per $100\mu m^2$. Arrows indicate the direction of magnetic field sweep. (b) Vortex and antivortex densities in the Pb(1% In) film at 4.5K.

Referring to the Pb film data in Figure 5.10(a), note that soon after the applied flux density is reduced from the maximum value of 10mT, antivortices start to appear, despite the applied field still being positive. This is not observed at higher temperatures and not at all for the Pb(1% In) film. The early entry of antivortices is attributed to the stronger flux pinning in the Pb film at low temperatures in the following way. As the applied magnetic field is reduced, vortices trapped in the film by pinning produce an additional field outside the film because the magnetic flux lines must be closed. This additional field is opposed to the applied field near the edge of the gate and when the

resultant field becomes negative, antivortices begin to enter. It is also possible to observe vortex-antivortex annihilation in Figure 5.10(a). On the downward sweep, the vortex density n_+ decreases slowly at first, but as the decreasing applied field approaches zero, n_+ drops more rapidly. At the same time there is a slight drop in n_-, which is a clear indication of vortex-antivortex annihilation. Subsequently n_+ continues decreasing while n_- increases rapidly, masking any further annihilation. The same behaviour is observed when the magnetic field sweep is reversed again on the last leg of the hysteresis loop. Any asymmetries in the Hall resistivity or the magnetoconductivity are also reflected in the figures and must be taken into account when considering the results. The asymmetries are most probably a consequence of inhomogeneities in flux penetration on the scale of the 10μm Hall bar and are neglected by the simple model.

All of the measurements discussed above were taken with a 1μA(rms) ac current passing through the Hall bar that was small enough for the 2DEG to be in the ohmic regime. The structures were also investigated at higher currents up to 16μA(rms), with the results shown Figure 5.11 where $\Delta\sigma$ is plotted for both a Au-gated and a Pb-gated structure with different currents flowing through the Hall bar at 4.5K. The effect of increasing the current, most clearly seen in the Au-gated structure, is to reduce the symmetrical weak localization contribution to the magnetoconductivity because the stronger electric field increases the electronic temperature[49] in the 2DEG. The zero field resistance changes slightly with current and is equivalent to the effect of an increase in lattice temperature of a few Kelvin. The Hall resistivity which is only sensitive to the temperature of the superconductor below T_c, changes very little with current, indicating that there is no significant heating of the gate. For the Pb-gated structure, the loss of the symmetrical weak localization component leaves behind an asymmetrical component of constant magnitude, attributed to inhomogeneities in magnetic flux distribution along the film on a scale greater than that set by the dimensions of the Hall probes. Such a flux inhomogeneity would give rise to different

transverse Hall voltages at neighbouring pairs of contacts, and this difference would be mixed into the longitudinal voltage measurement for the magnetoconductivity. The asymmetrical contribution does not depend on the magnetic history of the superconductor, as reversing the direction of field sweep around the hysteresis loop made no change.

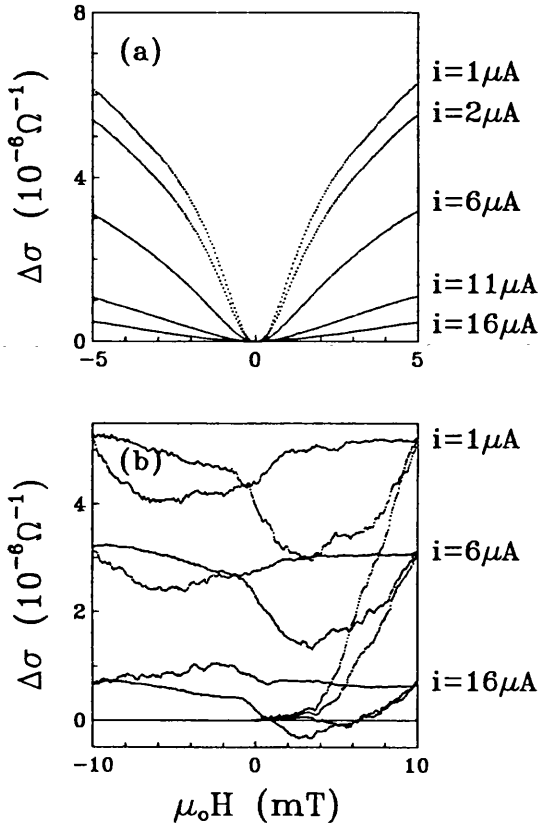

Figure 5.11. (a) Magnetoconductivity of the 10μm Au-gated structure at 4.5K for different applied currents. (b) Magnetoconductivity of the 10μm Pb-gated structure at 4.5K for different currents.

5.4. 2μm Hall Bars

A second family of Hall bars was fabricated with smaller characteristic linewidths of 2, 4 and 8μm. The 2DEG with $n_{2d} = 2.9 \times 10^{15}\,\mathrm{m}^{-2}$ and $\mu = 81\mathrm{m}^2\mathrm{V}^{-1}\mathrm{s}^{-1}$ at 7.5K was now at a depth of 80nm below the heterostructure surface. Pb films were

deposited under similar conditions as before with the same 200nm thickness and 20μm width over the Hall bar.

Previously just one gold wire had been attached to the films for grounding purposes, but now four wires were attached, allowing the application of transport currents and measurement of voltages at the Pb film in addition to the measurements at the Hall probe. Thin Pb films are vulnerable to destruction by thermal runaway during flux flow experiments[50] and to protect against this, a shunt of constantan wire was connected in parallel with the Pb film at the chip carrier. The shunt resistance was 4-5 times the normal state resistance of the film at low temperature, and was up to 2 orders of magnitude greater than the tiny sample resistances at the onset of flux flow.

With the greater spatial resolution offered by the smaller Hall bars and the possibility of running a supercurrent through the Pb film, two new classes of experiment could be performed where the Hall voltage was monitored while the temperature or supercurrent were varied. The results are presented below, after a discussion of the magnetic field sweeps.

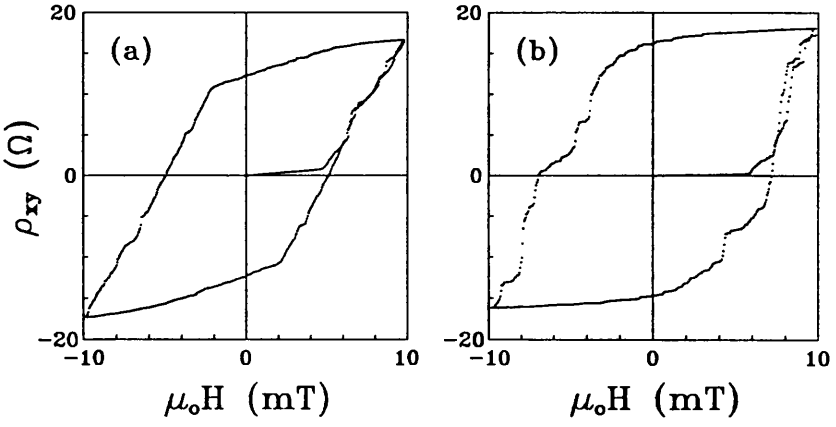

Figure 5.12. (a) Hall resistivity (ρ_{xy}) of a 8μm Pb-gated Hall bar at 4.3K. (b) Hall resistivity (ρ_{xy}) of a 4μm Pb-gated Hall bar at 4.3K.

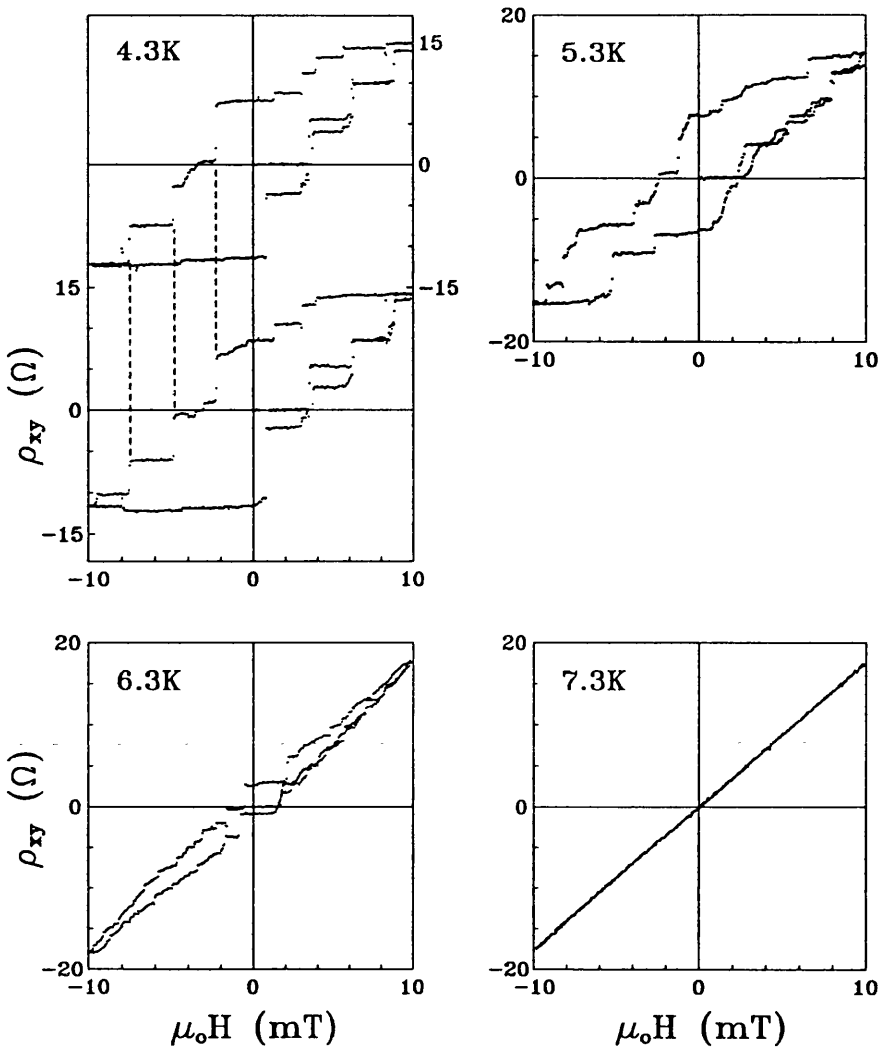

Figure 5.13. Hall resistivity (ρ_{xy}) of a 2μm Pb-gated Hall bar at different temperatures. At 4.3K, ρ_{xy} was measured simultaneously at two Hall probes separated by 4μm. A resistivity of ~1Ω corresponds to a single flux line threading the $2\times2\mu m^2$ detector.

5.4.1. Magnetic Field Sweeps

Hysteresis loops were recorded in the same way as before - the film was cooled in zero field to the desired temperature and the applied magnetic field cycled while the Hall voltage was recorded. The reduction in Hall probe dimensions has striking consequences as can be seen by comparing the 4.3K hysteresis loops in Figures 5.12 and 5.13 for line widths decreasing from 8 to 4 to 2μm. As the active area of the Hall

probe shrinks and flux movements are averaged over a smaller area of superconductor, the discrete nature of the flux vortices or bundles becomes progressively clearer. The hysteresis loop for a 2μm Hall bar consists almost entirely of flat sections where there is no change in the flux threading the area of Pb film being monitored, separated by discontinuous steps corresponding to the entry of a flux bundle. The number of flux vortices in the portion of the flux bundle detected can be calculated from the step height and is found to be as many as 10 for the 2μm structures at 4.3K. The hysteresis loop at a particular contact was not repeatable. The overall shape of the loop remained the same, but the position and height of the steps varied. The magnetic field sweep rate was varied from 2 to $10 mT.min^{-1}$ with no great effect on the hysteresis loops beyond a sharpening of the flux jumps, as the output of the lock-in amplifiers had more time to settle between measurement points. The magnetic field was usually swept at the slower rate in order to obtain well-defined steps. On increasing the temperature, the hysteresis loops become narrower and more rounded, composed of smaller flux jumps, as can be seen in Figure 5.13. This suggests that the weaker flux pinning results in the entry of flux bundles containing fewer vortices.

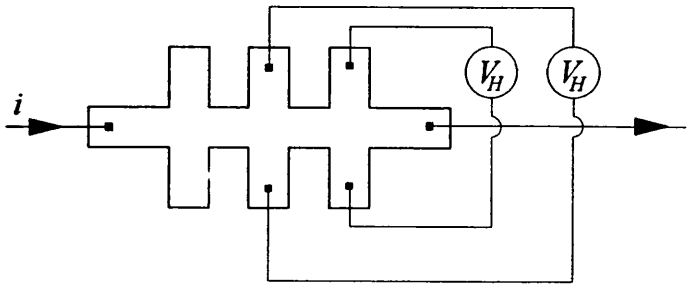

Figure 5.14. Contacts at 4μm separation used for simultaneous Hall voltage measurements on the 2μm Hall bar.

Interesting results were obtained by measuring the Hall voltage simultaneously at two different pairs of contacts on the same Hall bar, in the arrangement shown in Figure 5.14. The two 4.3K hysteresis loops in Figure 5.13 illustrate a typical result for probes 4μm apart. The probe separation is taken as that between probe centres. A

number of flux jumps occur simultaneously, implying that the same flux bundle extends over both pairs of contacts. The proportion of simultaneous steps falls off rapidly as the probe separation is increased. The following approach was taken to quantify these observations. Steps were identified either by inspection of the hysteresis loop, or by taking a numerical derivative of the loop. The latter procedure gives a sharp spike at every step which is easily detected by a simple computer program. The total number of steps N_{tot} was counted up on both of the two simultaneously recorded hysteresis loops, and the number of simultaneous steps N_{sim} also determined. A simple correlation coefficient defined for $N_{tot} > 0$ as $c = \frac{2N_{sim}}{N_{tot}}$ will always lie in the range $0 \le c \le 1$ depending on the degree of correlation between the two loops. If there are no simultaneous steps, then $N_{sim} = 0$ and so $c = 0$. On the other hand, if the two loops are perfectly correlated, that is every step in loop A occurs at the same time as every step in loop B, then $N_{sim} = \frac{1}{2} N_{tot}$ and we have $c = 1$. Note that if the probe separation is zero, by definition $c = 1$.

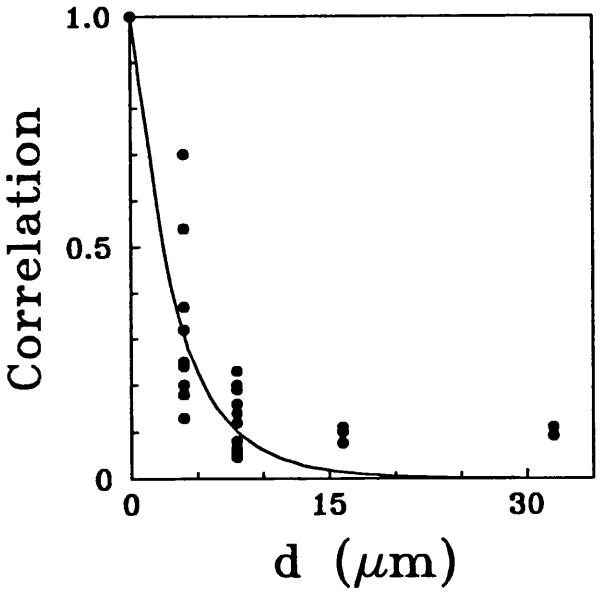

Figure 5.15. The correlation measured at different separations at 4.5K. The solid curve is a fit to the model described in the text with a flux bundle radius of 2.6μm.

The correlation c was determined for many pairs of Hall probes at different separations and the results are plotted in Figure 5.15. A simple model was developed to describe the correlation data. The flux bundles were assumed to be rigid cylinders of radius r that enter the centre of the Pb film distributed randomly along its length. If all of the flux bundles have the same radius r, from simple geometrical considerations c is given by

$$\begin{aligned} c(r,d) &= 1-\frac{d}{2r+w} \quad \text{for } d \le 2r+w \\ &= 0 \qquad\qquad\quad \text{for } d > 2r+w \end{aligned} \tag{5.7}$$

where d is the probe separation and w the linewidth of the Hall probe. This straight line form for c does not fit the experimental data very well, so the additional assumption was made that the flux bundles do not have a fixed radius but have some distribution of radii. A realistic distribution should be weighted more heavily towards smaller flux bundles, decreasing to zero as the bundle radius increases. A Poisson distribution of radii seems reasonable : $\rho(r,r_0)=\frac{1}{r_0}\exp(-r/r_0)$ where r_0 is the mean radius. Now we calculate a mean correlation coefficient

$$\langle c(r_0,d)\rangle = \int_0^\infty c(r,d)\rho(r,r_0)dr. \tag{5.8}$$

The solid line in Figure 5.15 is a best fit of the data to this expression with $r_0 = 2.6\pm0.2\mu m$, implying that the flux bundle diameter at 4.3K is approximately 5μm. Within experimental error, the flux bundle diameter remains the same at 5.3K and 6.3K.

The collective pinning theory of Larkin and Ovchinnikov[24] introduced in Chapter 2 gives a theoretical estimate of the collective pinning correlation radius $R_c = \frac{C_{66}\,a}{f_p\sqrt{n_p}}$ which can be computed at a fixed magnetic flux density B. The density of pinning sites n_p was assumed to be the same as the density of Pb grains, the pinning

force f_p was measured in a separate experiment described below and the vortex spacing $a \approx \sqrt{\Phi_0/B}$. The flux lattice elastic modulus C_{66} was estimated using the relation[25] $C_{66} = \frac{1}{2}\int_0^{B_0} B^2 \frac{\partial^2 H}{\partial B^2} dB$ with $B(H)$ obtained from the averaged magnetization measurements on the larger 10μm Hall bars. R_c was found to be $\approx 1.25\mu m$ at 5mT, comparing favourably with the experimental value r_0.

The 2μm hysteresis loops provided an opportunity of testing the calculation in Chapter 4 which can be used to determine the separation between the Hall probe and the superconductor. The larger Hall probes are not suitable because they extend too far over the central region of the film and pick up magnetic field from the edges of the strip. The calculation requires the field measurement to be made at a point above the centre of the strip. Looking at the 4.3K hysteresis loops in Figure 5.13, the slope at the beginning of the loop appears to be zero but with magnification, a small positive gradient is found. The slope was measured over a range from 0 to 2mT, when the strip should still be in or close to the Meissner state. Using the relation $z_0 = W\frac{H(z_0)}{H_a}$, where W is the half-width of the Pb strip, the separation between Hall probe and superconductor was found to be $z_0 = 180 \pm 40\text{nm}$. Considering the actual dimensions involved, the depth of the 2DEG is 80nm while the Pb film is 200nm thick. The spacing between the 2DEG and the middle of the film is thus 180nm, in excellent agreement with the calculated value.

5.4.2. Temperature Sweeps

In the second class of experiments, the applied magnetic field and supercurrent (if any) were held constant while the temperature was slowly altered. Most of the temperature sweeps were carried out according to the following procedure. The sample was cooled through T_c to the initial temperature $T < T_c$ in a constant magnetic field, ensuring an equilibrium arrangement of flux vortices such as that shown in Figure

5.2 with the flux vortices arranged not on a flux line lattice but in a disordered array determined by competition between flux pinning and vortex interactions. The flux density through the superconducting film remains on average constant, as confirmed with larger area probes[36]. With the magnetic field held constant, the temperature was slowly increased while the voltage at a single Hall probe was monitored. If the temperature sweep was performed with a supercurrent passing through the Pb film, the supercurrent was only switched on when the film had been cooled to the initial temperature, so that all the sweeps could start from the same equilibrium vortex arrangement.

Even in zero applied magnetic field, a small non-zero transverse voltage was always measured at any Hall contact. Despite accurate positioning of the Hall voltage contacts, they will not necessarily lie on an equipotential and the resulting small resistive voltage appears as an offset to the Hall voltage at zero field. The offset was always less than about 10% of the longitudinal voltage between nearest neighbour pairs, equivalent to a physical misalignment of the voltage contacts of less than 0.4μm. In measurements at constant temperature, the offset presented few problems and was subtracted from the processed data. However, the offset was found to be temperature dependent, giving the impression of a changing magnetic field when in fact there was none. Since the physical layout of the Hall probe does not change with temperature, the origin of the change in the offset must be a temperature-dependent rearrangement of the electron distribution in the region of the voltage contact. Fortunately the change in the offset was small and linear over the temperature range of the measurements, confirmed on temperature sweeps with zero applied field. For the sweeps in an applied field, the linear slope of the Hall voltage above T_c was extrapolated to lower temperatures and subtracted from the entire sweep, giving satisfactory results.

Figure 5.16 shows some temperature sweeps made in an applied flux density of 0.5mT which is small enough for there to be on average just one flux vortex threading

the $2 \times 2\mu m^2$ active area of the Hall probe. The measured Hall resistivity is converted using n_{2d} into the quantity of magnetic flux $\Phi(T)$ through the detector. The quantity $\Delta\Phi$ plotted against temperature in Figure 5.16 and subsequent plots is $\Delta\Phi = \Phi(T) - \Phi(T_c)$, the difference between the measured flux and the constant flux observed when the film becomes normal at T_c and above.

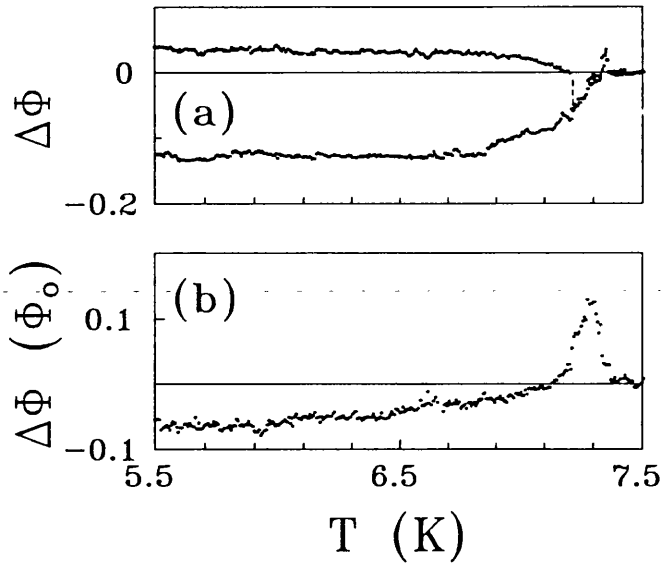

Figure 5.16. (a) The change in flux ($\Delta\Phi$) threading a Hall probe as a function of temperature in an applied field of 0.5mT. The two traces were recorded at the same Hall probe with the Pb film containing two different vortex configurations. (b) The same measurement performed at a different Hall probe.

The changes in $\Delta\Phi$ in Figure 5.16 correspond to vortices moving in the superconducting film, causing the amount of flux threading the Hall probe to increase or decrease slightly. The changes can be firmly attributed to the superconductor because for $T > T_c$ the Hall probe produces a constant signal. As discussed in Chapter 3, the Hall voltage depends on the net flux threading the active area, not on whether it is distributed into fluxons or not. At the microscopic level there is an absence of ensemble averaging and small differences in the measured flux density should be expected on field cooling as a result of (i) local inhomogeneities in the randomly

pinned vortex distribution and (ii) the effect of the location of a vortex in the active area of the Hall probe, that is a vortex in the middle of a probe should produce a larger Hall voltage than a vortex half-in half-out at the edge of the probe.

Returning to Figure 5.16, at 0.5mT the changes in measured flux are usually smooth and continuous, reflecting small movements of a single vortex towards or away from the edge of the probe due to changes in the pinning potential arising from the temperature-dependent superconducting parameters (e.g. λ and ξ). Rearrangement of vortices has also been observed in a thin Nb foil by the technique of Lorentz microscopy, where the vortex configuration is seen to approach a more regular hexagonal lattice as temperature increases[51].

In Figure 5.16(a), there are two temperature sweeps recorded at the same contact. The initial vortex configuration is different, showing that field cooling does not always lead to the same arrangement. Approaching T_c the lower trace smoothly approaches the uniform flux density of the normal state, while the upper trace shows the vortex hopping into the lower configuration, a few tenths of a Kelvin below T_c. A different feature is illustrated in Figure 5.16(b) for a temperature sweep at another probe, where there is a peak or concentration of flux just below T_c. This *increase* in inhomogeneity is not expected for vortices approaching a uniform flux line lattice or the homogeneous flux distribution of the normal state. If the temperature sweep is repeated with magnetic fields of different intensities, the peak is not observed at all fields but only at some, suggesting that its origin does not simply lie in the properties of the particular piece of superconductor but must also depend on vortex interactions.

As the applied magnetic field is increased, the temperature sweeps remain fundamentally the same. It is possible to observe the dependence of critical temperature on applied magnetic field. A temperature sweep in a flux density of 10mT is shown in Figure 5.17 and note that T_c has been reduced to 6.7K. With increasing magnetic field, the vortices are closer together and vortex interactions become more

important. The peak or concentration of flux below T_c becomes wider, suggesting that the stronger vortex interactions can influence the vortex arrangement at temperatures further below T_c where pinning is stronger relatively speaking. In addition at 10mT, some Hall probes displayed discontinuous traces. In the temperature sweep in Figure 5.17, discrete steps in the measured flux can be seen as temperature approaches T_c and the vortices suddenly rearrange themselves under the competing influences of pinning forces and vortex interactions. At this larger field, the vortex interaction becomes so strong that a small cluster of vortices hops between different minima of the collective pinning potential at certain threshold temperatures. The repulsive force per unit length exerted on a vortex by a neighbour is given by

$$f_2 = \frac{\Phi_0^2}{2\pi\mu_0\lambda^3}\sqrt{\frac{\pi\lambda}{2r_2}}\exp(-r_2/\lambda) \qquad (5.9)$$

for a vortex separation $r_2 >> \lambda$. The mean vortex separation at 10mT is 490nm and, taking into account the temperature dependence of λ, the intervortex force at 6.5K is estimated to be $\sim 10^{-6}\,\mathrm{Nm}^{-1}$. This is comparable with the single vortex pinning force at this temperature as measured in the next set of experiments, lending strength to the idea that competition between the two forces is important here.

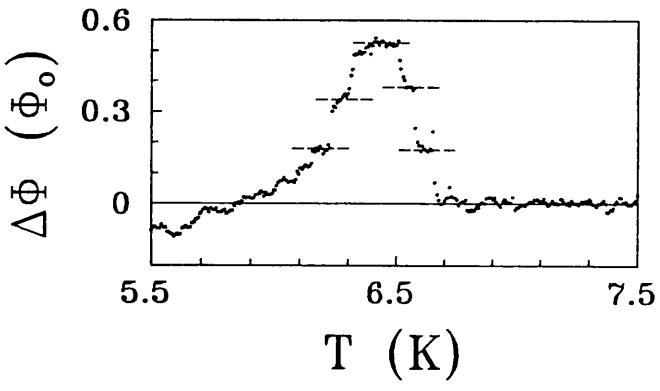

Figure 5.17. The change in flux ($\Delta\Phi$) threading a Hall probe as a function of temperature at an applied field of 10mT.

Modelling a vortex as a uniform cylinder of flux of radius $\lambda(T)$, the Hall voltage can be considered to measure the area of intersection between this cylinder and the active part of the Hall probe (assumed to be defined by the square intersection of voltage and current leads). Considering the two extreme cases of a cylinder with either its circumference or its axis just touching the edge of the active area, a change in Hall voltage can be converted to a lateral displacement of a flux vortex. In the case of the hopping flux bundles observed in Figure 5.17, with the assumption that just one critical vortex near the probe perimeter is responsible for the change in threaded flux and that elastic distortions of the bundle are small compared to the bundle displacement, we can estimate that the correlated vortex regions are moving distances of 20-40nm during jumps.

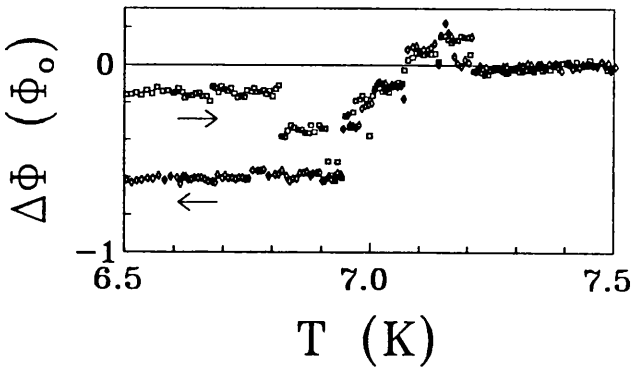

Figure 5.18. The change in flux ($\Delta\Phi$) threading a Hall probe in a 0.5mT applied field and with a $5\times10^{5}\,\mathrm{A\,cm^{-2}}$ current density passing through the Pb film. The arrows indicate the direction of temperature sweep.

Temperature sweeps were also carried out with a constant supercurrent passing through the Pb film. The aim was to investigate flux pinning forces and the results are included with those obtained from supercurrent sweeps in the next section. Two sweeps in a 0.5mT applied magnetic field are displayed in Figure 5.18 for comparison. The starting point for the warming sweep was reached by field cooling the Pb film with zero applied supercurrent. The supercurrent was applied after the film had reached the

initial temperature, and this was the procedure usually followed. The supercurrent exerts a Lorentz force on the vortex, and when a threshold temperature is reached, the Lorentz force equals the pinning force and there is a discontinuous step. Thereafter there is an irregular sequence of steps reflecting flux creep in the film, until T_c is reached. The second sweep was recorded as the film was cooled from above T_c with the supercurrent flowing through the film. As the temperature decreases, the sequence of flux movements is retraced, until at a certain temperature the traces separate, and a non-equilibrium vortex arrangement is frozen in.

5.4.3. Current Sweeps

The final class of experiments was performed at constant magnetic field and temperature while the dc supercurrent flowing in the Pb film was changed. As for the temperature sweeps, the films were cooled from above T_c in the applied magnetic field to the target temperature with no supercurrent flowing in the film so that the current sweep could start from an equilibrium configuration. The supercurrent was then ramped up from zero to some large value. The voltage drop across the film was monitored so that the resistance of the film could be correlated with the Hall probe observations.

Some current sweeps in a 1mT applied flux density at different temperatures are shown in Figure 5.19. There are on average just two flux vortices in the active probe area, they are well separated and vortex interactions can be ignored. Note that just above the critical temperature at 7.3K, the Hall voltage is not affected by the applied current and the flux threading the Hall probe remains constant, as would be expected. The magnetic field generated by the current flowing in the Pb strip is negligible. Below T_c the threaded flux also remains constant as long as the current density in the film is much less than the critical current density : $j << j_c$. When sufficient current is applied, a threshold current is reached where there is a sudden

discontinuous change in the threaded flux, followed by an irregular sequence of square steps as the current increases further. At still higher temperatures ($T < T_c$), these steps give way to a smooth upwards curve indicating that the net flux threading the probe is continuously increasing. Just below T_c, only the smooth curve is observed, which at a certain current rolls off, yielding the normal state behaviour.

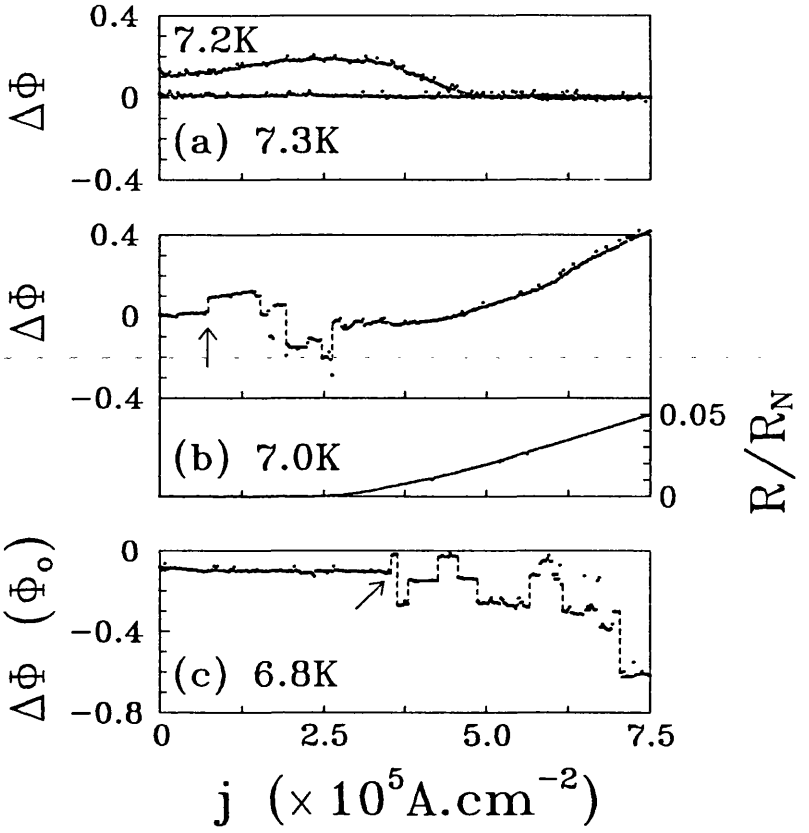

Figure 5.19. (a)-(c) The change in flux ($\Delta\Phi$) threading a Hall probe as a function of current density in the Pb film at various temperatures in a 1mT applied field. The arrows in (b) and (c) indicate the feature used to calculate pinning forces. Included in (b) is the flux flow resistance of the Pb film normalised by the normal state resistance at 8K.

By comparing the behaviour of the Hall voltage with four-point dc *I-V* measurements performed directly on the Pb film, it is possible to interpret the above behaviour. One of the resistance measurements is plotted below the Hall trace in Figure 5.19(b). In the Hall trace, the initial abrupt step-like structure represents the

onset of flux creep where individual vortices hop between pinning sites. Comparing this with the resistance measurement, it can be seen that flux creep is observed well before it is possible to measure a flux flow resistance. The smooth upwards curvature at the end of the Hall trace corresponds to the onset of flux flow.

In the flux creep regime, assuming that the dc current in the film is uniformly distributed, it is possible to estimate the Lorentz force $\mathbf{f}_L$ on a vortex, $\mathbf{f}_L = \mathbf{j} \times \Phi_0$ where $\mathbf{j}$ is the current density in the film and Φ_0 is a vector of magnitude the flux quantum directed along the vortex line. The threshold current at which the first step is observed (indicated by the arrows in Figures 5.19(b) and (c)) yields a Lorentz force equal to the pinning force for the vortex at that particular position. The initial step is repeatable, but the subsequent steps occur at different currents although they do have similar amplitudes from sweep to sweep. Different Hall probes show the initial step at different current densities, that is the pinning force is different at different parts of the Pb film. The pinning force at one specific site $f_p(t)$ is plotted in Figure 5.20.

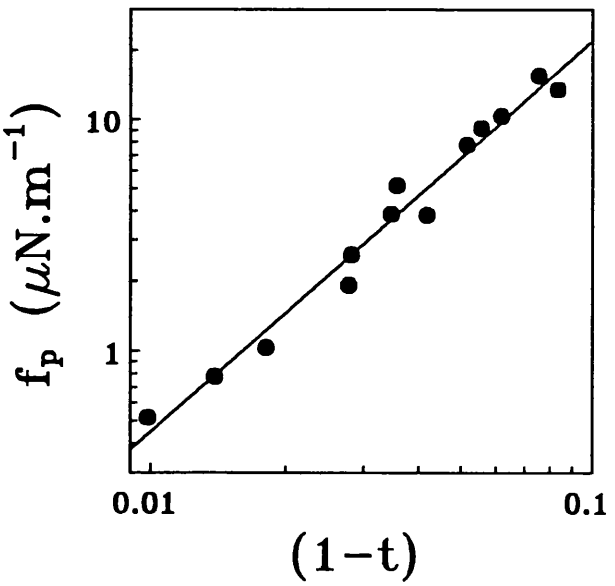

Figure 5.20. Pinning force at one particular site in the Pb film plotted as a function of $(1-t)$. The straight line is a fit to an empirical form (see text).

The solid line is a best fit to the empirical power law

$$f_p(t) = f_p(0)(1-t)^n \qquad (5.10)$$

where $t = T/T_c$ is the reduced temperature. It was found that the parameter $f_p(0)$ varies over a range $0.8-3.0\times10^{-6}\mathrm{Nm}^{-1}$ and the exponent n from $1.5-2.0$ for different pinning sites. From the micrograph in Figure 5.1, we know that the Pb films are granular with a grain size of ~200nm. As well as there being increased electron scattering at the grain boundaries, there also appears to be a reduction in film thickness there, so it is highly likely they are the dominant pinning sites in our films. The wide spread in the measured values of n suggests that there is no generic temperature dependence for this pinning mechanism, rather it depends on the microscopic details of the pinning site. In experiments using a Josephson junction to locate vortices in 380nm-thick Pb films[52], it was found that $n \approx 1$ from measurements over a similar temperature range. The difference in exponent and the rather smaller values of pinning force perhaps reflect differences in film thickness and quality.

The points in Figure 5.20 are a compilation of data for a specific pinning site gained from two types of experiment : sweeps of supercurrent with temperature held constant as described above, as well as temperature sweeps with the supercurrent held constant. The applied magnetic fields were 0.5mT and 1mT, that is 1 or 2 flux vortices in the active area of the Hall probe. At these magnetic fields, the mean vortex spacing is so large that intervortex interactions are negligible and there will be no collective pinning. The fact that the initial Hall voltage step used to obtain the pinning force is repeatable in size and direction at different temperatures and both magnetic fields is good evidence that a single vortex at a single pinning centre is involved. In addition, the data points fall on a single universal curve. Returning to the model used in the previous section to estimate vortex hopping distances, the height of the steps in Figure 5.19 imply that vortices are travelling ~20-40nm during hops. Taking into account the

microstructure of the film, it seems most likely that the vortices are moving short distances along grain boundaries.

In the flux flow regime, bundles of vortices cross the detector extremely rapidly so that individual vortices cannot be resolved and an average voltage is measured. The upward trend to the Hall voltage in this regime is consistent with a vortex/antivortex nucleation mechanism for the critical current in these films whereby vortices and antivortices enter at opposite edges of the film, move towards the centre under the influence of the Lorentz force and annihilate each other. Due to the existence of an applied magnetic field, the annihilation point will be off-centre, and the probe, which is near the geometrical centre of the film, will see an increased vortex density.

Figure 5.21 plots the change in flux threading the detector upon application of a supercurrent at 6.2K in a 10mT applied field. The apparent increase in noise in this figure is an instrumental artefact resulting from the subtraction of the background Hall voltage which is now ten times larger. The signal has now assumed a pronounced sawtooth-like profile. At this magnetic field, the vortices are close enough for collective effects to be expected and the sawtooth is interpreted as arising from smooth elastic distortions of correlated regions of flux vortices followed by sudden jumps when a local collective pinning force is exceeded.

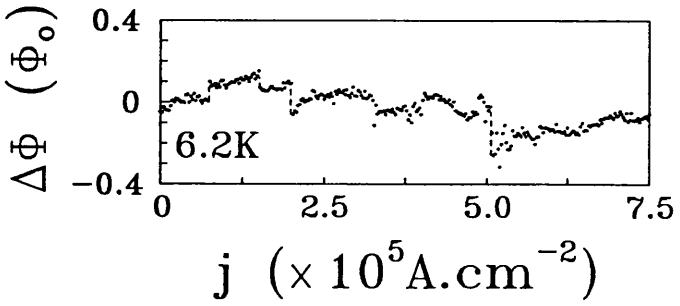

Figure 5.21. The change in flux (ΔΦ) threading a Hall probe as a function of current density in the Pb film at 6.2K in a 10mT applied field.

Chapter 6

Niobium Films

6.1. Introduction

Unlike the directly deposited Pb films, the Nb film was deposited onto a separate substrate and attached to the Hall bar with a thin layer of adhesive, the additional separation creating another obstacle to the resolution of single flux vortices. With care the adhesive layer could be made thin enough to allow fluxon-resolved investigations of flux bundle entry and of vortex movements in response to temperature changes and an applied supercurrent.

The same three types of experiment described in the last chapter, sweeps of magnetic field, temperature and supercurrent, were carried out on the Nb film. The entry of flux bundles was detected in the magnetic field sweeps and coincidence measurements established that the flux bundle radius was temperature dependent. The temperature and current sweeps showed evidence of flux creep and enabled the measurement of pinning forces.

6.2. Nb Films

Niobium is unusual among the elemental superconductors in that it displays type II behaviour in bulk form. Because it is only just type II, the bulk material enters a curious state called the mixed-intermediate state, where regions of flux lattice are separated by flux-free regions. This comes about because the vortex interaction is attractive down to a minimum vortex spacing. Thus when vortices enter the material,

they approach to the minimum spacing, emptying the flux-free regions. This behaviour is not shared by thin Nb films which have an enhanced type II nature for the same reasons as the type II Pb films.

A Nb film of thickness 0.7μm was deposited onto a sapphire substrate by rf sputtering. Using a HF/HNO_3 etching solution, the film was patterned into a strip 3mm long and 100μm wide. Four gold wires were attached with silver epoxy to pads at either end of the strip, enabling the electrical properties of the film to be monitored. Difficulty was experienced in making low resistance contacts to the film. The substantial contact resistance (~18Ω) caused problems later on when large supercurrents were driven through the film. Heat dissipation at the contacts made it difficult to maintain stable temperatures in the film, and limited the maximum useful supercurrent.

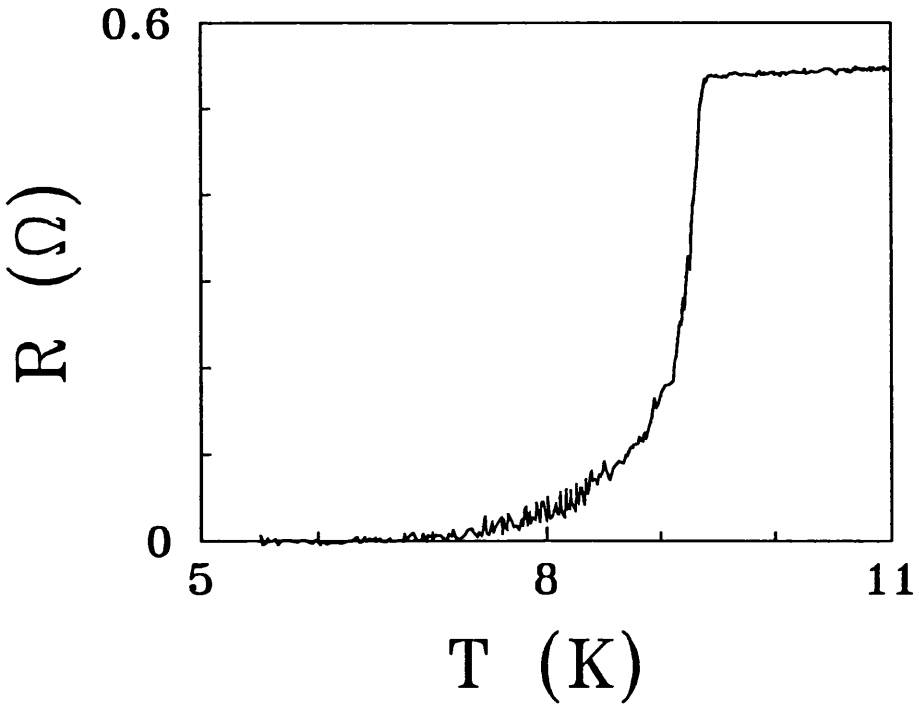

Figure 6.1. The resistance of the Nb film as a function of temperature.

The midpoint of the resistance measurement in Figure 6.1 confirmed that the 9.2K critical temperature of the film was the same as the bulk value. The long noisy tail

on the low temperature side of the transition is almost certainly due to the high resistance contacts. The film had a resistivity ratio $\rho(293K)/\rho(9.5K) \approx 35$. Following the procedure outlined in Chapter 5 for the Pb film, the critical field was found to be $\mu_0 H_{c2}(0) = 0.6 \pm 0.1 mT$ and the characteristic lengths were estimated as $\lambda(0) \approx 46nm$ and $\xi(0) \approx 24nm$.

6.3. The Hybrid Structure

The Hall probe design and assembly of the hybrid semiconductor/ superconductor structure was described in Chapter 4. Characterization of the 2DEG was complicated by the presence of parallel conduction, discussed in the following section. The 2DEG was at a depth of 36nm, with n_{2d} estimated to be $3.9 \times 10^{15} m^{-2}$ and $\mu \approx 23 m^2 V^{-1} s^{-1}$, ignoring the low mobility parallel conduction path. A Hall bar with a 2μm characteristic line width was employed.

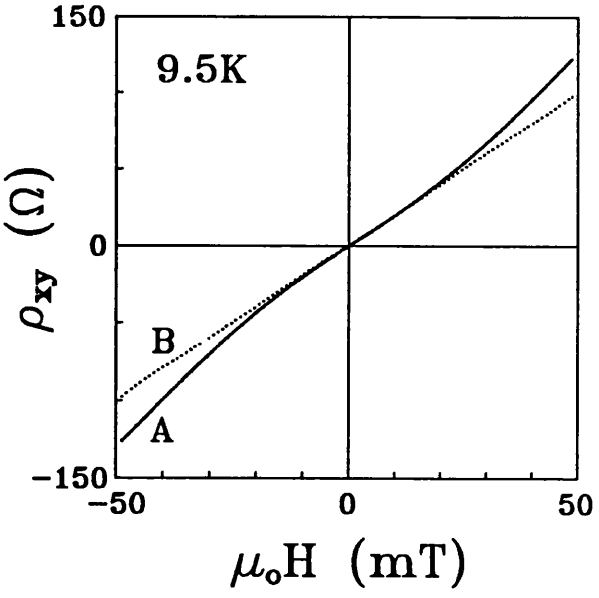

Figure 6.2. The Hall resistivity (ρ_{xy}) of the Nb-gated Hall bar at 9.5K when the Nb film is normal. The curvature of A is a sign of parallel conduction in the Hall bar. B is the improved linear response obtained from A after applying the correction procedure described in the text.

6.3.1. Parallel Conduction

When the Hall bar was cooled to 4.2K, some of the voltage leads were found to have an excessively high resistance. This problem was easily dealt with by a brief period of illumination with the infra-red LED which dramatically improves the 2DEG conductivity. When the 2DEG was subsequently characterized at 9.5K with the Nb film in its normal state, the Hall voltage was found to be non-linear in magnetic field, as illustrated in Figure 6.2. This is a sign that parallel conduction is taking place in the heterostructure, that is, there are two different sheets of conduction electrons of different electron densities and mobilities.

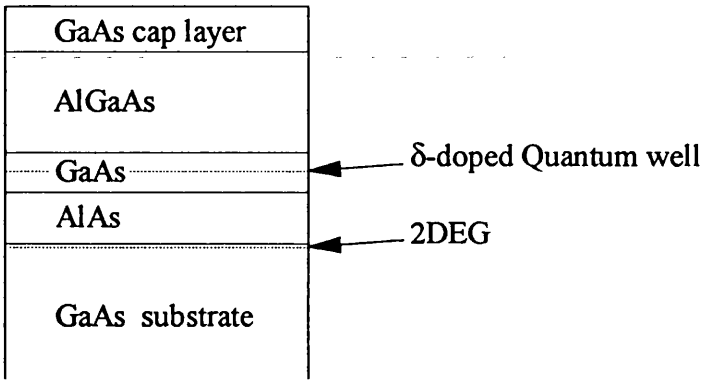

Figure 6.3. The layered heterostructure showing the intended location of the 2DEG. The parallel conduction path is probably in the quantum well.

The infra-red illumination increases the electron concentration in the 2DEG by persistent photoconductivity. In the conventional modulation-doped GaAs/$Al_xGa_{1-x}As$ heterostructure, parallel conduction can result[53] when the excited electrons form a parallel conduction path in the modulation-doped $Al_xGa_{1-x}As$ layer. As can be seen in Figure 6.3, the heterostructure used for the present Hall bar is different to the conventional structure, with the 2DEG forming at the GaAs/AlAs interface and with the donor atoms in the neighbouring GaAs quantum well. It is in the quantum well that the parallel conduction probably takes place. We make the reasonable assumption that

the electron mobility of the 2DEG at the GaAs/AlAs interface is much greater than that of the parallel conduction path.

In the low field limit[53], both components of the resistivity tensor are dominated by the high mobility conduction path :

$$\rho_{xx} \approx \frac{1}{n_{2d} e \mu}$$
$$\rho_{xy} \approx \frac{1}{n_{2d} e} B \qquad (6.1)$$

with both n_{2d} and μ referring to the high mobility 2DEG. The slope of the Hall resistivity at zero magnetic field was used to find n_{2d}. It was not possible to accurately determine the properties of the low mobility region because of the low magnetic fields available in the experimental apparatus, nor was this necessary because the aim of the experiments was to investigate the Nb film.

The fact that the Hall voltage is non-linear does not mean the Hall probe is useless as a magnetic field sensor. There is a linear region around the origin at the small magnetic fields (±15mT) used in the temperature and current sweeps. Larger magnetic fields were used for the hysteresis loops, and then the Hall resistivity was corrected to provide a linear response to magnetic field. The calibration of the Hall probe was carried out in the following way. At 9.5K with the Nb film in its normal state, there is negligible screening of the applied magnetic field so the measured Hall resistivity is produced by a known magnetic field. The properties of the Hall probe do not change significantly over the 4.5K to 9.5K temperature range of the measurements, enabling $\rho_{xy}(B)$ at 9.5K to be used to calibrate the sensor at other temperatures. Considering the applied flux density B to be a function of the measured Hall resistivity, the curve in Figure 6.2 can be accurately fitted to a fifth order polynomial:

$$B(\rho_{xy}) = c_5 \rho_{xy}^5 + \ldots + c_1 \rho_{xy} + c_0 \qquad (6.2)$$

where the coefficients c_i were found from a least-squares fit. Thus given a measured Hall resistivity ρ_{xy}, the corresponding magnetic field B can be calculated using Equation (6.2). A corrected Hall resistivity ρ'_{xy} is readily obtained :

$$\rho'_{xy} = \frac{1}{n_{2d}e} B(\rho_{xy}) \qquad (6.3)$$

where the electron concentration n_{2d} is the value obtained from the zero field slope. The effectiveness of this procedure is demonstrated in Figure 6.2 where the corrected linear Hall resistivity is also plotted.

6.4. Results and Discussion

6.4.1. Magnetic Field Sweeps

Magnetic field sweeps were carried out after the Nb film had been cooled from above T_c in zero applied magnetic field so that each sweep could start from the same initial equilibrium state. A series of hysteresis loops at different temperatures from 4.5K to 9.5K are displayed in Figure 6.4. The hysteresis loops are similar in appearance to those obtained with the 2μm Pb-gated structures, with the same discontinuous steps resulting from the entry of flux bundles observed below T_c. The detailed structure of the curves is not repeatable, that is the size and position of the steps varies for loops recorded under the same conditions on consecutive thermal cycles. The first penetration of flux to the centre of the Nb strip takes place at much higher applied fields than was the case for the Pb films. The most likely reason is the greater width of the Nb strip, which overcomes the compensating effect of weaker flux pinning forces (measured later). With increasing temperature, pinning forces decrease and the hysteresis loops become narrower. The 8.5K loop appears to close up entirely at the larger applied fields, but some hysteresis is still revealed on closer inspection.

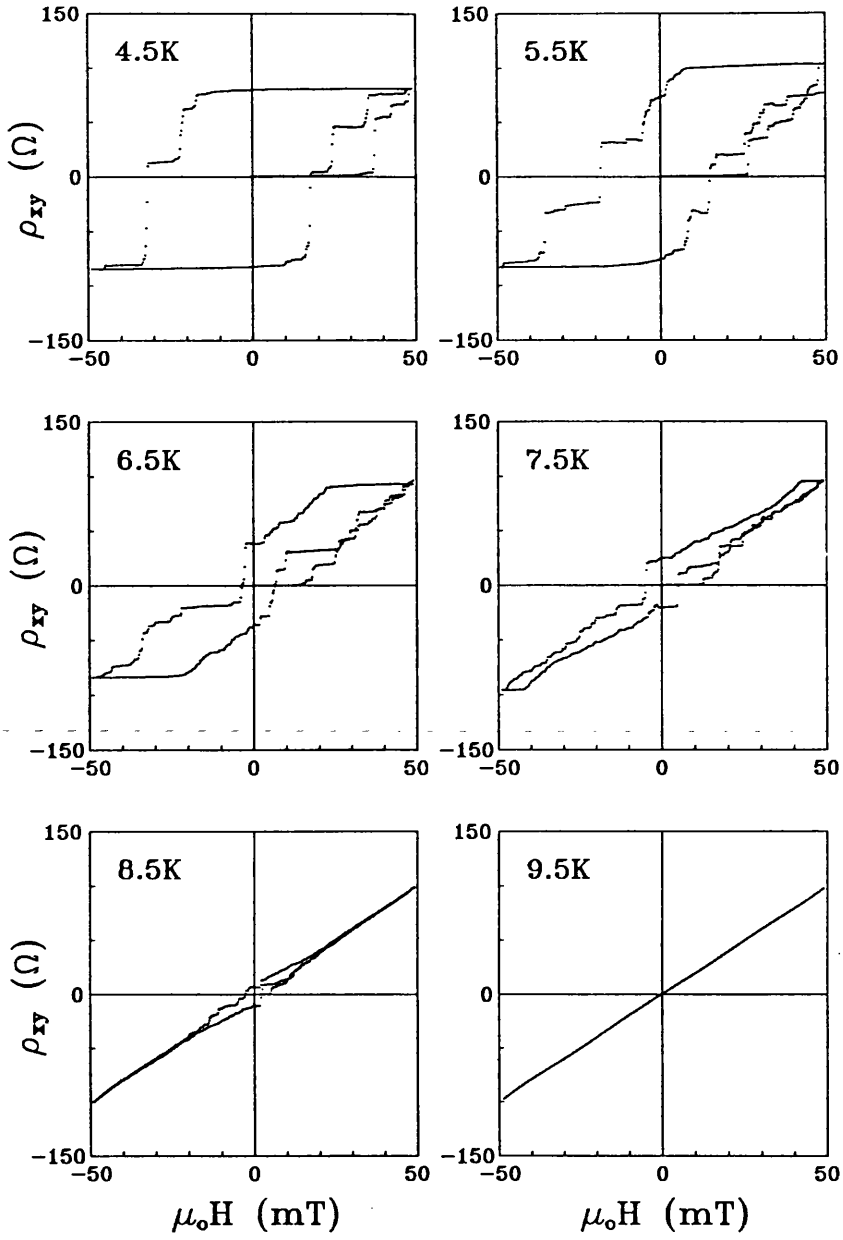

Figure 6.4. Corrected Hall resistivity (ρ_{xy}) of the Nb-gated Hall bar at different temperatures.

It was again possible to observe correlated steps in pairs of hysteresis loops recorded simultaneously at different Hall probes. The correlation coefficient c was determined for pairs of hysteresis loops using the same procedure devised for the Pb film. Some of the results are plotted in Figure 6.5. c was found to decrease both with increasing contact separation and increasing temperature. Fitting the data using the model outlined in Chapter 5 provided the values of the flux bundle correlation radius r_0 tabulated below.

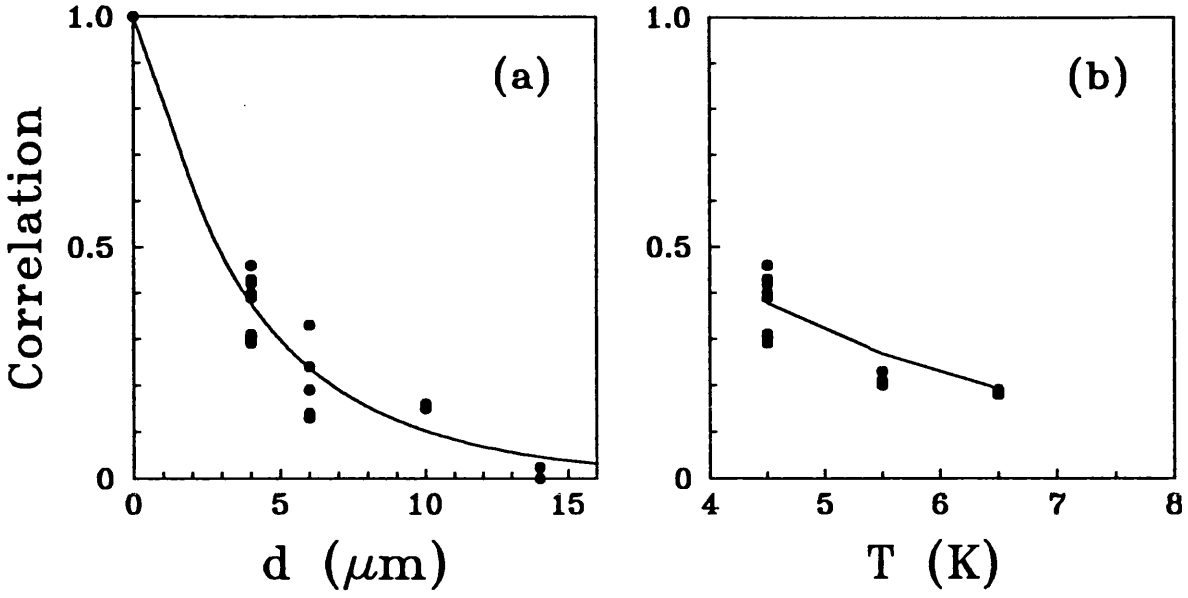

Figure 6.5 (a) The correlation c measured at different separations at 4.5K. The solid curve is a fit using a flux bundle radius $r_0 = 3.4\mu m$. (b) The correlation measured at different temperatures for contacts 4μm apart. The solid line joins points calculated using the values of r_0 listed in Table 6.1.

T(K)	r_0 (μm)
4.5	3.4±0.2
5.5	2.2
6.5	1.6

Table 6.1. Flux bundle radius r_0 at different temperatures.

Thus r_0 in the Nb strip decreases as temperature increases, in contrast to the temperature independence found in the Pb film. Recalling the theoretical estimate of the collective pinning correlation radius due to Larkin and Ovchinnikov[24], $R_c = \frac{C_{66}\, a}{f_p \sqrt{n_p}}$, the only temperature dependent terms are the shear modulus C_{66} and the pinning force f_p. The temperature dependence of the shear modulus can be obtained

from an expression due to Larkin[25] : $C_{66} \propto \lambda^{-4}\sqrt{\lambda/a}\exp(-a/\lambda)$. Using the Ginzburg-Landau temperature dependence $\lambda(t) = \lambda(0)(1-t)^{-1/2}$, we find that

$$C_{66}(t) \propto (1-t)^{1.75}\exp(-a/\lambda). \qquad (6.4)$$

The flux lattice constant $a \approx \sqrt{\Phi_0/B}$, so we can simplify matters by choosing a value of B large enough for the first term of the expansion $\exp(-a/\lambda) = 1 - a/\lambda + \ldots$ to dominate, that is $C_{66}(t) \propto (1-t)^{1.75}$.

In the Pb film we found that $f_p(t) \propto (1-t)^n$, with $n = 1.5-2$ depending on the particular site examined. A flux bundle must sample many pinning sites, so it seems likely that C_{66}/f_p will have a weak temperature dependence. For the Nb film, anticipating the result given later in this chapter that $f_p(t) \propto (1-t)^{0.52}$, we have $C_{66}/f_p \propto (1-t)^{1.2}$. In both cases, there is reasonable agreement between the measured trend in r_0 and the temperature dependence of R_c obtained using the Larkin-Ovchinnikov theory. The exact dependence of r_0 on temperature should not be expected to be exactly the same as that of R_c because r_0 is measured over a range of magnetic fields while R_c is calculated at a fixed value of B.

The separation of the 2DEG and superconductor was already believed to be of the order of one micron from the observation of optical interference fringes through the transparent substrate. The slope of the initial portion of the hysteresis loops was used to provide a more quantitative estimate. The slope was measured from 0 to 20mT on the first leg of the 4.5K hysteresis loops. Applying the relationship $z_0 = W\dfrac{H(z_0)}{H_a}$, with W the half-width of the Nb strip, the separation of Hall probe and superconductor was found to be $z_0 = 0.52 \pm 0.05\mu m$. Considering that the 2DEG is at a depth of approximately 40nm and the Nb film is 700nm thick, the value for z_0 implies that the thickness of the adhesive layer is about 130nm.

6.4.2. Temperature Sweeps

Temperature sweeps were carried out on the field-cooled Nb film, with results that on the whole were consistent with those obtained from the Pb films. As well as the Hall voltage, the resistance of the Nb film was simultaneously measured with a small 10μA measurement current, allowing the film resistance to be compared with flux movements detected during the temperature sweep. The current density in the superconductor was small enough to have no noticeable effect on the flux structures.

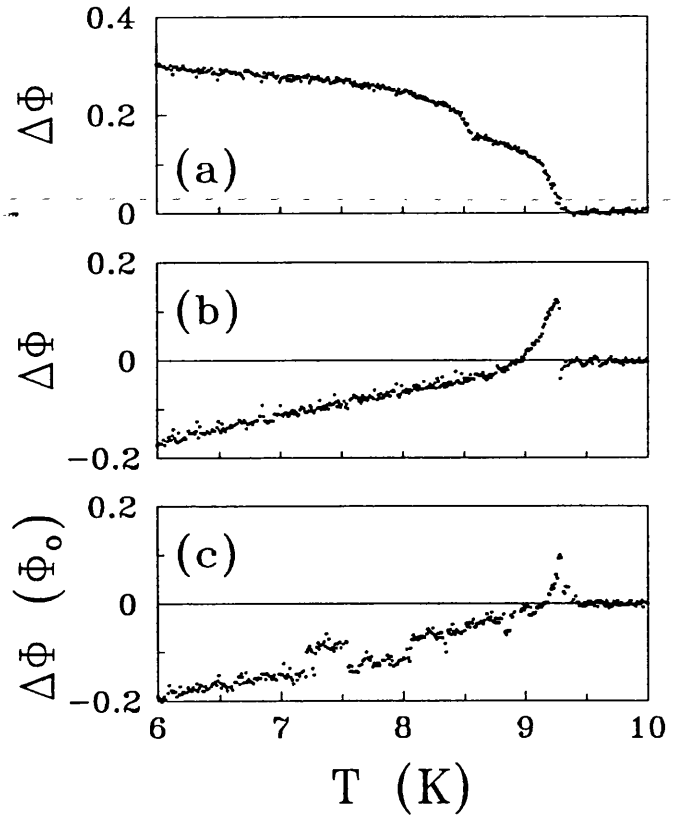

Figure 6.6. (a) The change in flux (ΔΦ) threading a Hall probe as a function of temperature at an applied field of 0.5mT. (b) and (c) The same measurement performed at a different Hall probe in applied fields of 0.5mT and 1mT respectively.

Some temperature sweeps taken with an average of one or two flux vortices in the active area of the probe are shown in Figure 6.6. Gradual flux motion commences well below T_c and continues right up to the transition. In Figure 6.6(a), it appears as if the vortex under observation moves gradually from one pinning site to another. A

temperature sweep at a different contact shows in Figure 6.6(b) a sudden collapse of the flux arrangement to the uniform normal state distribution at T_c. At this same contact, when the number of vortices present is increased from one to two, a vortex is observed to hop between two different positions (Figure 6.6(c)). The observed mixture of slow shifts and abrupt jumps is consistent with observations of vortices in a Nb foil made by Lorentz microscopy[51].

Unlike the very sharp resistive transition observed in the Pb film, the transition in the Nb film is broader with the midpoint of the transition at 9.2K and the full normal state resistance only reached at 9.4K. The flux movement observed in the temperature sweeps ceases not at the transition midpoint, but at 9.4K when the sample is completely normal. In common with the Pb film, when the Nb was field cooled, the vortices did not always settle into the same configuration, but chose an alternative configuration about 10% of the time.

With a larger applied magnetic field, vortex interactions become more important. Although not as dramatic as the interaction-driven steps seen in the Pb film, there was some evidence of vortices hopping between different configurations below T_c which may be seen in Figure 6.7 for a 10mT applied flux density.

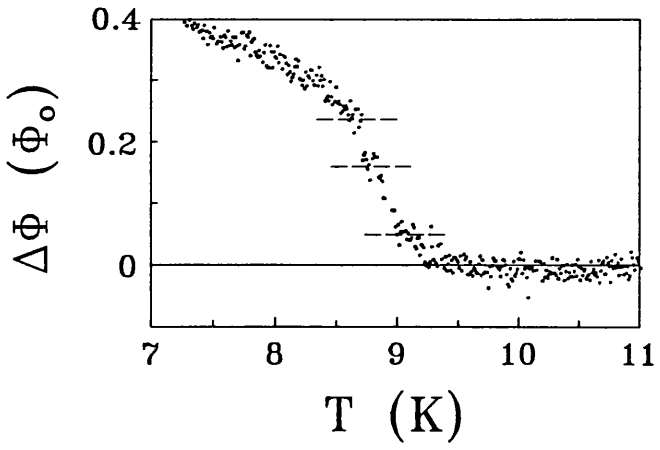

Figure 6.7. The change in flux ($\Delta\Phi$) threading a Hall probe as a function of temperature at an applied field of 10mT.

Temperature sweeps were also made with more substantial currents passing through the superconductor. The greatest current density applied was $1.4 \times 10^4 \text{A cm}^{-2}$, approximately 50 times smaller than the current densities applied to the Pb films. Higher current densities could not be applied because joule heating in the high resistance contacts became sufficient to upset the temperature stability of the film. The temperature sweeps with the applied supercurrent did not show the same evidence for flux creep seen in the Pb films, presumably because the small current densities restricted the flux creep regime to a narrow range of temperatures just below T_c.

6.4.3. Current Sweeps

After being field cooled with zero applied supercurrent, the film was held at a fixed temperature while the supercurrent was slowly increased. The Hall voltage was measured and the resistance of the Nb film was monitored at the same time. The maximum supercurrent density in the film was restricted by the need to maintain a stable temperature. As it was, the extra variable heat input contributed by joule heating in the contacts reduced temperature stability to $\pm 10\text{mK}$.

Another unwelcome consequence of the contact resistance is a gating effect caused by a voltage drop in the contacts. When a supercurrent is driven through the film, there is a potential difference between the Nb film and the 2DEG which changes the electron concentration and hence the Hall coefficient of the 2DEG. During a current sweep, the change in potential is proportional to the applied current and the result is a linear addition to the Hall voltage. Gating effects were not observed in the Pb films because they had both low film resistance and low contact resistance. The YBCO film examined in the next chapter has low contact resistance but a relatively high normal state resistance. No gating effects were observed with the YBCO film in its superconducting state but there were dramatic changes in Hall voltage at the superconducting transition as the normal state resistance sets in.

The background slope contributed by the gating effect has been removed in the same way as the background slope was removed from the temperature sweeps, using the slope of the normal state identified as the featureless straight line at the end of the current sweep. The background slope is the same when the film is superconducting, as could be seen in current sweeps made well below T_c where there is no flux motion added to the measured Hall voltage. Current sweeps taken over a range of temperatures close to T_c are plotted in Figure 6.8. The applied flux density was 0.5mT, so there was just one vortex on average in the active area of the Hall probe.

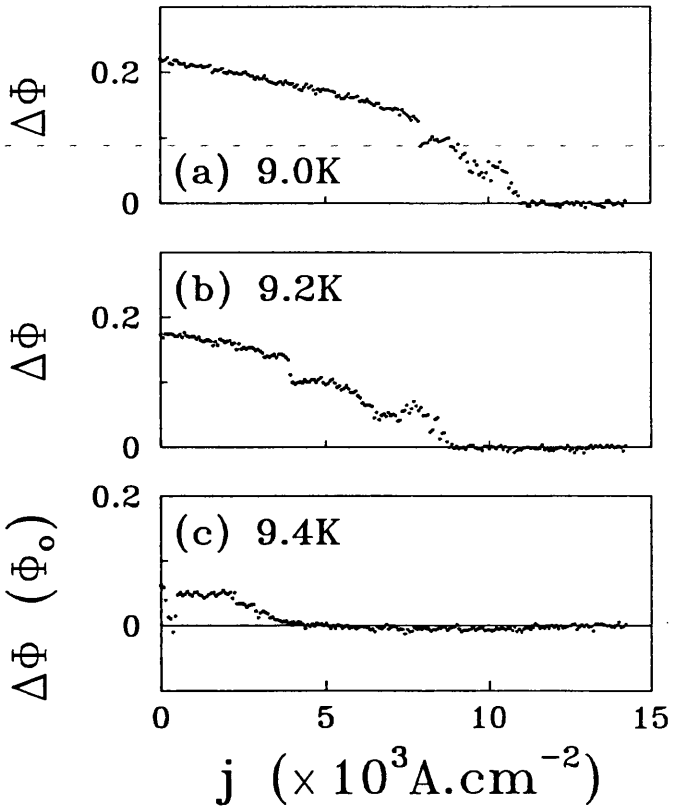

Figure 6.8. (a)-(c) The change in flux ($\Delta\Phi$) threading a Hall probe as a function of current density in the Nb film at various temperatures in a 0.5mT applied field.

In common with the Pb films, there is a discontinuous step at a threshold current, indicating the onset of flux creep. This is preceded by a continuous change in Hall voltage, suggesting a smooth vortex movement not observed in the Pb film. It seems that the Lorentz force causes a continuous shift of the flux vortex until a point

where the vortex hops into a different site. A 'noisy' section of curve follows, corresponding to the flux creep regime, although this is not as distinct as in the Pb film. The most probable reason is that the smaller supercurrent density in the Nb film confines the flux creep regime to a narrow current range close to the transition to the normal state. The noise due to the flux creep dies down just before the film is driven normal by the supercurrent. With temperature increasing from Figure 6.8(a) to (c), the flux creep regime is observed at lower current densities, until at 9.4K flux creep starts as soon as a current is applied and quickly gives way to the normal state.

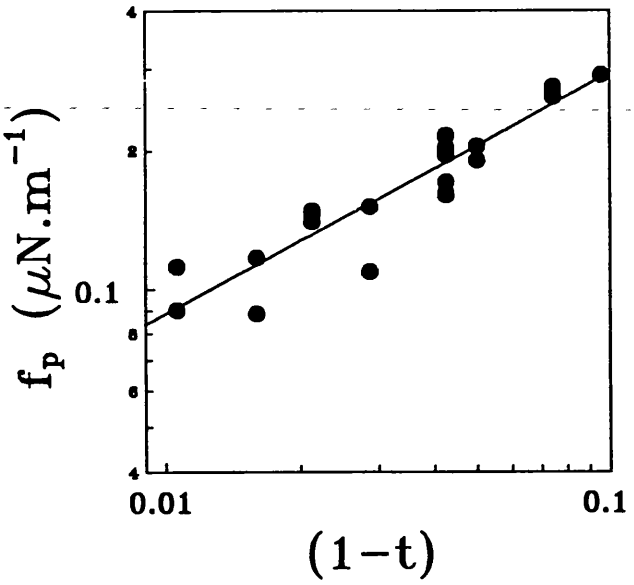

Figure 6.9. Pinning force in the Nb film plotted as a function of (1-*t*). The straight line is a fit to an empirical form (see text).

At the onset of flux creep, the Lorentz force exerted on the vortex under observation is equal to the pinning force. Assuming a uniform distribution of supercurrent in the film, the Lorentz force per unit length is $\mathbf{f}_L = \mathbf{j} \times \Phi_0$. Using this relation, the pinning force per unit length f_p was obtained from the supercurrent density at the onset of flux creep at four different Hall probes, that is from four different positions in the Nb film, and was plotted in Figure 6.9. The pinning forces at the different pinning sites were all the same magnitude and showed the same temperature

dependence, unlike the variations observed in the Pb film. The pinning force vanishes at 9.4K, the temperature at which all traces of superconductivity disappear, so 9.4K was used to determine the reduced temperature t. The data in Figure 6.9 was fitted to the empirical form $f_p(t) = f_p(0)(1-t)^n$ with $n = 0.52 \pm 0.05$ and $f_p(0) = 1.0 \pm 0.1 \mu Nm^{-1}$. The value for n is considerably smaller than those found for the Pb films in Chapter 5 and values for Nb films given by other authors. Park *et al.*[7] found $n = 1.9$ for a thin 20nm film with $T_c = 7.35K$. Allen and Claassen[54] found $n = 3.5$ also for a film 20nm thick with $T_c = 8.91K$. With such a wide variation in the critical exponent n, it is clear that the particular value measured is strongly dependent on the preparation of film and its superconducting properties.

Chapter 7

$YBa_2Cu_3O_{7-\delta}$ Films

7.1. Introduction

The Nb measurements demonstrated that the Hall probes could achieve single vortex resolution with films deposited on separate substrates. The techniques developed with the Nb film were then applied to the high-temperature superconductor $YBa_2Cu_3O_{7-\delta}$ (YBCO). A few initial magnetic field sweeps were made with the YBCO film unsuitably positioned, and these are included to show the importance of minimizing the probe/film separation, an aspect neglected in many previous Hall probe studies. Once the separation had been optimized, a series of magnetic, temperature and supercurrent investigations were carried out using a 2μm Hall bar. The results are contrasted with those for the conventional Pb and Nb films where appropriate.

The hysteresis loops could be described by the critical state model[28, 30] introduced in Chapter 2, with the critical current as the only fitting parameter. Flux bundles were not observed and a differential technique employed to provide greater resolution suggested that vortices entered one by one. The cross-over from flux creep to flux flow was observed in the temperature and current sweeps, which also allowed the measurement of pinning forces.

7.2. $YBa_2Cu_3O_{7-\delta}$ Films

The epitaxial YBCO film was grown to a thickness of 0.35μm on a MgO substrate by co-evaporation. It was patterned into a strip 200μm wide and 6mm long,

with low resistance silver contact pads at either end permitting four-point resistance measurements. The resistance of the film across the superconducting transition is plotted in Figure 7.1. The width of the transition is about 10K, with the critical temperature of 82K taken from the midpoint. The excessive transition width and the kink in the middle are indications of macroscopic inhomogeneities along the strip, with different regions having slightly different critical temperatures. Immediately after growth and annealing in oxygen, T_c was found to be 89.7K from magnetization measurements. The subsequent drop in T_c was probably due to changes when the strip was patterned or in storage. The penetration depth in similar films has been reported[55] as 200nm with a temperature dependence $\lambda(T) = \lambda(0)(1-t^2)^{1/2}$.

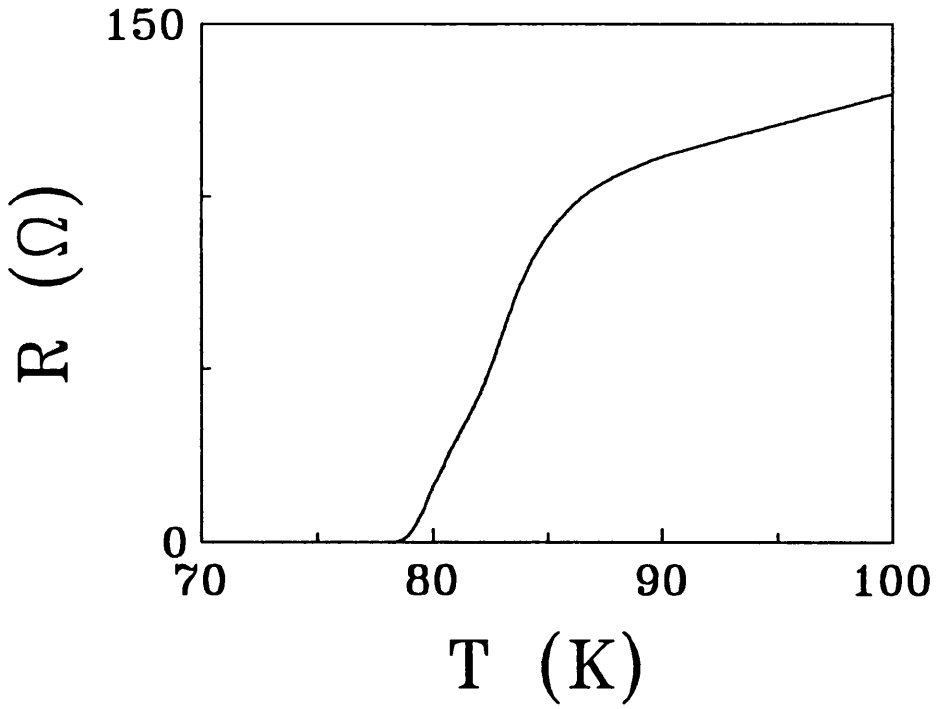

Figure 7.1. The resistance of the YBCO film as a function of temperature.

7.3. The Hybrid Structure

The Hall bar was fabricated with a 2μm characteristic linewidth and long voltage and current leads to stretch out from under the YBCO film and substrate. A

conventional modulation-doped GaAs/$Al_xGa_{1-x}As$ heterostructure was used, with the 2DEG at a depth of 300nm. The electron concentration $n_{2d} = 1.3 \times 10^{15} m^{-2}$ changed by approximately 5% over the wide temperature range of the measurements, while the mobility decreased from $86 m^2 V^{-1} s^{-1}$ at 4.5K to $13 m^2 V^{-1} s^{-1}$ at 85K.

The same Hall bar and YBCO film were examined in two configurations. In the first, the MgO substrate bearing the superconductor was placed on top of the Hall probe and held in position with GE varnish around the perimeter. The separation was found to be small, but not small enough for single vortex resolution. Subsequently the GE varnish was dissolved with an organic solvent and the substrate glued down with a film of dilute GE varnish following the procedure described in Chapter 4. The observation of optical interference fringes in the layer of varnish between the Hall probe and substrate suggested a much smaller spacing and this was confirmed by the magnetic measurements.

7.4. Results and Discussion

7.4.1. Magnetic Field Sweeps

Hysteresis loops were measured over a wide range of temperatures for both Hall probe/superconductor configurations. Hysteresis loops for the wide separation are shown in Figure 7.2 at a variety of temperatures. The large gradient of the initial portion of the loop as the applied magnetic field is increased from zero is a sure sign that the Hall probe is an undesirable distance away from the YBCO film. The gradient of the initial linear region was determined from hysteresis loops at temperatures from 4.5K to 30K. Using the relation $z_0 = W \frac{H(z_0)}{H_a}$ with W the half-width of the YBCO film, the separation between Hall probe and film was found to be $z_0 = 15 \pm 1 \mu m$.

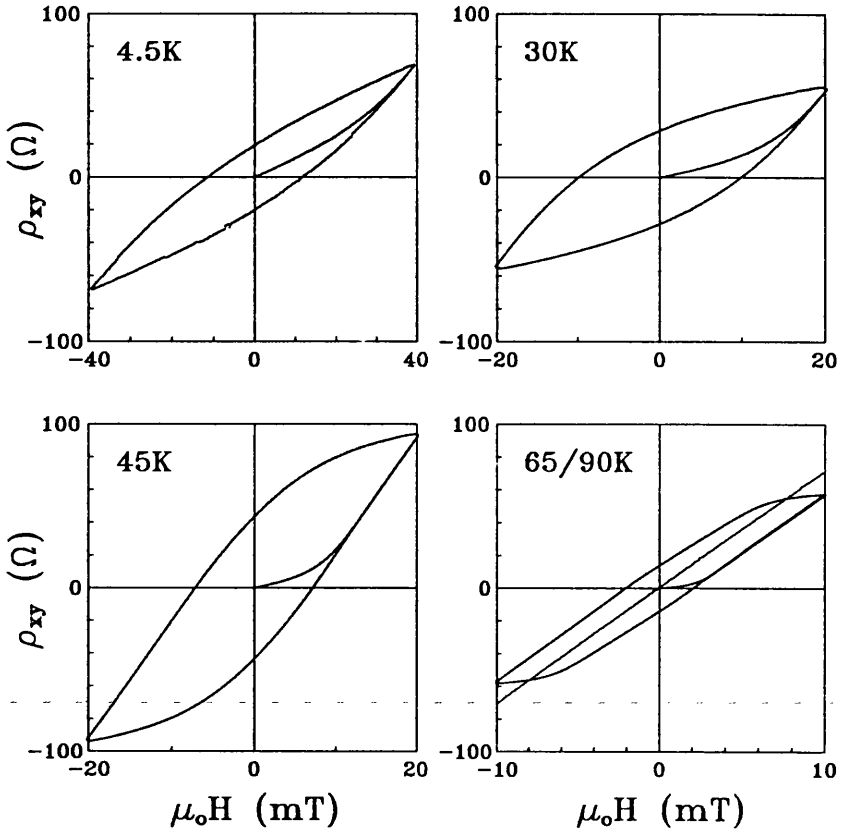

Figure 7.2. The Hall resistivity (ρ_{xy}) of the YBCO-gated Hall bar at different temperatures. The separation between superconductor and Hall probe is large.

The graphs in Figure 7.2 are not of great interest in themselves, but present a cautionary example when compared with the hysteresis loops in Figure 7.3 which were recorded with the same Hall probe and superconductor, but with the spacing greatly reduced. These hysteresis loops clearly give a much more accurate account of the magnetic field penetrating the YBCO film. The overall shape of the loops is quite different, with shoulders appearing when flux begins to enter or leave the film which are absent from the loops in Figure 7.2. The initial portion of the loop is now much flatter, only lifting off from the *x*-axis when magnetic flux penetrates to the centre of the strip. The initial slope showed that the probe/superconductor spacing had been reduced to 1.5±0.4μm. Taking into account the thickness of the YBCO film and the depth of the 2DEG, this implies that the adhesive layer is about 1μm thick.

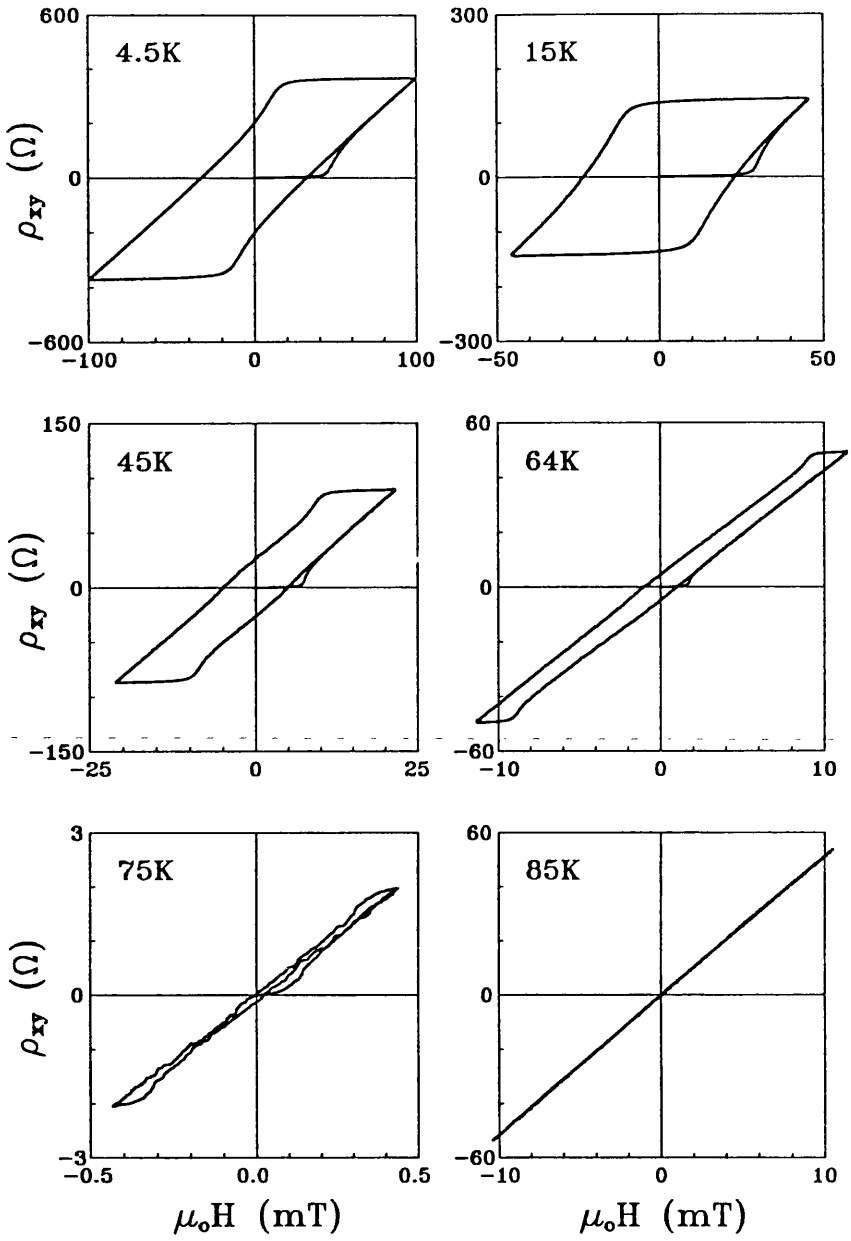

Figure 7.3. The Hall resistivity (ρ_{xy}) of the YBCO-gated Hall bar at different temperatures. The separation between superconductor and Hall probe is small.

The Hall probe is sufficiently close to the superconductor for the Hall resistivity to be an accurate measure of the local magnetic flux density B over a $2\times 2\mu m^2$ area of the superconducting film. It is thus possible to define a local magnetization $M_L = \frac{1}{\mu_0} B - H$ where B is the measured flux density obtained from ρ_{xy} and H is the external applied field. Figure 7.4 shows the local magnetization M_L at the centre of the

film as the applied magnetic field is cycled around a hysteresis loop, computed using the 4.5K hysteresis loop in Figure 7.3.

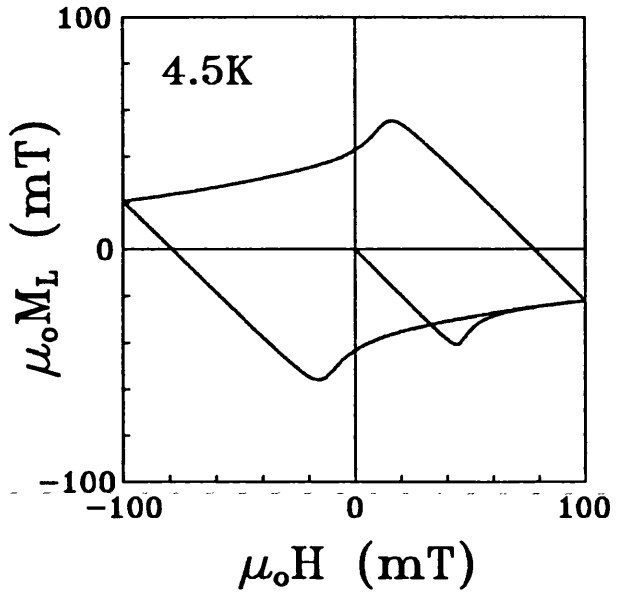

Figure 7.4. The local magnetization M_L at the centre of the YBCO film.

As the superconductor becomes warmer, the magnetic field at which the initial flux penetration occurs decreases, as does the width of the loop. At 75K the width of the hysteresis loop is very small, and if it were not for the persistence of the shoulders, the measurement would show little evidence of superconductivity.

The width of a hysteresis loop depends on the critical current of the superconducting film. The thin film critical state model[28, 30] introduced in Chapter 2 provides in Equation (2.28) the distribution of the perpendicular component of the magnetic field $H(y)$ across the width of the superconducting strip. Assuming that the Hall probe is perfectly positioned in the centre of the strip, it will sense an average magnetic flux density given by

$$B(H_a, J_c) = \frac{\mu_0}{w} \int_{-w/2}^{+w/2} H(y, H_a, J_c)\, dy \qquad (7.1)$$

where H_a is the applied magnetic field and J_c is the critical current integrated over the film thickness. w is the width of the active area of the Hall probe, in this case 2μm. $H(y)$ is history-dependent, depending on the maximum applied field $+H_0$ reached on the first leg of the hysteresis loop. The measured Hall resistivity could be compared with the model by converting ρ_{xy} into magnetic flux density $B = \rho_{xy}/R_H$ using the known electron concentration. The 4.5K hysteresis loop is plotted in Figure 7.5 together with $B(H_a, J_c)$ fitted to the experimental data with the single fitting parameter J_c.

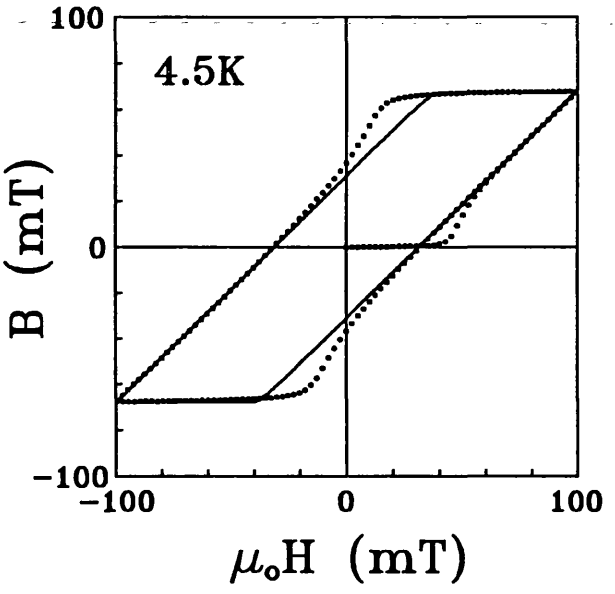

Figure 7.5. A fit of the critical state model (solid line) to the 4.5K hysteresis loop (dotted line).

The data is well described by the model except for the 'shoulders' where flux enters or exits the centre of the film. The model assumes that J_c is independent of the applied magnetic field, and the quality of the fit shows that the assumption is good for the low magnetic fields applied in this work. Each hysteresis loop in Figure 7.3 was fitted to the model and the resulting critical current densities j_c are plotted in Figure 7.6. j_c was obtained under the assumption that J_c was uniformly distributed across the

thickness d of the superconducting film. The film thickness of 0.35μm is less than twice the penetration length so the screening currents will flow approximately uniformly over the entire film thickness. From the figure, the critical current appears to decrease exponentially at low temperatures with a different temperature dependence close to T_c.

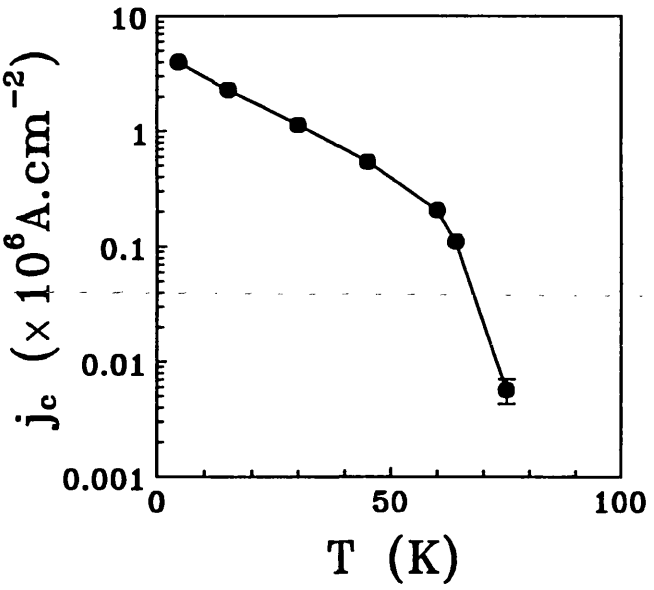

Figure 7.6. The critical current density in the YBCO film obtained by fitting the critical state model to the hysteresis loops in Figure 7.3.

The critical state model only considers the effect of bulk pinning, so the discrepancy between the model and the 'shoulders' on the hysteresis loop suggests that there is an additional mechanism influencing flux entry and exit. Recently a geometrical barrier has been proposed to explain the penetration of flux into a flat BSCCO crystal in a perpendicular magnetic field[56]. The geometrical barrier arises from a consideration of the potential energy of a flux vortex in a superconducting strip of rectangular cross-section, taking into account the effect of the square edges and the interaction between the vortex and the Meissner screening currents. Zeldov *et al.*[56] find that there is a potential barrier that delays the entry of flux vortices even in the absence of bulk pinning, and that when the vortices do enter, they are driven to the centre of the strip

by the screening currents. This qualitatively explains the shoulder observed on the initial upward sweep of the hysteresis loop. When the magnetic field is reduced, the screening currents prevent the vortices from leaving the centre immediately, accounting for the shoulders on the last two legs of the hysteresis loop.

All of the Pb and Nb hysteresis loops recorded using the 2μm Hall probes showed discrete flux jumps which are beyond the scope of the critical state model. An attempt was made to fit the smooth loops measured with the 10μm Hall bars on the Pb films, but the model could not provide hysteresis loops of the right shape. Possible explanations are that the width of the Hall bar at 10μm is significant in comparison to the 20μm wide Pb film, resulting in the Hall bar detecting too much of the fringing magnetic field; that the flux penetration was complicated by the granular structure of the Pb film; that there are effects due to the field-dependence of j_c because the largest applied magnetic fields around the loop reach an appreciable fraction of H_{c2}.

So far we have ignored a striking feature of the hysteresis loops in Figure 7.3 - there is no evidence for the existence of flux bundles. Unlike the Pb and Nb hysteresis loops, the YBCO loops show no discontinuities or steps caused by the sudden entry of flux bundles into the centre of the film. Although strong multi-vortex discontinuities are absent, there is nevertheless some weak structure due to the entry of single flux vortices which can be seen by magnifying the Hall resistivity sufficiently. The required signal is a small part of a large and rapidly changing Hall voltage and it was extracted by using a differential amplifier to subtract the output of one Hall probe from that of a neighbour. The simple circuit used is illustrated in Figure 7.7. The differential measurement gives an expanded view of the Hall voltage by removing the large background and allowing the application of more gain to the remaining signal, with the results shown in Figure 7.8.

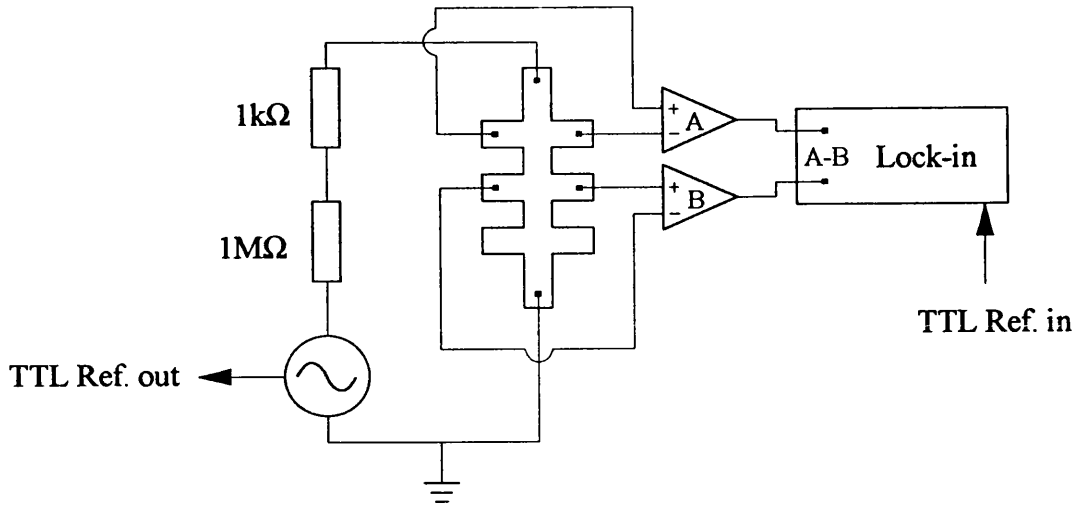

Figure 7.7. The circuit used to measure the difference between two Hall voltages. The amplifiers A and B are high-input-impedance differential amplifiers that supply the two Hall voltages to the differential mode inputs of the lock-in amplifier.

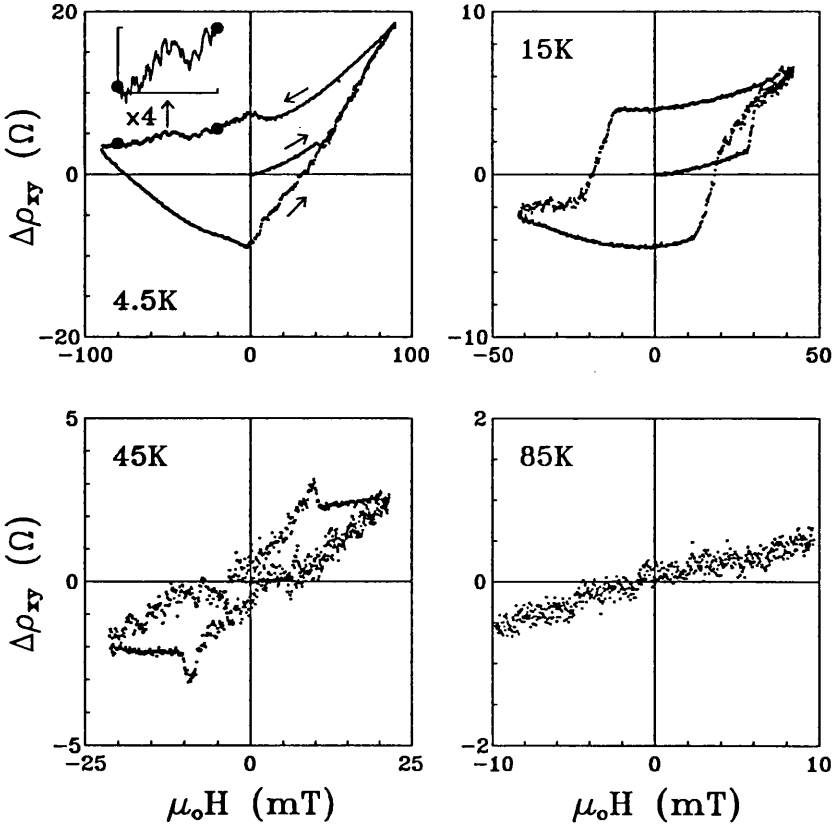

Figure 7.8. Differential hysteresis loops measured at different temperatures. The arrows show the direction of magnetic field sweep. A section of the 4.5K hysteresis loop is magnified in the inset to show greater detail.

The differential signals $\Delta\rho_{xy}$ are composed of two contrasting sections and should be looked at in conjunction with the hysteresis loops in Figure 7.3. The smoother sections correspond to sections of the hysteresis loop where the Hall resistivity changes only slightly, where flux pinning is preventing the entry or exit of flux vortices from the centre of the YBCO film. The remaining sections of the differential loops display clear structure and correspond to regions of the hysteresis loop which show large changes in Hall resistivity. The overall shape of the $\Delta\rho_{xy}$ curves is not believed to be significant as it reflects imperfect cancellation of the background Hall voltage for reasons such as differences in the local flux density at the two probes due to inhomogeneities in the film, differences in probe sensitivity caused by small variations in n_{2d} from probe to probe, and inequalities in the gain of the two differential amplifier channels.

While the overall shape of the $\Delta\rho_{xy}$ curve remained the same from sweep to sweep, the fine structure was not repeatable. The fine structure magnified in the inset to the 4.5K differential loop surprisingly does not take the form of discrete jumps but has a sawtooth form with an amplitude equivalent to changes in threaded flux of approximately $0.2\Phi_0$. The amplitude of the sawtooth is very similar to the changes in threaded flux observed in the Pb and Nb films at low applied magnetic fields when a single flux vortex moves under the influence of changing temperature or supercurrent. This suggests a picture of single vortices entering the centre of the YBCO film moving gradually through a very high density of pinning centres. The differential loops show the same behaviour up to 65K, but the traces at 75K are just about indistinguishable from those at temperatures above T_c. When the film enters the normal state, the differential signal is a straight line as both Hall probes produce the linear Hall voltage characteristic of the normal state. Note that the noise in the differential signal does not change significantly over the temperature range of the measurements - the noise level at 85K is very similar to that in the smooth sections of the 4.5K graph. The noise level appears to increase because the vertical scale changes from plot to plot.

One drawback of the differential measurement is that subtracting the two Hall voltages mixes together the signals from the two probes. However a consequence of this is that the fluctuations in $\Delta\rho_{xy}$ will become smaller if there is any correlation in the Hall voltages from the two probes. Differential measurements performed on pairs of Hall probes with separations ranging from 4μm to 16μm revealed no discernible difference in the fine structure of $\Delta\rho_{xy}$. Thus it appears that flux enters the centre of the YBCO film as individual vortices in an uncorrelated fashion consistent with a high density of pinning sites. In Reference 57, the high critical current densities and pinning energies observed in thin YBCO films have been explained by a model based on pinning at a high density of local defects in the CuO planes. England *et al.*[58] have measured critical currents in YBCO films and concluded that dissipation only occurs through the movement of flux bundles in magnetic fields above 2T. At low magnetic fields, they attributed dissipation to motion of individual flux quanta.

7.4.2. Temperature Sweeps

Temperature sweeps were carried out from 68K upwards, at temperatures accessible with liquid nitrogen. The film was always field-cooled to provide an equilibrium arrangement of flux. The resistance of the YBCO film was monitored during the sweep with the application of a supercurrent that was too small to affect the flux vortices. No definite features were observed in the Hall voltage as the film temperature was increased through T_c. The superconducting transition is about 10K in width, so flux movements caused by warming will be gradual and difficult to detect because the Hall voltage offset is changing as well. With the sweeps extending over a broad temperature range, the offset drift was no longer linear and could not be removed with sufficient confidence.

Although no significant features were observed in temperature sweeps recorded with zero supercurrent density, the sweeps became more interesting when a large dc supercurrent was driven through the YBCO strip as can be seen in Figure 7.9. Both

sweeps were recorded in an applied flux density of 0.5mT and the supercurrent density was 0.7 and 1.4×10^5 A cm^{-2} in Figures 7.9(a) and (b) respectively. Initially the curves are flat with little sign of flux movement until there is a sudden drop in the flux threading the Hall probe. All probes showed the same change in threaded flux which probably marks the entry of additional flux associated with the applied supercurrent. Brandt and Indenbom[29] have calculated the current distribution in a type II superconducting strip carrying a supercurrent in a perpendicular magnetic field. For $j < j_c$ the supercurrent flows mostly at the strip edges, encroaching on the centre of the strip as j approaches j_c. The perpendicular component of the magnetic field associated with the supercurrent distribution moves in towards the centre of the strip in the same way, with its sign depending on the exact location of the Hall probe relative to the strip centre. The decrease in threaded flux observed in Figure 7.9 occurs at lower temperatures and becomes larger in magnitude as the applied supercurrent increases, both observations being consistent with Reference 29.

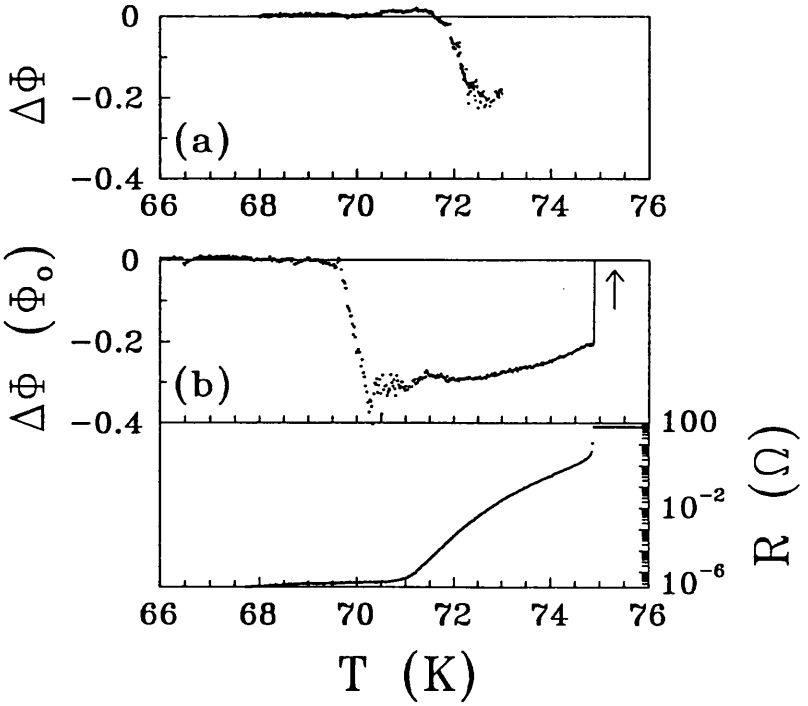

Figure 7.9. (a) The change in flux ($\Delta\Phi$) threading a Hall probe as a function of temperature at an applied field of 0.5mT. The supercurrent density in the YBCO film is 0.7×10^5 A cm^{-2}. (b) The supercurrent density is now 1.4×10^5 A cm^{-2}. The flux flow resistance (R) of the YBCO film is plotted below the change in flux ($\Delta\Phi$).

The large decrease in threaded flux coincides with a clear increase in the level of noise in the Hall voltage, a sign of the onset of flux creep. Looking at the resistance of the YBCO film measured simultaneously with the temperature sweep in Figure 7.9(b), there is still no measurable flux flow voltage at this temperature. As temperature increases and pinning forces decrease further, the flux creep becomes more rapid and only after 71K is there a detectable flux flow resistance. At the same time, the Hall voltage noise tails off because the fluctuations caused by flux vortices moving across the active area of the probe become too rapid to be resolved by the lock-in amplifier with its 100ms time constant. Once there is a flux flow resistance in the film, the voltage drop along the film produces a gating effect and the Hall voltage steadily increases in proportion to the resistance, eventually going off-scale when the YBCO film is driven normal by the supercurrent. The film enters the normal state extremely rapidly, probably as a result of thermal runaway.

7.4.3. Current Sweeps

The YBCO film was field-cooled in a constant magnetic field before the supercurrent was swept up from zero. The two current sweeps displayed in Figure 7.10 were performed in an applied field of 0.5mT so that the response of a single flux vortex could be investigated. As the supercurrent density increases, there is a small continuous shift in the vortex position until, at a threshold current, there is discontinuous jump which marks the onset of flux creep. This is followed over a narrow current range by a series of downward jumps probably caused by the same entry of additional flux associated with the applied supercurrent that was observed in the temperature sweeps. The onset of flux creep is also signalled by an increase in Hall voltage noise.

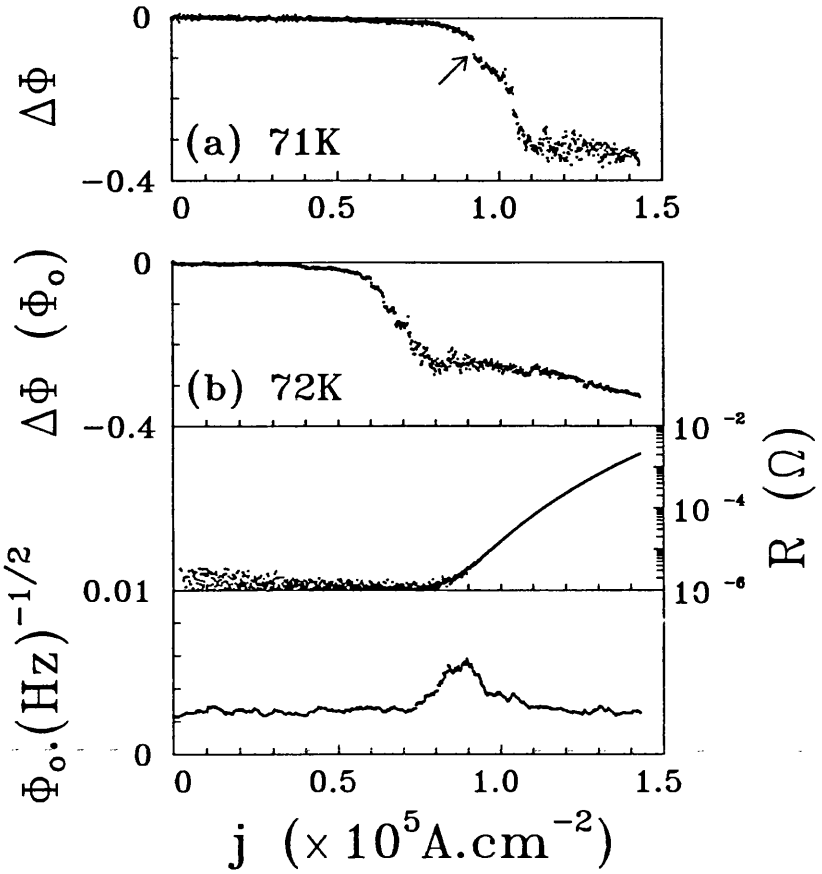

Figure 7.10. (a) The change in flux ($\Delta\Phi$) threading a Hall probe as a function of supercurrent density in the YBCO film in a 0.5mT applied field. The arrow indicates the onset of flux creep. (b) The change in flux ($\Delta\Phi$) threading the Hall probe in a 0.5mT applied field is plotted (top) together with the flux flow resistance (middle) and the excess Hall voltage noise (bottom).

The resistance R of the YBCO strip was measured at the same time as $\Delta\Phi$ and is included in Figure 7.10(b). (Note that the changing noise in the resistance is an experimental artefact caused by the division of the constant background voltage noise by the increasing supercurrent.) Comparing R and $\Delta\Phi$, it can be seen that flux entry and creep are detected by the Hall probe before there is a measurable flux flow resistance. As current density increases further, the flux creep becomes more rapid and cannot be resolved due to the 100ms time constant of the Hall voltage measurement. At about the same time a measurable flux flow resistance appears, and the Hall voltage starts to drift off as a result of the gating effect. The transition from flux creep to flux flow was also seen in the previous section. In the temperature sweeps, the pinning

force was changing while the Lorentz force exerted by the supercurrent was held constant. Now it is the pinning force that remains the same while the Lorentz force increases.

As noted above, the flux creep in the superconductor is a source of excess noise in the output of the Hall probe. There is a noise measurement option on the lock-in amplifier which allows the measurement of the rms noise voltage in a selected bandwidth about the reference frequency. The excess noise in the Hall voltage was measured at a frequency of 10Hz and is plotted in the lowest box of Figure 7.10(b). As expected, the peak in the 10Hz noise power coincides with the fluctuations in the Hall voltage measured with a 100ms time constant. It was not possible to measure the noise over a wide range of frequencies because the peak disappeared into the background noise at frequencies above 30Hz.

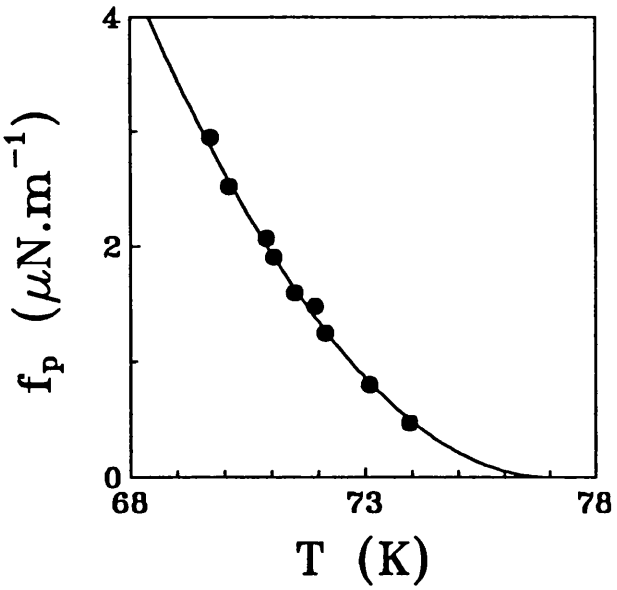

Figure 7.11. Pinning force in the YBCO film as a function of temperature. The solid line is a fit to $(1-t)^2$.

Pinning forces were obtained from both the temperature and current sweeps. Assuming a uniform distribution of supercurrent in the film, the Lorentz force per unit length exerted on a vortex is $\mathbf{f}_L = \mathbf{j} \times \Phi_0$ and is equal to the pinning force f_p at the onset

of flux creep. The pinning force is plotted as a function of temperature in Figure 7.11 and it is apparent that f_p tends to zero well before T_c. The solid curve is a fit to the data under the assumption that close to the transition $f_p \propto (1-t)^2$, the same as a temperature dependence[3] that has been observed for j_c. The best fit was found when the reduced temperature t was calculated using $T_p = 77.0 \pm 0.2\text{K}$ instead of $T_c = 82\text{K}$.

Referring back to the 75K hysteresis loop in Figure 7.3, it was found that the critical current determined by the critical state model is very close to zero and it is not surprising that the pinning force approaches zero at a similar temperature. The vortices depin well before the resistive transition appears to begin at $78.0 \pm 0.1\text{K}$. The most likely explanation is that the direct resistance measurement is not sensitive enough to detect the tiny voltages produced by flux creep. In the temperature sweeps in the previous section, the onset of flux creep is always seen 1-2K before it is possible to measure a flux flow voltage.

The pinning force was measured in a very low 0.5mT magnetic field which does not access the area of the *H-T* phase diagram believed to contain the vortex liquid phase. Indeed, the temperature and current sweeps showed no sign of vortex motion in the absence of the driving force provided by a supercurrent. At low magnetic fields close to the superconducting transition, it appears as if the appropriate way to describe the mixed state of the YBCO film is by vortices depinned by thermal activation before the material becomes fully normal.

Chapter 8

Conclusions

8.1. Introduction

The work presented in this thesis demonstrates that micron-sized 2DEG Hall probes can provide unique and valuable information about the behaviour of flux vortices in type II superconducting films. While Hall probes have often been used to examine the inhomogeneous magnetic fields associated with superconductors, most previous work has employed relatively large probes which cannot resolve fine magnetic structures such as flux vortices. By shrinking the Hall probes to micron dimensions, a much wider range of information was obtained with higher spatial and temporal resolution than much of the previous work.

The high-mobility 2DEG found in a GaAs/$Al_xGa_{1-x}As$ heterostructure was used to make sensitive Hall probes that could operate over a wide temperature range. To make high resolution measurements, it is vital that there is a small separation between the probe and the superconducting surface. A reliable technique was developed to achieve this as well as a method for estimating the separation of the superconducting film and 2DEG, based on the assumption that the superconductor exists in the Meissner state for very small applied magnetic fields. Hall probes with characteristic dimensions from 2 to 10μm were fabricated and applied to Pb and Pb(1% In) films. The most interesting results were obtained with 2μm Hall bars and these were also applied to Nb and YBCO supérconducting films. The results are discussed in more detail in the following sections.

8.2. Pb Films

The first results were obtained from 200nm Pb and Pb(1% In) films that were directly deposited onto 10μm Hall bars. Magnetic field sweeps below T_c provided hysteresis loops which showed delayed flux entry and exit from the centre of the films caused by flux pinning. Flux pinning was found to be stronger in the Pb films. The Hall bars could detect flux jumps due to the motion of small bundles of flux containing typically 4-10 vortices. The 2DEG was suitable for both Hall voltage and magnetoresistance measurements and the complementary information provided was used to calculate the densities of up and down vortices threading the Hall probe at low applied fields. This revealed the coexistence of vortices and antivortices in the Pb film and subsequent vortex-antivortex annihilation.

With reduction of the Hall bar dimensions to 2μm, the character of the measurements changed dramatically because there was now much less spatial averaging of the magnetic field. When the magnetic field was swept around a hysteresis loop, discontinuous steps were observed in the Hall voltage due to the entry or exit of flux bundles. By measuring the Hall voltage simultaneously at pairs of Hall probes at different separations, the flux bundle correlation radius in the Pb film was found to be 2.6μm, in reasonable agreement with a theoretical estimate.

It was also possible to track single vortices and correlated bundles as they moved in response to a change in temperature or under the action of an applied dc supercurrent. With increasing temperature, flux vortices were found to move small distances of 20-40nm driven by vortex interactions as pinning forces weakened near T_c. When a dc supercurrent was flowing through the film, the Lorentz force acting on the vortices could produce flux creep and flux flow. Flux creep appeared when the supercurrent exceeded a definite threshold value and was characterized by a series of discontinuous changes in the flux threading the Hall probe. Flux flow coincided with the appearance of a measurable resistance in the Pb film and was detected as a smooth

change in Hall voltage because flux motion was too rapid to be resolved. Pinning forces were measured as a function of temperature at individual pinning sites from the characteristic onset of flux creep. The pinning forces were all fitted to the same empirical form but each pinning site displayed a different detailed temperature dependence.

8.3. Nb Films

A Nb film 200nm thick was deposited onto a separate substrate and attached to a 2μm Hall bar with a thin layer of adhesive. The 0.5μm separation was small enough to allow high resolution measurements. In common with the Pb films, the magnetic hysteresis loops showed the entry and exit of vortices in flux bundles and coincidence measurements revealed that the flux bundle radius decreased from 3.4μm to 1.6μm as the temperature increased from 4.5K to 6.5K, unlike the temperature independence observed for the Pb film. Both temperature dependences were explained qualitatively by the theory of Larkin and Ovchinnikov[24], taking into account the measured temperature dependence of the pinning forces in the appropriate film.

The temperature sweeps showed similar effects to those observed in the Pb films. The results obtained with a dc supercurrent flowing through the Nb film were disappointing because high contact resistances prevented the application of large enough currents. Nevertheless it was possible to observe the onset of flux creep and to determine the pinning force in the Nb film at individual sites, all of which displayed the same temperature dependence.

8.4. $YBa_2Cu_3O_{7-\delta}$ Films

The 0.35μm-thick YBCO film was attached to a 2μm Hall bar in the same way as the Nb film, with the adhesive layer estimated to be 1μm thick. In contrast to the Pb and Nb films, the YBCO hysteresis loops did not show large multi-quantum

discontinuities resulting from the entry or exit of flux bundles. Greater sensitivity was obtained by a differential measurement where the Hall voltage at one probe was subtracted from that at a neighbouring probe. Fine structure was observed, suggesting that single vortices entered in an uncorrelated fashion, consistent with a high density of pinning centres in the film. The smooth YBCO hysteresis loops could be fitted to the critical state model of Brandt *et al*[28], providing the critical current in the film over a wide temperature range. 'Shoulders' in the loops that could not be fitted to the critical state model were seen as evidence for a geometrical barrier against flux entry.

Features were only seen on the temperature sweeps with a dc transport current flowing through the film, when it was possible to observe the crossover from flux creep to flux flow. Similar behaviour was observed when the transport current was ramped up from zero at fixed temperature. The pinning force determined from the onset of flux creep at an individual pinning site extrapolated to zero at a depinning temperature well below the critical temperature of the film and before there was a detectable resistance in the film. It appears that the flux vortices are depinned by thermal activation before the material becomes fully normal, in contrast with the Pb and Nb films where the pinning force vanished at T_c.

8.5. Future Prospects

The present work has proven the value of Hall probes as local probes of vortex properties and suggests a number of avenues for further investigations. An obvious limitation of the technique is that the Hall probe is fixed with respect to the superconductor. This can be overcome by a scanning probe system but at the expense of a considerable increase in complexity of the experimental apparatus. Linear arrays of Hall probes will continue to be a simple option for examining different areas of a superconducting sample. A new Hall bar design that would allow a string of Hall probes to extend from the centre to the edge of a sample would give a detailed picture

of the flux distribution without the need for a complex scanning mechanism.

Future work will concentrate on high-T_c films and single crystals, with the aim of learning more about the wide variety of new phenomena observed in these materials. Unfortunately the irreversibility line and the controversial flux liquid phase are found in the high field region of the *H-T* phase diagram where there is little magnetic field modulation and it will be very difficult if not impossible to detect individual vortices. It is possible that the differential measurement technique will be useful in lower magnetic fields closer to T_c. For example, flux lines in highly anisotropic $Bi_2Sr_2CaCu_2O_8$ crystals appear to cross-over from 3D to 2D behaviour in moderate $(<100\text{mT})$ magnetic fields[59]. Hall probe measurements combined with a supercurrent flowing through the crystal should yield interesting results.

Appendix A

Sample Fabrication

A.1. Introduction

This appendix lists detailed procedures for the fabrication of Hall bars from a $GaAs/Al_xGa_{1-x}As$ heterostructure.

A.2. Fabrication Procedure

1. The GaAs wafer containing the heterostructure was scribed and cleaved into chips $5 \times 5 mm^2$ square.

2. **Cleaning**

   The chips were placed in beakers of (i) trichloroethane, (ii) acetone and (iii) propanol and agitated in each solvent for 5 minutes in an ultrasonic bath. They were rinsed in hot propanol and blown dry with a nitrogen jet.

3. Each chip was glued with photoresist to a clean glass slide to facilitate handling. The photoresist was hardened by baking for 30 minutes at 95°C.

4. **Photolithography**

   Shipley Microposit S1813 photoresist was spun onto the chips at a speed of 4000rpm for 25-30 seconds, producing a ~1.3μm-thick layer of photoresist which was baked for 30 minutes at 95°C. Contact pads were defined by exposing the photoresist to ultraviolet light through the contact mask for 8 seconds. The photoresist was developed in Shipley

Microposit 351 developer for 50-60 seconds, rinsed in distilled water and hard-baked for 30 minutes at 95°C.

The lift-off process described in the next step could be improved if the photoresist was soaked in chlorobenzene for 10-12 minutes after exposure, and then dried in air for 2 hours before development.

5. Ohmic contacts

Each chip was dipped in a 1:1 solution of conc. HCl and distilled water for one minute to remove the surface oxide, rinsed in distilled water and blown dry. The chip was immediately placed in the evaporator, heated up to 80-90°C under vacuum, and 660Å of Ge, 1340Å of Au and 200Å of nickel deposited. Before the metals were evaporated, the chip surface was cleaned by an Ar glow discharge for 10 minutes. On removal from the evaporator, the chip was soaked in acetone to dissolve all of the photoresist, removing the chip from the slide and lifting off the unwanted Ge-Au-Ni film while leaving behind the contact pads.

After being rinsed in propanol, the chip was placed in a flash annealer and the contacts annealed in a reducing N_2/H_2 atmosphere at 430°C for 2 minutes. The gold and germanium layers form a 88%:12% Au-Ge eutectic and diffuse into the GaAs, creating an n^+ region that makes ohmic contact to the 2DEG. The Ni layer acts as a diffusion activator.

6. Gold contact layer

200Å of Ti (for good adhesion) and 2000Å of Au were deposited on top of the ohmic contacts to provide a layer suitable for ultrasonic wire bonding. The metal films were patterned using the same lift-off technique used for the ohmic contacts.

7. Etching

Photoresist was spun on at 4000rpm for 5 seconds and then at 6000rpm for 12 seconds in order to minimise the edge bead caused by

build up of photoresist at the corners and edges of the chip. After baking (30 minutes at 95°C), the photoresist was exposed for 5 seconds using the etch mask to define the Hall bar structures. The photoresist was immediately developed for 30-40s, and hard-baked (30 minutes at 95°C). The surface oxide was removed as described in step 5. To etch away the unwanted regions of 2DEG, the chip was dipped in a 160:8:1 solution of distilled water, H_2O_2 (30%) and conc. H_2SO_4 , a general GaAs/$Al_xGa_{1-x}As$ etchant with an etch rate of approximately $0.2\mu m.min^{-1}$. Depending on the depth of the 2DEG, etch times were usually 15-20 seconds. It is not necessary to etch right down to the 2DEG; halfway is sufficient to ensure that the 2DEG is depleted beneath the etched areas. The photoresist was removed with acetone, and the chip rinsed in acetone and propanol.

8. Pb films

Photoresist was spun on at the slow speed of 2500rpm for 30 seconds, providing a layer of photoresist ~1.5μm thick. Pb is a soft metal with poor adhesion, and the thicker photoresist makes the lift-off process easier. Pb was deposited by thermal evaporation with the chip held at ambient temperature.

Appendix B

List of Publications

The work described in this thesis has led to the following publications :

Correlated flux vortices in Nb films, S.T. Stoddart, S.J. Bending, R.E. Somekh, and M. Henini, submitted to Supercond. Sci. Technol.

Fluxon-resolved studies of high-T_c superconducting films, S.T. Stoddart, S.J. Bending, M. Henini and R.G. Humphreys, to be published in Physica B

The pinning potential at single flux vortices investigated using sub-micron Hall probes, S.T. Stoddart, A.K. Geim, S.J. Bending, and M. Henini, Physica B **194-196**, 1899 (1994)

Quantum-resolved investigations of flux dynamics : collective and single vortex effects, S.T. Stoddart, S.J. Bending, A.K. Geim, and M. Henini, Phys. Rev. Lett. **71**, 3854 (1993)

Microscopic investigation of the flux dynamics of type-II superconducting films, S.T. Stoddart, H.I. Mutlu, A.K. Geim, and S.J. Bending, Phys. Rev. B **47**, 5146 (1993)

References

1. D.A. Huse, M.P.A. Fisher, and D.S. Fisher, Nature **358**, 553 (1992)
2. D.J. Bishop, P.L. Gammel, D.A. Huse, and C.A. Murray, Science **255**, 165 (1992)
3. K. Kadowaki, Y. Songliu, and K. Kitazawa, Supercond. Sci. Technol. **7**, 519 (1994)
4. H. Träuble and U. Essmann, J. Appl. Phys. **39**, 4052 (1968)
5. O.B. Hyun, D.K. Finnemore, L. Schwartzkopf, and J.R. Clem, Phys. Rev. Lett. **58**, 599 (1987)
6. S.C. Sanders, J. Sok, D.K. Finnemore, and Q. Li, Phys. Rev. B **47**, 8996, (1993)
7. G.S. Park, C.E. Cunningham, B. Cabrera, and M.E. Huber, Phys. Rev. Lett. **68**, 1920 (1992)
8. R.C. Black *et al.*, Appl. Phys. Lett. **62**, 2128 (1993)
9. L.N. Vu, M.S. Wistrom, and D.J. Van Harlingen, Appl. Phys. Lett. **63**, 1693 (1993)
10. H.F. Hess *et al.*, Phys. Rev. Lett. **62**, 214 (1989)
11. T. Matsuda *et al.*, Phys. Rev. Lett. **62**, 2519 (1989)
12. T. Tamegai *et al.*, Phys. Rev. B **45**, 8201 (1992)
13. D.A. Brawner *et al.*, Phys. Rev. Lett. **71**, 785 (1993)
14. E. Zeldov, D. Majer, M. Konczykowski, A.I. Larkin, V.M. Vinokur, V.B. Geshkenbein, N. Chikumoto, and H. Shtrikman, to be published in Phys. Rev. Lett. (1994)
15. M.L. Roukes *et al.*, Phys. Rev. Lett. **59**, 3011 (1987)
16. U. Hartmann, Appl. Phys. A **59**, 41 (1994)
17. H.J. Hug, A. Moser, I. Parashikov, B. Stiefel, O. Fritz, H.-J. Güntherodt, and

H. Thomas, to be published in Physica C (1994)

18. A.M. Chang *et al.*, Appl. Phys. Lett. **61**, 1974 (1992)

19. R.P. Huebener, *Magnetic Flux Structures in Superconductors* (Springer-Verlag, Berlin 1979)

20. J.R. Clem, J. Low Temp. Phys. **18**, 427 (1975)

21. J.R. Clem, *Proc. 14th Intern. Conf. Low Temp. Phys.*, eds. M. Krusius and M. Vuorio (North-Holland, Amsterdam 1975) Vol. 2, p.285

22. P.W. Anderson and Y.B. Kim, Rev. Mod. Phys. **36**, 39 (1964)

23. M. Tinkham, *Introduction to Superconductivity* (McGraw Hill, New York, 1975)

24. A.I. Larkin and Yu. N. Ovchinnikov, J. Low Temp. Phys. **34**, 409 (1979)

25. A.I. Larkin, Sov. Phys. JETP **31**, 784 (1970)

26. M. Tinkham, Phys. Rev. **129**, 2413 (1963)

27. G.J. Dolan, J. Low Temp. Phys. **15**, 111 (1974)

28. E.H. Brandt, M.V. Indenbom, and A. Forkl, Europhys. Lett. **22**, 735 (1993)

29. E.H. Brandt and M.V. Indenbom, Phys. Rev. B **48**, 12893, (1993)

30. E. Zeldov, J.R. Clem, M. McElfresh and M. Darwin, Phys. Rev. B **49**, 9802 (1994)

31. M. Jaros, *Physics and Applications of Semiconductor Microstructures* (Clarendon Press, Oxford, 1989)

32. E.H. Putley, *The Hall Effect and Related Phenomena* (Butterworths, London, 1960)

33. R.S. Popovic', *Hall Effect Devices : Magnetic Sensors and Characterization of Semiconductors* (Adam Hilger, IOP Publishing Ltd, Bristol, 1991)

34. B.L. Altshuler, D. Khmel'nitzkii, A.I. Larkin, and P.A. Lee, Phys. Rev. B **22**, 5142 (1980)

35. A.K. Geim, S.J. Bending, and I.V. Grigorieva, Phys. Rev. Lett. **69**, 2252 (1992)

36. A.K. Geim, S.V. Dubonos, and A.V. Khaetskii, JETP Lett. **51**, 121 (1990)

37. J. Rammer and A.L. Shelankov, Phys. Rev. B **36**, 3135 (1987)

38. A.K. Geim, JETP Lett. **50**, 389 (1989)

39. S.J. Bending, K. von Klitzing, and K. Ploog, Phys. Rev. Lett. **65**, 1060 (1990)

40. S.J. Bending and A.K. Geim, Phys. Rev. B **46**, 14912 (1992)

41. D.D. Roshon, Rev. Sci. Instrum. **33**, 201 (1962)

42. *Landolt-Börnstein : Numerical Data and Functional Relationships in Science and Technology New Series, Volume III/17a Physics of Group IV Elements and III-V Compounds*, O. Madelung (Editor), (Springer-Verlag, Berlin 1982)

43. E.W. Saker, F.A. Cunnell, and J.T. Edmond, Brit. J. Appl. Phys. **6**, 217 (1955)

44. R. Carey and E.D. Isaac, *Magnetic Domains and Techniques for their Observation* (English Universities Press, London, 1966)

45. T-H. Shen *et al.*, Supercond. Sci. Technol. **4**, 232 (1991)

46. J.R. Barker, Brit. J. Appl. Phys. **1**, 65 (1950)

47. A.K. Geim, V.I. Falko, S.V. Dubonos, and I.V. Grigorieva, Solid State Commun. **82**, 831 (1992)

48. S.J. Bending, K. von Klitzing, and K. Ploog, Phys. Rev. B **42**, 9859 (1990)

49. M.J. Uren, R.A. Davies, M. Kaveh, and M. Pepper, J. Phys. C **14**, L395 (1981)

50. R.P. Huebener and D.E. Gallus, Phys. Rev. B **7**, 4089, (1973)

51. K. Harada *et al.*, Nature **360**, 51 (1992)

52. Q. Li, J.R. Clem, and D.K. Finnemore, Phys. Rev. B **43**, 12843 (1991)

53. M.A. Reed, W.P. Kirk, and P.S. Kobiela, IEEE J. Quantum Electron. **22**, 1753 (1986)

54. L.H. Allen and J.H. Claassen, Phys. Rev. B **39**, 2054 (1989)

55. R.G. Humphreys and J.A. Edwards, Physica C **210**, 42 (1993)

56. E. Zeldov *et al.*, Phys. Rev. Lett. **73**, 1428 (1994)

57. T.L. Hylton and M.R. Beasley, Phys. Rev. B **41**, 11669 (1990)

58. P. England, *et al.*, Phys. Rev. B **41**, 4834 (1990)

59. S.L. Lee *et al.*, Phys. Rev. Lett. **71**, 3862 (1993)